Disorder in Entropic Solids

Disorder in Entropic Solids

Academisch Proefschrift

ter verkrijging van de graad van doctor aan de Universiteit van Amsterdam op gezag van de Rector Magnificus prof. mr. P. F. van der Heijden ten overstaan van een door het college voor promoties ingestelde commissie, in het openbaar te verdedigen in de Aula der Universiteit op woensdag 10 december, te 11:00 uur.

door

Sander Pronk

geboren te Alkmaar

Promotor: prof. dr. D. Frenkel

Faculteit: Natuurwetenschappen, Wiskunde en Informatica

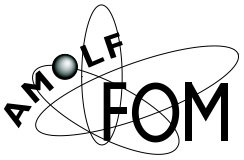

The work described in this thesis was performed at the FOM Institute for Atomic and Molecular Physics, Kruislaan 407, 1098 SJ, Amsterdam, The Netherlands. The work is part of the research program of the Stichting voor Fundamenteel Onderzoek der Materie (FOM) and was made possible by financial support from the Nederlandse Organisatie voor Wetenschappelijk Onderzoek (NWO).

Cover: Triangulation of a polydisperse hard disk system at $\nu = 0.006$,
$P = 19.25 k_B T/\sigma^2$

The work in this thesis covers the following publications:

Chapter 3:
PRONK, S. AND FRENKEL, D. Can stacking faults in hard-sphere crystals anneal out spontaneously? *J. Chem. Phys. 110*, 9 (1999), 4589.

Chapter 4:
PRONK, S. AND FRENKEL, D. Large difference in the elastic properties of fcc and hcp hard-sphere crystals *Phys. Rev. Lett. 90*, 25 (2003), 255501.

Chapter 5:
PRONK, S. AND FRENKEL, D. Point defects in hard-sphere crystals *J. Phys. Chem. B 105*, 28 (2001), 6722.

Chapter 6:
PRONK, S. AND FRENKEL, D. Large effect of polydispersity on defect concentrations in colloidal crystals (submitted to J. Chem. Phys.)

Chapter 7:
PRONK, S. AND FRENKEL, D. Melting of polydisperse hard disks (submitted to Phys. Rev. E.)

Contents

1 Introduction **1**
- 1.1 Entropic solids . . . 1
- 1.2 Disorder . . . 4

2 Technical Background **7**
- 2.1 Computer Simulation: Free Energy Methods in Solids . . . 7
- 2.2 Elasticity . . . 11
- Appendix A: Force and the Stress Tensor . . . 17

3 Stacking Faults in Hard Sphere Crystals **21**
- 3.1 Lattice Switch Monte Carlo . . . 22
- 3.2 Results . . . 23
- 3.3 Discussion . . . 24

4 Stacking and Elasticity **27**
- 4.1 Lattice Symmetries and Elasticity . . . 27
- 4.2 Simulations . . . 28
- 4.3 Polydispersity . . . 33
- 4.4 Lattice Anisotropy . . . 35
- 4.5 Conclusion . . . 36

5 Point Defects in Hard Sphere Crystals **37**
- 5.1 Free Energy of Vacancies . . . 38
- 5.2 Computational Scheme . . . 44
- 5.3 Simulation Results . . . 46
- 5.4 Analytical Estimate of the Free Energy of Interstitials . . . 47

6 Polydispersity and Point Defect Concentrations **53**
- 6.1 Simulation Methods . . . 53
- 6.2 Results . . . 57
- 6.3 Discussion . . . 58

7 Melting of Polydisperse Hard Disks **63**
- 7.1 The System . . . 64
- 7.2 Simulations . . . 68
- 7.3 Conclusion . . . 72

8 Monte Carlo Study of Hard Pentagons **75**
8.1 Background 75
8.2 Simulations 76
8.3 The Elastic Antiferromagnet on a Triangular Lattice 82
8.4 Conclusion 84

Bibliography **85**

Summary **93**

Samenvatting **95**
Het mysterie van de entropie 95
Is natuurkunde exact? 96
Harde bollen 98

Nawoord **103**

1 Introduction

1.1 Entropic solids

At the heart of the highest-temperature, highest-density ordered crystalline phase of most materials lies a short-ranged, steeply repulsive inter-particle interaction (for an early postulation of this fact, see Bridgman[1]). Although for most simple molecular and atomic solids (metals, salts), the details of the attractive part of the inter-particle potential determine the type of crystalline ordering, beyond a certain density and at sufficiently high temperatures, there must be a crystalline phase for any system with such a steeply repulsive interaction.

The crystalline phase is characterized by a spontaneous ordering of the particles into regular arrangements. These arrangements can be thought of as consisting of repeating unit cells containing one or more particles, i.e. with broken translational and rotational symmetry. Surprisingly, the entropy of this phase can be higher than the entropy of a fluid phase of equal density, as was found in some of the very first applications of computer simulations in 1957 by Alder and Wainwright[2] (with molecular dynamics simulations) and Wood and Jacobson[3] (who did Monte Carlo simulations) on a system of hard spheres. These authors found that there is a first-order phase transition from a fluid phase to a crystalline phase.

The phase behaviour of elastic hard spheres (i.e. particles with zero interaction energy if they are separated by a distance more than the sum of their radii, and infinite interaction energy if the distance separating them is smaller) is determined solely by entropy: when the momentum part of the partition sum is separated out, we are left with the configurational part which, for hard spheres, does not depend on temperature (as the Boltzmann weight for any given configuration is either zero — when particles overlap — or one). This means that only the number of configurations, i.e. the entropy, determines the free energy of the system. Solids of hard spheres and of hard particles in general are therefore referred to as entropic solids.

The crystalline solid is not the only ordered phase that hard particles can form;[4] for example, hard spherocylinders form nematic and smectic liquid crystals (partially ordered phases with order in one and two dimensions, respectively).[5] Possibly, two-dimensional hard disks have a hexatic phase in which there is no translational order but six-fold orientational order.[6] In general, for the class of lyotropic liquid crystals, it can be said that the short-range steric repulsion is what usually determines the phase behaviour at high densities.

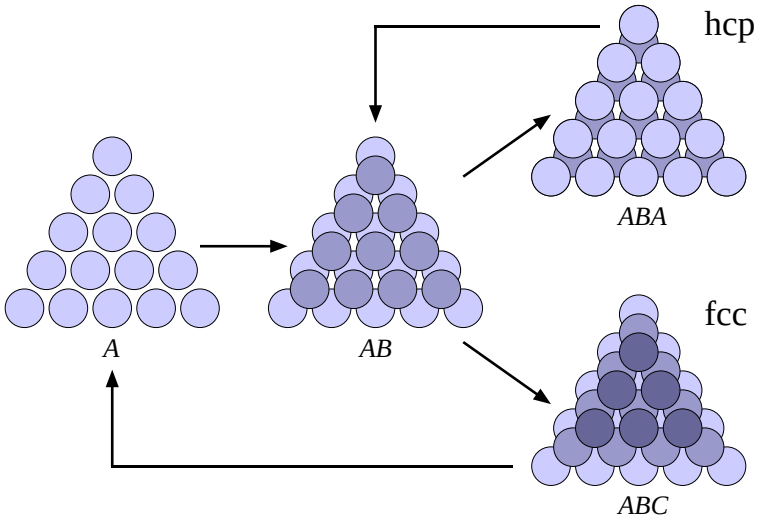

Figure 1.1: Layer stacking of spheres.

1.1.1 The Hard Sphere Solid

Because temperature is not a relevant thermodynamic variable for hard-particle systems, the phase diagram of a system of hard spheres can be thought of as a line; the phase coexistence between fluid and solid runs from a packing fraction $\eta = 0.49171$, the freezing point of the fluid, to $\eta = 0.54329$, the melting point of the solid.[7]

The thermodynamically stable hard sphere crystal forms the structure that was conjectured by Keppler to be the closest packing of spheres, as has only recently been confirmed.[8] In this structure, the spheres form hexagonal layers (see Fig. 1.1) which are stacked in such a way that the particles in each layer fit into the 'holes' of the preceding and succeeding layer.

As Fig. 1.1 shows, there are two distinct places where a succeeding layer would fit into the 'holes' of a layer of closely packed spheres. If we were to label the first layer to be at location *A*, and the next layer *B* (here, choosing a different 'hole' would make no difference), the *third* layer can either be back at *A*, or at *C*. The two simplest repeating structures are thus *ABAB*... and *ABCABC*..., where the former constitutes the hexagonal close packing (hcp) structure, and the latter is in fact a face-centered cubic (fcc) structure.

The higher symmetry of fcc can be seen in Fig. 1.2. There, the cubic unit cell of the fcc crystal is shown, with the hexagonally close packed layers of the *ABCABC* packing delineated by the lines that diagonally cross the faces of the cubic unit cell.

The relative thermodynamic stability of fcc vs. hcp, the free energy difference, is extremely small: in the order of $10^{-3} k_B T$ per particle (see refs. 9, 10, 11 or chapters 3 and 4). In practice, this will often cause the crystal to have random

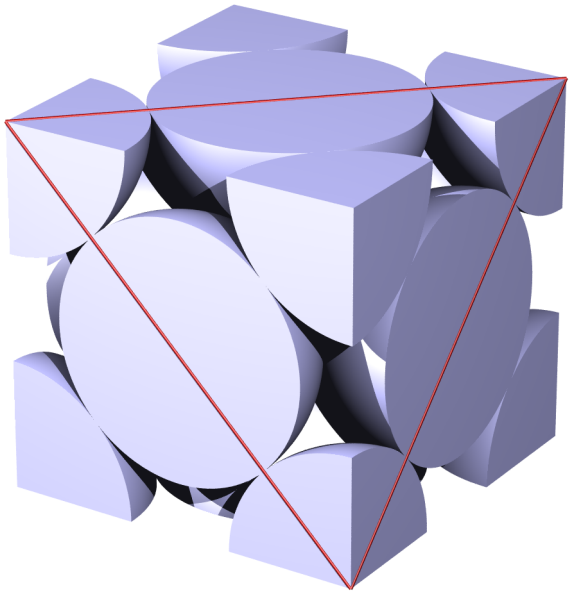

Figure 1.2: The fcc unit cell. The cross-section of one close-packed layer is delineated.

stacking: the entropy contribution of the choice in stacking will outweigh the bulk free energy gains for smaller crystals.

1.1.2 Colloidal Hard Spheres

Hard spheres, and hard particles in general, are not just model systems. While it is not possible to have hard interactions on the atomic scale, it is possible to prepare colloidal suspensions that consist of effectively hard particles.

Colloidal suspensions are suspensions of particles in a size range from several nanometers to about 1 micron; small enough to be subjected to thermal motion in the form Brownian motion and with a thermal energy at least as high as the gravitational energy of a few particle diameters, but big enough so that detailed knowledge about the internal degrees of freedom of each individual colloidal particle is not important for the behaviour of the suspension.[12]

Colloids interact through a potential of mean force that makes it possible to treat them as 'giant molecules'; depending on density and temperature, a suspension can show gas, liquid and crystalline phases, just like atomic and molecular systems. The colloidal interaction can often be modeled by a screened Coulomb interaction together with dispersion forces, known as the DLVO — Derjaguin, Landau, Verweij and Overbeek — potential.[12,13] A distinguishing feature of the inter-particle potential is an effective hard-core repulsion at short range and a soft attractive or

repulsive interaction at intermediate ranges (and possibly a strongly attractive part at very short ranges, causing colloidal aggregation under certain conditions).

The tunability of the inter-particle interaction (by, for example, manipulating the salt concentration of the solvent to change the range for the screened Coulomb interaction) of colloids makes them eminently suitable for studying the effect of inter-particle forces on the phase behaviour. The fact that the particles themselves are relatively large and usually well distinguishable from the surrounding solvent, makes it feasible to perform real-space analysis of the equilibrium and dynamic behaviour of these systems using microscopic measurement techniques.[14]

Colloidal suspensions are found in many common substances, ranging from paints to biological systems. In nature, the particles are mainly found in fluid phases, but there are some examples of crystalline colloidal systems in nature; opals being the most well-known. Recently, the optical properties of colloids of roughly the size of the wavelength of visible light, have started to become exploited as a self-assembling photonic material; the crystalline phases are in principle well suited to make large, visible light photonic band-gap materials.[15]

By, for example, grafting polymers to the surface of colloids, the effective potential can be made to become harshly repulsive.[16] Such 'hard-sphere' colloidal suspensions have an equation of state that corresponds to the one found in computer simulations.[17,18,19,20] Hard-sphere colloids exhibit a first-order phase transition from the fluid to a close-packed crystal structure.[21] The exact type of close-packed structure formed depends on experimental conditions but can partly be understood from simulations (see, for example chapter 3 or Ref. 11).

An intrinsic property of many colloidal suspensions is that not all particles have the same size (and possibly shape); they are polydisperse. Polydispersity influences the equilibrium behaviour; possibly destabilising ordered phases, widening coexistence areas and causing size fractionation.[22,19,23,24] Typically, for experiments on hard-sphere colloidal suspensions, the polydispersity of the originally liquid colloidal suspension varies from 3% to 5%.

1.2 Disorder

This thesis focuses on the role of disorder on the equilibrium behaviour in entropically ordered phases, in particular the hard sphere crystal. Although potentially important for applications of ordered colloidal systems like the already mentioned photonic materials, there have, up to now, not been many studies on this subject, which is not surprising given the experimental difficulties in obtaining measurements of most of the types of disorder mentioned. The types of disorder considered here are stacking faults, polydispersity, point defects, the possiblity of dislocation unbinding in 2D and orientational disorder.

Chapter 3 and 4 describe the effects of stacking (fcc or hcp) on the hard sphere crystal. Stacking faults, faults in stackings of close-packed layers which transform part of the crystal from fcc to hcp or vice versa arise, as mentioned above, because of the entropy gain in the choice of two layer types, and the low bulk free energy

differences involved. This type of stacking faults is not unique to hard spheres; for example, there is a possiblity of this happening in Lennard-Jones potentials, where for some densities the zero-temperature free energy differences between fcc and hcp changes sign as a function of density and is in general in the order of $10^{-3}k_BT$ per particle.[25]

Some experimental studies have been performed to establish the exact type of stacking that spontaneously occurs under gravity[26,27,28,29] and in micro-gravity conditions.[30,31] In addition, it is possible to manipulate the boundaries of the deposited colloidal crystals to form pure fcc[32] and even the metastable hcp.[33]

The study of the influence of polydispersity on solids has centered on the range of stability of polydisperse crystals (the phase behaviour)[23,34] and fractionation effects.[35,24] In experiments, the effect on the equation of state has been studied by Phan et al.[22] Chapters 4, 6 and 7 explore various aspects of the polydisperse crystal.

Of the mentioned types of disorder, perhaps the most well understood is that of point defects. Point defects play a key role in the dynamic behaviour of solids, with their mobility being one of the principal agents of diffusion in crystalline solids[36] (for an example, see Ref. 37). Applications of point defects include traditional silver-based photography, where vacancy-interstitial pairs are created by electromagnetic radiation in the form of visible light in silver-halide crystals. The interstitials then aggregate to stable clusters which after develompent, cause the image to form.[38] In hard sphere crystals, not much is known about point defect concentrations experimentally; computer simulations by Bennett and Alder[39] give a relatively high (in the order of 10^{-4}) concentration for vacancies. Chapters 5 and 6 deal with the formation of point defects in hard sphere solids in equilibrium.

In two dimensions, the solid crystalline phase is at its lower critical dimension. Strictly speaking, there is no long-range translational order.[40,41,6] There is a universal melting mechanism, the Kosterlitz-Thouless-Halperin-Nelson-Young (KTHNY) melting scenario, which occurs when the free energy of free dislocations becomes smaller than zero. This happens when the crystal is so ‘soft’ (elastic constants are low enough) that the translational entropy of the dislocations becomes higher than the cost in elastic energy. At this point, the crystalline phase should go through two continuous phase transitions, with a liquid crystalline phase in between: the hexatic phase. This melting scenario, although universal, need not neccesarily occur because it can be pre-empted by a first-order phase transition. For two-dimensional hard disks, it is, as of yet, unknown which of the two mechanisms takes place: KTHNY melting or a weak first-order phase transition. In chapter 7, the introduction of polydispersity, which widens the coexistence gap in three dimensions, is explored for two-dimensional hard disks.

Finally, in chapter 8, the equilibrium phase behaviour of a type of particle is investigated which has a symmetry that is incommensurate with the symmetry of the lattices it forms: the pentagon. The two-dimensional pentagon system forms a hexagonal lattice at lower densities, but upon increasing the density, forms a ‘striped’ phase that closely resembles striped phases in elastic antiferomagnetic spin systems.

2 Technical Background

2.1 Computer Simulation: Free Energy Methods in Solids

Particle-based computer simulations such as Monte Carlo (MC) or Molecular Dynamics (MD) simulations do not allow direct measurements of the accessible volume of the configurational phase space. As the entropy and, as a consequence, the free energy, is determined by this volume, direct calculations of the free energy of all but the smallest systems are impossible. However, it is possible to compute *differences* in free energy. To compute such differences, one makes use of the fact that derivatives of the free energy can be computed directly in a simulation. Imagine, for instance, that the free energy of the system is known at one particular density. Then we compute the free energy at another density by computing the density derivative of the free energy:

$$\left(\frac{\partial F}{\partial \rho}\right)_{N,T} = NP(\rho)/\rho^2 \tag{2.1}$$

where $P(\rho)$ is the pressure of the system at density ρ. By integration, we then find the free-energy difference

$$F(\rho_2) - F(\rho_1) = N\int_{\rho_1}^{\rho_2} d\rho \frac{P(\rho)}{\rho^2} \tag{2.2}$$

This procedure is useful to obtain free energy differences between, for example, a low density fluid (where the ideal gas laws apply) and a dense fluid. However, if there are first-order phase transitions between the two states, then hysteresis makes the compression effectively irreversible and the integration scheme fails.

Fortunately, in computer simulations, there is a wide choice of thermodynamic integration schemes that are not limited to physically realizable transformations. For instance, as Kirkwood first suggested (not in the context of simulations, however) that we can consider the free energy change associated with a change in the interaction potential of the system. If the free energy of the system described by one of these interaction potentials is known (or can be computed analytically) then the free energy of the system described by the second potential energy function can be computed by thermodynamic integration. To this end, we define a generalized potential-energy function that is a linear * combination of the two potentials U_a and

*The combination needs not be linear, but this route has certain computational advantages

U_b

$$U(\lambda) = (1-\lambda)U_a - \lambda U_b \tag{2.3}$$

The free energy of a system with this potential energy function is given by

$$\begin{aligned} F(N,V,T,\lambda) &= -k_B T \ln Q(N,V,T,\lambda) \\ &= \int d\mathbf{r}^N \exp[-\beta U(\lambda)] \end{aligned} \tag{2.4}$$

Clearly,

$$\begin{aligned} \frac{\partial F(\lambda)}{\partial \lambda} &= \frac{1}{Q(N,V,T,\lambda)} \frac{\partial Q(N,V,T,\lambda)}{\partial \lambda} \\ &= \frac{\int d\mathbf{r}^N \partial U(\lambda)/\partial\lambda \exp[-\beta U(\lambda)]}{Q(N,V,T,\lambda)} \\ &= \left\langle \frac{\partial U}{\partial \lambda} \right\rangle \end{aligned} \tag{2.5}$$

which is equal to $< U_b - U_a >$. This quantity can be sampled in a normal simulation (note that the outcome of Eq. 2.5 does not depend on the exact way in which U_a and U_b are coupled in Eq.2.3). This means, that by integrating the thermodynamical average of the derivative of the potential, we can get the free energy difference between the systems with potentials U_a and U_b.

2.1.1 Einstein Integration

One application of this thermodynamic integration is the transformation of a crystal with an arbitrary potential energy function U, to a model crystal with a known free energy: the Einstein crystal. The Einstein crystal is a crystal consisting of particles connected with harmonic springs to their respective lattice sites. It has a configurational energy

$$U_{\mathrm{e}}(\mathbf{r}^N) = \tfrac{1}{2} \sum_i^N \alpha (\mathbf{r}_i - \mathbf{r}_{0,i})^2 \tag{2.6}$$

where $\mathbf{r}_{0,i}$ is the fixed lattice position of the lattice position to which particle i is connected, and α is a spring constant. This gives us a free energy

$$\begin{aligned} F_{\mathrm{e}} &= -k_B T \ln \int d\mathbf{r}^N \exp\left[-\beta \tfrac{1}{2} \sum_i^N \alpha (\mathbf{r}_i - \mathbf{r}_{0,i})^2 \right] \\ &= -k_B T \frac{dN}{2} \ln\left(\frac{\pi}{\alpha\beta} \right) \end{aligned} \tag{2.7}$$

where d is the dimensionality of the system.

Using the functional of Eq. 2.3 (or $U(\lambda) = U_0 + \lambda U_{\mathrm{ei}}$ for hard spheres), there would be a sharp peak of $U(\lambda)$ as $\lambda \to 0$, because the crystal as a whole is allowed to explore the simulation box. This divergence can be removed by constraining

the system to have its center of mass fixed; the correction to the free energy of the Einstein crystal is[42,7]

$$\Delta F_{\mathrm{e,cm}} = F_{\mathrm{e,cm}} - F_{\mathrm{e}} = -k_B T \frac{d}{2} \ln\left(\frac{\beta^2 \alpha}{4\pi^2}\right) \tag{2.8}$$

and to the real crystal it is

$$\Delta F_{\mathrm{cm}} = F_{\mathrm{cm}} - F = -k_B T \ln\left(\frac{\rho}{N}\right) - k_B T \frac{d}{2} \ln\left(\frac{\beta}{2\pi M}\right) \tag{2.9}$$

making the free energy of the crystal

$$\frac{\beta F}{N} = \frac{\beta}{N} \int d\lambda \left\langle \frac{\partial U(\lambda)}{\partial \lambda} \right\rangle + \frac{\beta F_e}{N} + \frac{\beta \Delta F_{\mathrm{e,cm}}}{N} - \frac{\beta \Delta F_{\mathrm{cm}}}{N} \tag{2.10}$$

or (expressed as excess free energy $F_{\mathrm{ex}} = F - F_{\mathrm{id}}$, with F_{id} the ideal gas free energy)

$$\begin{aligned} \frac{\beta F_{\mathrm{ex}}}{N} &= \frac{\beta}{N} \int d\lambda \left\langle \frac{\partial U(\lambda)}{\partial \lambda} \right\rangle + \frac{\beta F_e}{N} + \frac{\ln \rho}{N} \\ &\quad - \frac{d}{2N} \ln\left(\frac{\beta \alpha}{2\pi}\right) + \frac{d+1}{2} \frac{\ln N}{N} \\ &\quad + \ln \rho + 1 - \frac{\ln 2\pi}{2N} \end{aligned} \tag{2.11}$$

The parameter α can be used to keep the value of $\partial U / \partial \lambda$ as flat as possible over the integration range to improve accuracy of the numerical quadrature.[7] Careful integration can yield results with an accuracy of $\mathcal{O}(10^{-6} k_B T)$ per particle (see e.g. chapter 4).

2.1.2 Lattice Switch

Another way to calculate free energy differences between states a and b is by calculating relative probabilities of finding the system in either of these states, which are freely accessible to it. To this end, we define a Landau free energy with order parameter λ

$$\begin{aligned} F(\lambda, N, V, T) &= -k_B T \ln Q(\lambda, N, V, T) \\ &= -k_B T \ln \int d\mathbf{r}^N \delta\left(\lambda' - \lambda(\mathbf{r})\right) \exp\left[-\beta U(\mathbf{r}^{\mathbf{N}})\right] \end{aligned} \tag{2.12}$$

and we say that λ belongs to state $q \in \{a, b\}$ if $\lambda \in \{\lambda_q\}$. Now the free energy associated with state q is the aggregate of the order parameter values belonging to $\{\lambda_q\}$

$$\begin{aligned} F(q|N, V, T) &= -k_B T \ln Q_q(N, V, T) \\ &= -k_B T \ln \sum_{\{\lambda_q\}} d\lambda' Q(\lambda', N, V, T) \end{aligned} \tag{2.13}$$

and the probability of finding the system in state q is

$$P(q) = Q_q(N,V,T)/Q(N,V,T) \tag{2.14}$$

so the free energy difference between a and b becomes

$$\begin{aligned} F(b|N,V,T) - F(a|N,V,T) &= k_B T \ln \frac{Q_a(N,V,T)}{Q_b(N,V,T)} \\ &= k_B T \ln \frac{P(a)}{P(b)} \end{aligned} \tag{2.15}$$

which can in principle be obtained in a single simulation.

The difficulty now is to construct an ensemble that connects the two states of interest with a suitable order parameter. The order parameter has to be such that for a given value there should not be distinct and in practice mutually inaccessible regions of phase space; these will cause sampling problems due to the finite nature of simulations. An example is the ensemble used to calculate the free energy associated with an interstitial in chapters 5 and 6, where the particle diameter of one particle was allowed to vary between 0 and 1 and the probability of finding a particle of diameter 1 was compared with the probability of finding a point particle. This path between normal crystal to a crystal with an interstitial works because the interstitial diffuses quickly on the time scale of the simulation, as does the point particle (and the radii in between).

Another application of Eq. 2.15 is a direct method for comparing the free energy between two crystalline phases developed by Bruce and Wilding.[10] In this lattice switch method, originally applied to the fcc/hcp problem in hard spheres, the particles are at positions

$$\mathbf{r}_i = \mathbf{R}_{q,i} + \mathbf{d}_i \tag{2.16}$$

where $\mathbf{R}_{q,i}$ is the perfect lattice position for particle i and $\mathbf{d}_i$ is the displacement of the actual particle with respect to its perfect lattice position. Normal sampling is done in $\mathbf{d}_i$ with an extra degree of freedom: the choice in lattice positions $\mathbf{R}^N_{q,i}$, connecting two crystalline phases. Now state a is defined as having the set of lattice positions $\mathbf{R}^N_{a,i}$ and state be as having the set of lattice positions $\mathbf{R}^N_{b,i}$ and free energy differences can be calculated directly. This method is used in chapter 3 to compare the free energy of a crystal with two interfaces between stacking types, to one with four interfaces.

2.1.3 Multicanonical Sampling

It is to be expected that the probability of accepting a lattice switch as described above is low. In general, there might be values for λ in Eq. 2.12 that have a high free energy and therefore low probability, yet, we still need to sample those areas of phase space to connect the states we are interested in.

The solution is to bias the Boltzmann distribution by simply making the low-probability λ values more probable. We can add a weight factor $W(\lambda)$ to the free

energy in Eq. 2.12 and sample

$$\begin{aligned} F'(\lambda,N,V,T,\{W\}) &= F(\lambda,N,V,T)+W(\lambda) \\ &= -k_BT\ln\Big(Q(\lambda,N,V,T)\exp[W(\lambda)]\Big) \\ &= -k_BT\ln\int d\mathbf{r}^N\delta\left(\lambda-\lambda(\mathbf{r}^N)\right)\times \\ &\quad \exp\left[W(\lambda)-\beta U(\mathbf{r}^N)\right] \end{aligned} \tag{2.17}$$

which means that the probability of a micro-state is now modified by an amount depending on the order parameter value λ; instead of Metropolis sampling based on the acceptance probability determined by $\min\{1,\exp(-\beta\Delta U)\}$, we sample with acceptance probability based on $\min\{1,\exp[-\beta\Delta U+\Delta W(\lambda)]\}$. With this biased ensemble we sample a histogram $P'(\lambda|N,V,T)$ from which we can unfold the bias by

$$P(\lambda|N,V,T)\propto P'(\lambda|N,V,T)\exp[-W(\lambda)] \tag{2.18}$$

to either get a free energy profile up to a constant $F(\lambda,N,V,T)+\Delta=-k_BT\ln P(\lambda)$ or a free energy difference from Eq. 2.15.

The smallest variance in values of $P'(\lambda)$ is obtained when it is a flat distribution; i.e. when $W(\lambda)=-\exp[F(\lambda,N,V,T)]$. Now, $F(\lambda,N,V,T)$ is precisely the quantity we are after, so it has to be approximated iteratively. Using the histogram $P'_i(\lambda)$ obtained from simulation iteration i, we get the new weights for step $i+1$

$$W_{i+1}(\lambda)=W_i(\lambda)-\ln P'_i(\lambda)+c \tag{2.19}$$

Of course, this makes very little use of the information from previous steps and does not take into account relative uncertainties; better methods for obtaining weights are described in Ref. 43. In practice though, the simple updating scheme of Eq. 2.19 is quite effective for quickly exploring previously unsampled areas of the $P(\lambda)$ histogram, especially with a little over-damping.

Multicanonical sampling is applied to the lattice switch method for hard spheres as follows: an overlap parameter $M_r(\mathbf{d}^N)$ is introduced which counts the number of 'virtual overlaps': the number of overlaps one would have if one would switch from the current underlying lattice $\mathbf{R}^N_{q,i}$ to lattice $\mathbf{R}^N_{r,i}$. If $q=r$ then $M_r(\mathbf{d}^N)=0$, but if it is not, it is usually bigger than zero. Now the order parameter which is used as a basis of the bias is

$$L(\mathbf{r}^N)=M_a(\mathbf{r}^N)-M_b(\mathbf{r}^N) \tag{2.20}$$

so a lattice switch is accepted only if $L(\mathbf{r}^N)=0$. Because of the multicanonical sampling, this state is actually sampled and the switch is actually performed during the simulation; a state with an unbiased probability of $\mathcal{O}(10^{-150})$ for 1728 particles, as can be seen in chapter 3.

2.2 Elasticity

Elasticity, the linear response of a solid body to an applied deformation, is important not only for the study of the mechanics of materials: it also plays an important

role in modeling the concentration of various types of defects. As will be shown in Chapter 5, the equilibrium concentration of interstitials can be estimated using a simple model involving a shear elastic constant. In addition, the free energy of dislocations in 2D depends strongly on Young's modulus, a combination of the second-order elastic constants. If the 2D Young's modulus drops below a certain universal value, the free energy of free dislocations goes to zero and a continuous phase transition can occur. This prediction forms the basis for the study of polydisperse disks in chapter 7.

In our daily experience, elasticity is the restoring force (stress) of a solid to an applied deformation (strain). In a statistical mechanical sense, it is related to the increase in free energy with applied strain. Imagine the particle coordinate of particle i in the undeformed system, r_k^i, which are deformed through a homogeneous deformation

$$r_k'^i = \alpha_{kl} r_l^i \equiv (\upsilon_{kl} + \delta_{kl}) r_l^i \tag{2.21}$$

(where we employ the Einstein summation convention) with deformation matrix α_{kl} and displacement gradient υ_{kl}. Now, the free energy of a many-body system should be rotationally invariant and the change in free energy upon deformation can only depend on the change in the distances between particles. This implies that the free energy should not be expressed as a function of the strains α_{kl}, but of the *Lagrangian strain parameters* ηkl. The Lagrangian strains are related to the α_{kl} through

$$\eta_{kl} = \tfrac{1}{2}(\alpha_{mk}\alpha_{ml} - \delta_{kl}) = \tfrac{1}{2}(\upsilon_{kl} + \upsilon_{lk} + \upsilon_{mk}\upsilon_{ml}) \tag{2.22}$$

The change in *distance* between any two particles i and j ($\Delta_k^{ij} = r_k^i - r_k^j$), can be expressed in terms of the Lagrangian strains:

$$\begin{aligned} 2\eta_{kl}\Delta_k^{ij}\Delta_l^{ij} &= (\alpha_{mk}\alpha_{ml} - \delta_{kl})\Delta_k^{ij}\Delta_l^{ij} \\ &= \alpha_{mk}\alpha_{ml}\Delta_k^{ij}\alpha_{mk}\alpha_{ml}\Delta_l^{ij} - \Delta_k^{ij}\Delta_k^{ij} \\ &= \Delta_m'^{ij}\Delta_m'^{ij} - \Delta_k^{ij}\Delta_k^{ij} \\ &= \sum_m \left|\Delta_m'^{ij}\right|^2 - \sum_k \left|\Delta_k^{ij}\right|^2 \end{aligned} \tag{2.23}$$

In other words, the change in distance between two particles i and j only depends on the original positions r_k and the Lagrangian strain parameters η_{kl}; in particular, the elastic free energy should depend on them. In an expansion around small deformation, we can write

$$\begin{aligned} F(\eta_{kl})/V &= F(\mathbf{0})/V + C_{kl}\eta_{kl} + \tfrac{1}{2}C_{klmn}\eta_{kl}\eta_{mn} \\ &\quad + \frac{1}{3!}C_{klmnop}\eta_{kl}\eta_{mn}\eta_{op} + \cdots \end{aligned} \tag{2.24}$$

where V is the density at zero deformation. The second-order elastic constants, C_{klmn} are what is usually referred to as 'the elastic constants'. (The values C_{kl} should either be 0 or reflect the imposed thermodynamic control parameters when

kl	11	22	33	23 or 32	13 or 31	12 or 21
α	1	2	3	4	5	6

Table 2.1: Voigt indices for elastic constants.

expanding around equilibrium to satisfy the requirement that the free energy should be minimal at zero strain).

Apart from the strain, our daily experience with elasticity is connected to the restoring force. The stress is the force f_k per surface area ds_l,

$$f_k = T_{kl} ds_l \tag{2.25}$$

and is, as is shown in appendix A, in free energy terms equal to

$$T_{kl} = \frac{1}{V'} \alpha_{km} \alpha_{ln} \left(\frac{\partial F}{\partial \eta_{mn}} \right) \tag{2.26}$$

Note that the components of C_{kl} are just the stress tensor *at zero deformation*, and are $C_{kl} = -\delta_{kl} P$ for isotropic pressure P.

Using Eqs. 2.24 and 2.26, we can derive a generalization of Hooke's law; expanding the stress tensor around zero deformation

$$\begin{aligned} \left. \frac{\partial T_{kl}}{\partial \alpha_{mn}} \right|_{\alpha_{kl}=\delta_{kl}} &= \left. \frac{\partial \frac{1}{V'} \alpha_{ko} \alpha_{lp} (\partial F / \partial \eta_{op})}{\partial \alpha_{mn}} \right|_{\alpha_{kl}=\delta_{kl}} \\ &= \left. \frac{\partial J^{-1} \alpha_{ko} \alpha_{lp} \left(C_{mn} + \frac{1}{2} C_{mnop} [\alpha_{qo} \alpha_{qp} - \delta_{op}] + \cdots \right)}{\partial \alpha_{mn}} \right|_{\alpha_{kl}=\delta_{kl}} \end{aligned} \tag{2.27}$$

where we used the fact that $V'/V = J = \det \alpha_{kl}$, ($J$ is the Jacobian of the transformation α_{kl}). Around zero deformation $\alpha_{kl} = \delta_{kl}$, $\alpha^{-1} = \delta_{kl}$ and $T_{kl} = C_{kl}$: a somewhat tedious calculation gives us

$$\left. \frac{\partial T_{kl}}{\partial \alpha_{mn}} \right|_{\alpha_{kl}=\delta_{kl}} = (C_{kn} \delta_{lm} + C_{ln} \delta_{km} - C_{kl} \delta_{mn}) + C_{klmn} \tag{2.28}$$

with Jacobi's identity $\partial J / \partial \alpha_{kl} = \alpha_{kl}^{-1} J$. A similar (but even more tedious) derivation can be done for the second derivative of T_{kl} to get terms containing the third-order elastic constants, as is done in chapter 4. The inverse of the derivative[†] above (the strain derived as a function of stress) defines the components of the *compliance* S_{klmn}:

$$S_{klmn} = \left. \frac{\partial \alpha_{kl}}{\partial T_{mn}} \right|_{\alpha_{kl}=\delta_{kl}} \tag{2.29}$$

[†]This is only true in the case of isotropic pressure, see Wallace[44] for details

From the elastic free energy in Eq. 2.24, it is clear that not all 3^4 elastic constants C_{klmn}, nor all 3^2 components of C_{kl} are independent. Because η_{kl} is symmetric and derivatives are independent, the components of C_{kl}, C_{klmn}, C_{klmnop}, etc. satisfy the *Voigt symmetry*; for example

$$C_{klmn} = C_{lkmn} = C_{klnm} = C_{mnkl} \tag{2.30}$$

For shorter notation, we can instead use the Voigt notation $C_{\alpha\beta} \equiv C_{klmn}$, which uses this symmetry to replace two indices with one Voigt index; see Table 2.1 for the full list of Voigt indices. The values for 3D elastic constants in this thesis — and in most literature on 3D elasticity — are reported using Voigt notation.

For systems with symmetries, such as the cubic symmetry of fcc and the hexagonal symmetry of hcp, the number of independent elastic constants can be further reduced; for example, the values of C_{11}, C_{22} and C_{33} should be the same for fcc in the frame of reference of its cubic symmetry. In total, there are only three independent elastic constants for fcc: C_{11}, C_{12} and the shear elastic constant C_{44}; all other elastic constants are the same as the three above or zero (for example C_{14}). In two dimensions, the common hexagonal crystal has two elastic constants, just as the isotropic case:[45] C_{11} and C_{12}.

2.2.1 2D Isotropic and Hexagonal Systems

For two-dimensional systems with hexagonal symmetry or isotropic systems, the free energy expansion at isotropic pressure of Eq. 2.24 has only two independent elastic constants and reduces — up to the second order — to

$$\begin{aligned} \Delta F(\eta_{kl})/V &= -P(\eta_{11}+\eta_{22}) \\ &\quad +\tfrac{1}{2}C_{11}(\eta_{11}^2+\eta_{22}^2+2\eta_{12}^2) \\ &\quad +C_{12}(\eta_{11}\eta_{22}-\eta_{12}^2) \end{aligned} \tag{2.31}$$

(note that $C_{44} = \frac{1}{2}(C_{11}-C_{12})$), while, traditionally the free energy functional for arbitrary deformation has been defined as

$$\begin{aligned} \Delta F(u_{kl})/V &= -P(u_{11}+u_{22}) + \tfrac{1}{2}\lambda_L(u_{ii})^2 + \mu_L u_{kl}^2 \\ &= -P(u_{11}+u_{22}) \\ &\quad +\tfrac{1}{2}\lambda_L(u_{11}^2+u_{22}^2+2u_{11}u_{22}) \\ &\quad +\mu_L(u_{11}^2+u_{22}^2+2u_{12}^2) \end{aligned} \tag{2.32}$$

with λ_L and μ_L as the bulk and shear *Lamé coefficients*. Crucially, u_{kl} is defined as the Lagrangian strain without quadratic components of the displacement matrix

$$u_{kl} = \tfrac{1}{2}\left(\upsilon_{kl}+\upsilon_{lk}\right) \tag{2.33}$$

When we expand Eq. 2.31 up to quadratic terms in υ_{kl} (for small deformations) we get

$$\Delta F(u_{kl})/V = -P(u_{11}+u_{22})$$

$$
\begin{aligned}
&-\tfrac{1}{2}P(u_{11}^2+u_{22}^2+4u_{12}^2-2v_{12}v_{21})\\
&+\tfrac{1}{2}C_{11}(u_{11}^2+u_{22}^2+2u_{12}^2)\\
&+C_{12}(u_{11}u_{22}-u_{12}^2)
\end{aligned}
\tag{2.34}
$$

which equates the Lamé elastic constants to

$$
\begin{aligned}
\lambda_L+2\mu_L &= C_{11}-P\\
\mu_L &= \tfrac{1}{2}(C_{11}-C_{12})-P=C_{44}-P
\end{aligned}
\tag{2.35}
$$

2.2.2 Computer Simulations

To calculate the elastic constants using molecular simulations, there are three basic methods: direct free energy calculations, which directly calculate the free energy change as a function of applied strain, stress-strain methods, where a system is deformed and the stress response to the deformation is calculated, and fluctuation methods.

Direct calculation of the free energy response to an applied strain has mostly been performed as a validatory method, as in Ref. 46 and in chapter 4, and are relatively expensive if the free energy is recalculated for each deformation.

The conceptually most straightforward way to calculate the elastic constants, the stres-strain methods, measure the stress as a function of a small applied strain. The second-order elastic constant are in this case a function of the derivative of the stress as function of strain through Eq. 2.28. Typically, for hard spheres, the maximum applied strain is less than 10^{-3} to keep the stress response linear enough (for second-order elastic constants).

The stress tensor can be calculated in a simulation — similarly to the virial pressure — with (see appendix A)

$$
\begin{aligned}
T_{kl} &= \frac{k_BT\delta_{kl}}{V}-\frac{1}{V}\left\langle\sum_{i=1}^{N}f_k^{\mathrm{int},i}r_l^i\right\rangle\\
&= \frac{k_BT\delta_{kl}}{V}-\frac{1}{V}\left\langle\sum_{i=1}^{N}\sum_{j<i}U'(r^{ij})\frac{r_k^{ij}r_l^{ij}}{|r^{ij}|}\right\rangle
\end{aligned}
\tag{2.36}
$$

where $f_k^{\mathrm{int},i}$ is the total inter-particle force that particle i experiences on coordinate index k, the inter-particle distance $r_k^{ij}\equiv r_k^i-r_k^j$, and $U'(r^{ij})=\partial U(r^i,r^j)/\partial r^{ij}$ with $U(r^i,r^j)$ as the inter-particle potential between particles i and j. For hard particles (for which the inter-particle potentials are nondifferentiable) this can only be done directly in an MD simulation, where a time average of the average momentum exchange is equal to the average of the force[47]

$$
\begin{aligned}
\left\langle\sum_{i=1}^{N}f_k^{\mathrm{int},i}r_l^i\right\rangle &= \lim_{\tau\to\infty}\frac{1}{\tau}\int_0^\tau\sum_{i=1}^{N}m\frac{\partial p_k^i}{\partial t}r_l^i\,dt\\
&= \lim_{\tau\to\infty}\frac{1}{\tau}\sum_{\mathrm{coll}(i,j)}m\Delta p_k^{ij}r_l^{ij}
\end{aligned}
\tag{2.37}
$$

where $\Delta p_k^{ij} = p_k^i(t+\varepsilon) - p_k^i(T-\varepsilon)$, the difference in momentum before and after a collision involving particles i and j, or zero if there was no collision. The last term involves a sum over all collisions and uses Newton's third law ($\Delta p_l^{ij} = -\Delta p_l^{ji}$). Like for the pressure, the ensemble average of Eq. 2.36 can be approximated using extrapolation of a radial distribution-like function[48] for use in a MC simulation; this method, however, is relatively cumbersome.

From the expansion of the free energy around the strain it could be noted that the second-order elastic constants play the role of an inverse compressibility: just like the inverse isothermal compressibility can be seen as a second derivative of the free energy in the canonical ensemble:

$$\frac{1}{\kappa_T} = -\frac{1}{V}\left(\frac{\partial P}{\partial V}\right)_T = \frac{1}{V}\left(\frac{\partial^2 F}{\partial V^2}\right)_T \tag{2.38}$$

we have by definition from Eq. 2.24

$$C_{klmn} = \frac{1}{V}\frac{\partial^2 F}{\partial \eta_{kl}\eta_{mn}} \tag{2.39}$$

(Incidentally, using Eq. 2.29 it is straightforward to show[44] that the compressibility is $\kappa_T = S_{kkll}$). This second derivative has been evaluated by Squire, Holt and Hoover[49] (following an original derivation by Born and Huang, but with cross-terms) for the case of particles with pairwise interactions and becomes

$$\begin{aligned} C_{klmn} \;=\; & \frac{2Nk_BT\delta_{km}\delta_{ln}}{2} \\ & + \frac{1}{Vk_BT}\left\{ \left\langle \sum_{<i,j>} U'(r^{ij})\frac{r_k^{ij}r_l^{ij}}{|r^{ij}|} \right\rangle \left\langle \sum_{<i,j>} U'(r^{ij})\frac{r_m^{ij}r_n^{ij}}{|r^{ij}|} \right\rangle \right. \\ & \left. - \left\langle \sum_{<i,j>} U'(r^{ij})\frac{r_k^{ij}r_l^{ij}}{|r^{ij}|} \sum_{<i,j>} U'(r^{ij})\frac{r_m^{ij}r_n^{ij}}{|r^{ij}|} \right\rangle \right\} \\ & + \frac{1}{V}\left\langle \sum_{<i,j>} U''(r^{ij})\frac{r_k^{ij}r_l^{ij}r_m^{ij}r_n^{ij}}{|r^{ij}|^2} \right\rangle \\ & - \frac{1}{V}\left\langle \sum_{<i,j>} U'(r^{ij})\frac{r_k^{ij}r_l^{ij}r_m^{ij}r_n^{ij}}{|r^{ij}|^3} \right\rangle + \frac{2Nk_BT}{V}\delta_{kn}\delta_{lm} \end{aligned} \tag{2.40}$$

where the term between braces contains fluctuations of the stress tensor. Similarly, the fluctuations in the isotensic ensemble, in which the stress T_{kl} is fixed and the strain is allowed to fluctuate,[50,51,52] are related to the elastic constants:

$$S_{klmn} = \frac{k_BT}{V'}\langle \eta_{kl}\eta_{mn}\rangle \tag{2.41}$$

The fluctuation methods use these relations to calculate all the elastic constants in a single simulation. The oldest method by Squire et al.[49] uses the stress fluctuations of Eq. 2.40 in an NVT ensemble. Because this method needs derivatives of

the inter-particle potential it can not be used directly for hard particles. An adaptation for hard spheres has been developed by Farago and Kantor[53] which involves taking a limit on an approximating potential.

Unfortunately, the fluctuation methods seem to suffer from equilibration problems[52] or poor convergence[54,55] due to slow relaxation of box size or microscopic stress. The work of Sprik et al.,[52] but also the quoted number of simulation steps in other work[46] seems to suggest that the stress-strain method is more efficient.

Appendix A: Force and the Stress Tensor

To make the connection between the stress tensor as defined in Eq. 2.25 and its expression in terms of the free energy in Eq. 2.26, we calculate the virtual work done on an arbitrarily strained body when it undergoes a virtual deformation, following Wallace's[44] derivation. We imagine an arbitrarily deformed material with particle points $r_k'^N$ bounded by a surface $\mathbf{s}$ into volume V', we define the stress T_{kl} by the force f_k acting on surface element ds_l.

$$f_k = T_{kl} ds_l \tag{2.42}$$

undergoing a further, virtual displacement of the surface element ds_l with an amount of $\Delta r_k'$. This virtual deformation corresponds to a virtual change in the displacement gradient υ_{kl} (see Eq. 2.21) and α_{kl}

$$\begin{aligned} r_k' + \Delta r_k' &= (\delta_{kl} + \Delta\upsilon_{kl}) r_l' \\ &= (\delta_{kl} + \Delta\upsilon_{kl}) \alpha_{lm} r_m \\ &= (\alpha_{kl} + \Delta\alpha_{kl}) r_l \end{aligned} \tag{2.43}$$

so $\Delta\alpha_{kl} = \Delta\upsilon_{kl}\alpha_{kl}$. The deformation amounts to a virtual work of

$$f_k \Delta r_k' = T_{kl} ds_l \Delta\upsilon_{km} r_m' \tag{2.44}$$

which, for the whole material, is the integral over the surface $\mathbf{s}$:

$$\begin{aligned} \Delta W &= \int_{\mathbf{s}} T_{kl}\Delta\upsilon_{km} r_m' ds_l \\ &= \int_{\mathbf{V}'} T_{kl}\Delta\upsilon_{kl} d\nu \\ &= V' T_{kl}\Delta\upsilon_{kl} \\ &= V' T_{kl}\Delta\tfrac{1}{2}(\upsilon_{kl} + \upsilon_{lk}) \\ &= V' T_{kl}\Delta\eta_{mn}\alpha_{mk}^{-1}\alpha_{nl}^{-1} \end{aligned} \tag{2.45}$$

where we employed Gauss's theorem from step one to two, the next-to-last step can be done because the stress tensor T_{kl} is symmetric and the last step because the change in Lagrangian strain can be expressed in terms of $\Delta\upsilon_{kl}$ as

$$\begin{aligned} \Delta\eta_{kl} &= \tfrac{1}{2}(\alpha_{mk}\Delta\alpha_{ml} + \Delta\alpha_{mk}\alpha_{ml}) \\ &= \tfrac{1}{2}(\alpha_{mk}\Delta\upsilon_{mn}\alpha_{nl} + \Delta\upsilon_{mn}\alpha_{nk}\alpha_{ml}) \\ &= \tfrac{1}{2}\alpha_{mk}\alpha_{nl}(\upsilon_{mn} + \upsilon_{nm}) \end{aligned} \tag{2.46}$$

Now, because for reversible changes

$$dU = dW + TdS \tag{2.47}$$

we get for the canonical ensemble ($F = U - TS$)

$$dF/V' = T_{kl}\alpha_{mk}^{-1}\alpha_{nl}^{-1}d\eta_{mn} \tag{2.48}$$

or

$$T_{kl} = \frac{1}{V'}\alpha_{km}\alpha_{ln}\left(\frac{\partial F}{\partial \eta_{mn}}\right) \tag{2.49}$$

which brings us back to the C_{kl} of Eq. 2.24 at zero deformation.

We will now extend the virial theorem[56] to give a microscopic definition of the stress in terms of particle interactions. For this derivation it is convenient to use time averages rather than ensemble averages; the ergodicity hypothesis

$$\begin{aligned}\langle A\rangle &= \frac{\int dp^N dr^N A\left(p^N, r^N\right)\exp\left[-\beta U(p^N, r^N)\right]}{\int dp^N dr^N \exp\left[-\beta U(p^N, r^N)\right]} \\ &= \lim_{\tau\to\infty}\frac{1}{\tau}\int_0^\tau A\left(p^N[t], r^N[t]\right)dt\end{aligned} \tag{2.50}$$

is a central concept in the connection of statistical mechanics to thermodynamics. An example of a thermodynamic average is the connection between temperature and mean particle momentum

$$\frac{1}{3Nmk_B}\left\langle\sum_{i=1}^N p_k^i p_k^i\right\rangle = T \tag{2.51}$$

Now, we will calculate the average of an extended Clausius virial equation

$$\mathscr{V}_{kl} = \sum_{i=1}^N f_k^i r_l^i \tag{2.52}$$

with f_k^i as the total force experienced by particle i in direction k. The time average of this quantity is

$$\begin{aligned}\left\langle\mathscr{V}_{kl}\right\rangle &= \lim_{\tau\to\infty}\frac{1}{\tau}\int_0^\tau\sum_{i=1}^N f_k^i r_l^i dt \\ &= \lim_{\tau\to\infty}\frac{1}{\tau}\int_0^\tau\sum_{i=1}^N m\frac{\partial^2 r_k^i}{\partial t^2}r_l^i dt \\ &= -\lim_{\tau\to\infty}\frac{1}{\tau}\int_0^\tau\sum_{i=1}^N m\frac{\partial r_k^i}{\partial t}\frac{\partial r_l^i}{\partial t}dt \\ &= -\frac{1}{Nm}\lim_{\tau\to\infty}\frac{1}{\tau}\int_0^\tau\sum_{i=1}^N p_k^i p_l^i dt \\ &= -k_B T\delta_{kl}\end{aligned} \tag{2.53}$$

where step two to three involves an integration by parts and Eq. 2.51 is used in the last step, keeping in mind that velocities in each direction are uncorrelated. We can now separate the force f_k^i into internal forces (from the interaction between the particles) and external forces (from the interaction of the particles with the surface **s**)

$$\begin{aligned} f_k^i &= f_k^{\text{int},i} + f_k^{\text{ext},i} \\ &= \sum_{j\neq i} \frac{\partial U(r^{ij})}{\partial r^{ij}} \frac{r_k^{ij}}{|r^{ij}|} + f_k^{\text{ext},i} \\ &= \sum_{j\neq i} U'(r^{ij}) \frac{r_k^{ij}}{|r^{ij}|} + f_k^{\text{ext},i} \end{aligned} \tag{2.54}$$

where $r_k^{ij} \equiv r_k^i - r_k^j$ and we assume the particles to interact solely through pair potentials. The external forces are now given by the stress tensor as in Eq. 2.42 over the surface area ds_m, and are $T_{km}ds_m$ for the k coordinate index, so, using Gauss's theorem again (and assuming homogeneous stress over the volume)

$$\int_{\mathbf{s}} T_{km} r_l ds_m = \int_V T_{kl} d\nu = V T_{kl} \tag{2.55}$$

which allows us to rewrite Eq. 2.53 as

$$\begin{aligned} T_{kl} &= \frac{k_B T \delta_{kl}}{V} - \frac{1}{V} \left\langle \sum_{i=1}^{N} \sum_{j\neq i} U'(r^{ij}) \frac{r_k^{ij}}{|r^{ij}|} r_l^i \right\rangle \\ &= \frac{k_B T \delta_{kl}}{V} - \frac{1}{V} \left\langle \sum_{i=1}^{N} \sum_{j<i} U'(r^{ij}) \frac{r_k^{ij} r_l^{ij}}{|r^{ij}|} \right\rangle \end{aligned} \tag{2.56}$$

where the last step is done using Newton's third law. This connects the microscopic positions and inter-particle forces to the homogeneous stress tensor.

3 Stacking Faults in Hard Sphere Crystals

The freezing of hard spheres is one of the most dramatic illustrations that the emergence of crystalline order can be entropy driven. Ever since the early simulations of Alder and Wainwright[2] and Wood and Jacobson,[3] hard-sphere freezing has been studied extensively, both theoretically[13,57,58,59] and experimentally.[60,61] Hard spheres can occur in two different crystal structures, face-centered cubic (fcc) and hexagonal close-packed (hcp). These two phases differ in the stacking of the hexagonal close-packed [111] layers. The fcc phase has *ABCABC*... stacking, while the hcp phase has *ABABAB*... stacking. Of the two crystal structures, the fcc phase is the most stable. Recent simulations suggest that, at the melting density ($\rho/\rho_0 \approx 0.736$, where ρ_0 is the density at regular close packing) the fcc phase is more stable than hcp by an amount of the order of $90 \pm 20 \cdot 10^{-5} k_B T$ per particle.[9,10] As the free-energy difference between the two phases is very small, the spontaneous generation of stacking faults is quite common. In fact, recent experiments on the crystallization of hard-sphere colloids under micro-gravity conditions or in a density matched system found that randomly stacked hexagonal close-packed (rhcp) crystallites were formed.[30,31,26,27] Yet, there is experimental evidence that, in slowly grown crystallites, the fcc phase is favored over the hcp phase, and fcc stacking of hexagonal close-packed [111] planes occurs with a higher than random probability.[62,31,26,27] The aim of the present paper is to estimate the driving force for the formation of a pure fcc phase from the randomly stacked phase. Using some simple assumptions about the rate of crystal growth, we can then arrive at an estimate of the growth velocity of essentially pure fcc crystals from a polycrystalline mixture of randomly stacked crystals. Our main conclusion is that the driving force, although weak, is large enough to account for a growth rate of fcc crystals that is of the order of Ångstrøms per second. In other words, for a typical hard-sphere colloid, it would take months to transform a 1-millimeter crystallite from rhcp to fcc. For a 50-100 μ crystallite, the time would be days, rather than months. The presence of gravity strongly influences the dynamics of crystal growth and the resulting hard sphere stackings.[26,27] Gravity may also be exploited by, for example, using colloidal epitaxy; see Ref. 28 and Chapter 4 for an application and its possible influence on stacking.

To estimate the rate at which the fcc phase grows from the rhcp phase, we need to estimate the relative free energy of the latter. The free energy of the rhcp phase contains several ingredients: first of all, $\Delta f = f_{\mathrm{hcp}} - f_{\mathrm{fcc}}$, the difference in bulk free

energies per particle of the pure fcc and hcp phases. Secondly, the interfacial free energy $\gamma_{\mathrm{hcp-fcc}}$, which is the measure of the additional free-energy cost to create an fcc-hcp interface. And thirdly, the stacking entropy of the rhcp phase ($k_B \ln 2$ per plane). Although Δf is known from recent simulations,[9,10] its value has been subject to debate.[58,59,9,10] We therefore recomputed it using two different techniques. We find that the different approaches do indeed yield the same answer. To compute $\gamma_{\mathrm{hcp-fcc}}$ we used a lattice-switch Monte Carlo technique that is described in some detail below. Finally, to estimate the actual growth rate, we make use of the version of the Wilson-Frenkel law,[63] as applied to colloids by several authors.[13,57,60,61]

3.1 Lattice Switch Monte Carlo

To compute the free energy of the fcc-hcp interface, we used the lattice-switch method proposed by Bruce and Wilding.[10] This method is particularly suited to compute the free-energy difference between two different solid structures, provided they have the same number of degrees of freedom. As a test, we used the same method to compute the free-energy difference between the bulk fcc and hcp phases. In the lattice-switch simulations, we consider two realizations of the crystal structure that are related through a simple one-to-one particle mapping. The configuration of the system is denoted by an index α. The particle positions in configuration α ($\in \{\mathbf{a},\mathbf{b}\}$) are denoted by $\vec{X}_i^{\alpha} + \vec{\delta}_i$, where $\vec{X}_i^{\alpha}$ is the lattice position for particle i in configuration α, and $\vec{\delta}_i$ is the displacement relative to its lattice position. The different crystalline configurations differ in their lattice positions $\vec{X}_i^{\alpha}, i = 1 \ldots N$.

We can define a global partition function, $Z(N,V,T)$ as the sum of the partial partition functions for the different configurations α:

$$Z(N,V,T) = \sum_{\alpha} Z(N,V,T,\alpha) = \sum_{\alpha} \int_V d\vec{\delta}_i \prod_i e^{-\Phi(\vec{\delta}_i,\alpha)} \tag{3.1}$$

where Φ represents the configurational energy in units $k_B T$. If the system can switch between different configurations by replacing the lattice positions $\vec{X}_i$ but retaining the displacements $\vec{\delta}_i$, the probability of finding the system in configuration α is

$$P(\alpha|N,V,T) = \frac{Z(N,V,T,\alpha)}{Z(N,V,T)} \tag{3.2}$$

The Helmholtz free energy of configuration α is

$$f_\alpha \equiv N^{-1} F_\alpha \equiv N^{-1} k_B T \ln Z(N,V,T,\alpha) \tag{3.3}$$

and the free energy difference between two configurations $\alpha = \{\mathbf{a},\mathbf{b}\}$ can be written as

$$\Delta f = \frac{k_B T}{N} \ln \frac{P(\mathbf{a}|N,V,T)}{P(\mathbf{b}|N,V,T)} \tag{3.4}$$

The probabilities $P(\alpha|N,V,T)$ are sampled using the histogram method of Ref. 10.

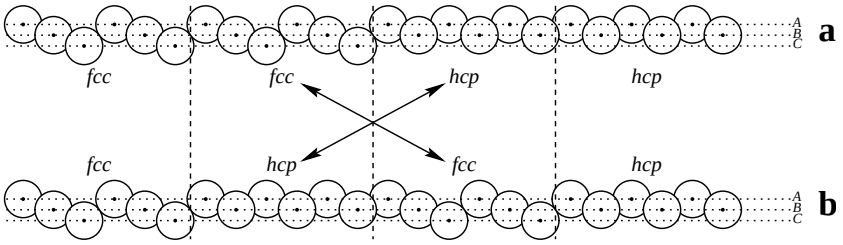

Figure 3.1: Side view of the two configurations **a** and **b** between which the free energy difference is calculated to calculate the interfacial free energy. The configurations are divided into four pieces and the middle quarters of the configurations are swapped so that configuration **a** has two interfaces between fcc and hcp, and configuration **b** has four. Note that the view is with the hexagonal layers upright and perpendicular to the paper and that periodic boundary conditions are used.

For the calculations on the free energy difference between fcc and hcp structures we have used an fcc crystal as configuration $\alpha = \mathbf{a}$ and an hcp crystal as configuration $\alpha = \mathbf{b}$. To calculate the interfacial free energy between fcc and hcp we have used a system where the layer stacking for configuration **a** is a crystal which has the first half of its hexagonal layers in fcc stacking and the second half in hcp. The stacking for configuration **b** has the middle two quarters swapped with respect to configuration **a**, creating a crystal which has four parts: fcc, hcp, fcc and hcp (See Fig. 3.1). In this situation, configuration **a** has two interfaces between fcc and hcp stacking, and **b** has four (with periodic boundary conditions), while the total size of the fcc and hcp parts remain the same.

We obtain the interfacial free energy density by computing the free energy difference between structures **a** and **b**, and dividing this difference by the difference in interfacial free area of **a** and **b**.

3.2 Results

Most simulations were performed at a reduced density of $\rho/\rho_0 = 0.7778$, (packing fraction $\eta = 0.5760$), a density somewhat higher than the melting density. This density was chosen because the system would become unstable at the melting point due to the histogram method which was used, and the density of $\rho/\rho_0 = 0.7778$ is the same as in Ref. 10. In all simulations, periodic boundary conditions were used.

We first calculated the free energy difference per particle between fcc and hcp stackings ($\Delta f_{\mathrm{hcp-fcc}}$). In Table 3.1 we present our results. In the same table, we also show show the free-energy difference at a reduced density of 0.736 (the melting density), as computed by Bolhuis et al.,[9] using the Einstein integration method[58] . Our results appear to disagree with those of Bruce and Wilding.[10] To verify our results, we also performed an Einstein integration on the 1728-particle system.

N	$\Delta f_{\text{fcc-hcp}}\ (10^{-5}k_BT)$	method
12096	90 ± 20	EI[9]
216	101 ± 4	LS[10]
1728	83 ± 3	LS[10]
5832	86 ± 3	LS[10]
216	132 ± 4	LS
1728	112 ± 4	LS
1728	113 ± 4	EI

Table 3.1: Simulation results on the free energy difference between fcc and hcp structures of the hard-sphere crystal. The system size is denoted by N. EI stands for Einstein integration, and LS for the lattice switch method.

However, our simulations were considerably longer than those of Ref. 10. The results of these simulations agreed to within the (very small) statistical error with the lattice switch method. We can use our results for $N = 216$ and $N = 1728$ to estimate $\Delta f_{\text{hcp}-\text{fcc}}$ in the limit $N \to \infty$. If we assume that finite-size corrections scale as $1/N$, then the results for $N = 1728$ are, to within the statistical error, equal to the results for the infinite system.

The calculation of the interfacial free energy was performed on a $12 \times 12 \times 24 = 3456$ particle system particle system at a reduced density $\rho/\rho_0 = 0.7778$. The total length of the simulation was $2.21 \cdot 10^{12}$ Monte Carlo cycles. The fcc-hcp interfacial free energy was found to be $25.9 \pm 5.6 \cdot 10^{-5} k_BT/\sigma^2$, with σ the particle diameter. In what follows, all free energies will be expressed in units of k_BT and all distances in units of the particle diameter σ, unless otherwise noted.

3.3 Discussion

Using the numerical data presented above, we can estimate the free energy difference between the stable fcc phase and the rhcp phase. If we assume that the stacking in the rhcp phase is truly random, then the free-energy difference per particle is

$$\Delta f_{\text{rhcp}-\text{fcc}} = 0.5\Delta f_{\text{hcp}-\text{fcc}} + 0.5\gamma_{\text{hcp}-\text{fcc}} s_0 - \ln 2/N_{layer} \tag{3.5}$$

where s_0 is the surface area per particle ($s_0 = (\sqrt{3}/2)(\rho_0/\rho)^{2/3}\sigma^2 \approx 1.02\sigma^2$, for $\rho/\rho_0 = 0.7778$) and N_{layer} is the number of particles in a single close-packed layer. In Eq. 3.5, we have assumed that the interfacial free energy does not depend on the density of stacking faults. This is almost certainly an approximation. However, as the stacking-fault free energy itself is small, the resulting error is probably negligible. Our simulations suggest that for small crystals (less than a thousand particles per plane) rhcp is more stable than fcc. Hence, only once the crystallites have grown beyond this size (corresponding to lateral dimensions of some ten microns for real colloidal crystals) can the slow annealing towards the stable phase commence. Let us therefore consider crystals that are sufficiently large that we can

ignore the stacking entropy. Then the driving force per particle to convert from rhcp to fcc is $0.5\Delta f_{\mathrm{hcp-fcc}} + 0.5\gamma_{\mathrm{hcp-fcc}} s_0$, which, in the present case, is approximately equal to $6 \cdot 10^{-4}$. Let us now consider the growth of fcc crystallites at the expense of rhcp crystallites. It is plausible to assume that fcc crystallites grow where a [111]-grain boundary of the fcc crystal is in contact with an rhcp crystal. In the case of colloidal crystal growth from solution, the velocity of the crystal front is, to a good approximation given by[63, 13, 57, 60, 61]

$$v_{cr} = \frac{\zeta D}{\Lambda}(e^{\Delta\mu/k_B T} - 1) \tag{3.6}$$

where $\Delta\mu$ is the chemical potential difference between liquid and solid, D is the (short-time) self-diffusion constant in the dense colloidal suspension, Λ is a characteristic distance over which a particle should diffuse in order to be incorporated in the crystal, and ζ is a factor of order one. In order to arrive at an estimate for v_{cr}, we assume that grain boundaries are liquid like, and the characteristic distance Λ is of the order of the particle diameter σ. Moreover, we replace $\Delta\mu$ by $\Delta f_{\mathrm{rhcp-fcc}}$. For a 200 nm colloid, a typical value for D would be $D \approx 2 \cdot 10^{-10}$ cm^2 s^{-1}. The resulting estimate for v_{cr} is $v_{cr} \approx 6 \cdot 10^{-9}$ cm s^{-1}. Hence, this rough estimate suggests that it would take several months to grow a 1 mm fcc crystal, starting from a rhcp crystallite. It is therefore hardly surprising that only random stacking was observed in the micro-gravity experiments of Zhu et al.[30] However, many studies of colloidal crystallization last months or even years. The present analysis suggests that the fcc crystallites observed under those conditions could indeed be 'true' hard-sphere crystal fcc phases. A second conclusion is that small crystallites (containing less than $30^3 \approx 3 \cdot 10^4$ particles) will never become fcc-like. Intermediate-sized crystallites (containing less than 100^3 particles) can be fcc-like, but will always have an appreciable equilibrium concentration stacking faults.

Recently, there have been several experiments focusing on hard-sphere stacking and its aging.[26, 28, 27] All of these studies find that fcc is the most favourable stacking; either it forms immediately under sedimentation[28] or it forms through slow annealing.[26, 27] Although gravitational stresses and small disturbances appear to strongly favour fcc through what appears to be shear-melting of hcp,[27] the density-matched systems, unaffected by gravity, seem to regrow rchp crystals as fcc crystals at a rate that is compatible with the rates predicted in this chapter.

4 Stacking and Elasticity

The simplest regular close-packed structures of hard, spherical particles are the face-centered cubic (fcc) and hexagonal close-packed (hcp) structures (see Fig. 1.1 on page 2 and Fig. 4.1). Close to melting, the Helmholtz free energies of these two crystal structures differ by less than 0.05% (see refs. 9, 10 and chapter 3). As a consequence, hard-sphere colloids (the experimental realization of elastic hard spheres) rarely crystallize directly into the more stable fcc structure. Rather, crystallization initially results in the formation of a randomly stacked crystal.[30,64] As explained in chapter 3, the latter then slowly transforms to the stable fcc structure. However, pure *hcp* crystals have recently been grown by colloidal epitaxy on patterned templates.[33] At a given density, not only the free energies, but also the pressures and compressibilities of the fcc and hcp phases are very similar. One might therefore be tempted to suppose that these two crystal phases are similar in *all* their thermodynamic properties. Surprisingly, this is not the case. In this Letter we present calculations of the elastic constants of fcc and hcp hard-sphere crystals. We show that some of these elastic constants may differ by as much as 20%. As a consequence, a moderate deformation of the hard-sphere crystal may change the relative stability of the two crystal phases.

4.1 Lattice Symmetries and Elasticity

A homogeneous deformation of a solid can be described by the transformation matrix α_{ij} that relates the cartesian coordinates x_j of a point in the undeformed solid, to the coordinates x'_i in the deformed solid: $x'_i = \alpha_{ij} x_j$, where summation of repeated indices is implied. The (isothermal) elastic constants of a crystal are most easily defined in terms of an expansion of the Helmholtz free energy $F(N,V,T)$ in powers of the Lagrangian strains η_{ij}:[44]

$$\begin{aligned} F(\eta_{ij})/V &= F(\mathbf{0})/V + T_{ij}(\mathbf{0})\eta_{ij} + \tfrac{1}{2}C_{ijkl}\eta_{ij}\eta_{kl} \\ &\quad + \tfrac{1}{6}C_{ijklmn}\eta_{ij}\eta_{kl}\eta_{mn} + \dots \end{aligned} \tag{4.1}$$

The Lagrangian strain parameters η_{ij} are related to the deformation matrix through $\eta_{ij} \equiv \frac{1}{2}(\alpha_{ki}\alpha_{kj} - \delta_{ij})$. In Eq. 4.1, the coefficients $T_{ij}(\mathbf{0})$ are simply the components of the stress tensor at zero deformation, C_{ijkl} are the second-order elastic constants, C_{ijklmn} are the third-order elastic constants, and so on. For a system under hydrostatic pressure P, the components of the stress tensor are $T_{ij} = -\delta_{ij}P$.

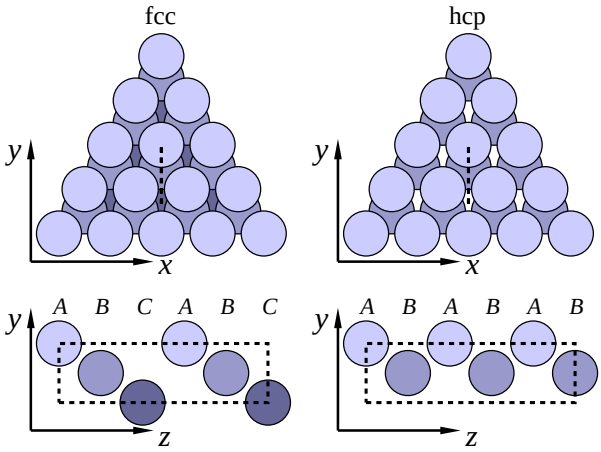

Figure 4.1: Sketch of the structures of the regular close-packed fcc crystal (left) and hcp crystal (right). Inequivalent close-packed layers are labeled with the letters A,B and, in the case of fcc, C. An fcc crystal has *ABCABC*... stacking and an hcp crystal has *ABABAB*... stacking. The c/a ratio is the distance between two close-packed layers divided by the distance between neighboring particles in a close-packed layer. The figures show the definitions of the *x*,*y* and *z* directions referred to in the text.

The fcc lattice has only 3 independent elastic constants[44] ($C_{1111} \equiv C_{11}$, $C_{1122} \equiv C_{12}$ and $C_{2323} \equiv C_{44}$ in the coordinate frame of the cubic unit cell). In what follows, we use this Voigt notation (C_{ij}) to denote the second-order elastic constants.

In order to compare the elastic constants of the fcc and hcp crystals, we used the coordinate system shown in Fig. 4.1, with the *x* and *y* directions in the hexagonal planes and the *z* direction perpendicular to these planes. For hcp (with hexagonal symmetry), there are six distinct elastic constants, five of which are independent.[44] To make a term-by-term comparison of the fcc and hcp elastic constant, it is convenient to ignore the full symmetry of the fcc crystal, and only use the fact that the crystal also has a lower rhombohedral symmetry. If the symmetry were really rhombohedral, the fcc crystal would have six independent elastic constants. But, if we take the full fcc symmetry into account, only three are linearly independent. The usual fcc elastic constants can be expressed as linear combinations of the rhombohedral elastic constants C'_{ij}: $C_{11} = 4C'_{11} - 3C'_{33}$, $C_{12} = C'_{33} + C'_{12} - C'_{11}$ and $C_{44} = C'_{33} - \frac{1}{2}(C'_{11} + C'_{12})$.

4.2 Simulations

We computed the elastic constants by calculating the stress response to a small applied strain, using molecular dynamics simulations.[65] At zero deformation, the

stress response of a system with isotropic pressure P is given by a generalization of Hooke's law:

$$\frac{\partial T_{ij}}{\partial \alpha_{kl}} = \left(\delta_{ij}\delta_{kl} - \delta_{il}\delta_{jk} - \delta_{jl}\delta_{ik}\right) P + C_{ijkl} \tag{4.2}$$

For the MD simulations, we used the event-based MD algorithm with cell lists, described by Rapaport.[66] The pressure tensor is calculated as the time average of the dyadic product of the collisional momentum exchange vector and the particle separation vector for each two-particle collision.[47]

We performed simulations for a range of amplitudes of each type of deformation. The second-order elastic constants were deduced from the linear part of the stress-strain relation. In principle, all elastic constants can also be calculated in a single simulation using fluctuation methods.[50,52,55] However, these methods suffer from slow convergence.[52] We found the stress-strain method to be the most efficient.

For some deformations, we also computed the third-order elastic constants from the second derivative of the stress tensor with respect to deformation:

$$\begin{aligned}\frac{\partial^2 T_{ij}}{\partial \alpha_{rs}\partial \alpha_{tu}} &= 2\delta_{tu}\delta_{rs}T_{ij} + (\delta_{it}\delta_{jr} + \delta_{ir}\delta_{jt})T_{su} \\ &\quad -\delta_{ut}(\delta_{ir}T_{js} + \delta_{jr}T_{is}) \\ &\quad -\delta_{sr}(\delta_{jt}T_{iu} + \delta_{it}T_{uj}) \\ &\quad -\delta_{ut}C_{ijrs} + \delta_{it}C_{ujrs} + \delta_{jt}C_{iurs} \\ &\quad -\delta_{sr}C_{ijtu} + \delta_{ir}C_{sjtu} + \delta_{jr}C_{istu} \\ &\quad +\delta_{rt}C_{ijsu} + C_{ijrstu}\end{aligned} \tag{4.3}$$

The third-order elastic constants C_{ijrstu} appear in the last term.

The simulations were performed on systems with $6\times6\times6 = 216$, $12\times12\times12 = 1728$ and $24\times24\times24 = 13824$ particles. The maximum applied strain at lower densities was $4\cdot10^{-3}$; higher densities required even smaller deformations to keep the stress response linear. The simulation equilibration time was $1\cdot10^4$ collisions per particle. Data were collected during typically $2\cdot10^6$ collisions per particle for the 216 particle system, and $6\cdot10^4$ collisions per particle for the 13292 particle system. For each deformation, 8 simulations were done at different strain amplitudes to check linearity of the stress response. The calculations of the stress-strain curve for each type of deformation involved simulations totaling $6.4\cdot10^9$ collisions (one week on an Athlon 1600+ CPU). The measured elastic constants between the melting point (packing fraction $\phi = 0.54329$[7]) and close packing are given in tables 4.1 and 4.2.

At all densities, the values of the fcc and hcp elastic constants differ significantly (see Fig. 4.2). The relative differences between the elastic constants appear to remain approximately constant over the entire density range. The largest difference between fcc and hcp (up to 20%) was found for C'_{12}. Yet, the compressibilities of the two phases are identical to within the measurement error. For instance, at

ϕ	N		C'_{11}	C'_{12}	C'_{13}	C'_{33}
0.543	13292	fcc	90.51(6)	13.56(7)	7.51(7)	96.7(1)
		hcp	87.39(8)	15.95(7)	7.7(1)	96.56(9)
		hcp	*87.0(1)*	*15.82(9)*	*7.83(8)*	*97.1(1)*
0.543	216	fcc	90.50(8)	13.8(1)	7.57(8)	97.0(1)
		hcp	87.39(7)	16.6(1)	7.56(9)	96.67(9)
0.550	216	fcc	99.41(9)	15.2(1)	8.4(1)	106.16(8)
		hcp	95.88(6)	17.9(1)	8.6(1)	106.1(1)
0.576	13292	fcc	146.42(8)	21.86(7)	12.1(1)	156.1(1)
		hcp	142.1(1)	25.64(7)	12.36(8)	155.78(9)
0.576	216	fcc	146.1(1)	21.8(2)	12.1(1)	156.3(3)
		hcp	141.8(1)	25.8(1)	12.44(9)	156.1(4)
0.628	216	fcc	366.4(6)	51.6(4)	26.4(5)	392(1)
		hcp	356.9(4)	60.3(6)	27.3(3)	390(1)
0.681	216	fcc	1463(3)	189(2)	89(2)	1563(3)
		hcp	1423(3)	223(3)	97(1)	1559(2)
0.733	216	fcc	$1.10(1)\cdot 10^5$	$1.28(1)\cdot 10^4$	$6.1(2)\cdot 10^3$	$1.17(2)\cdot 10^5$
		hcp	$1.08(1)\cdot 10^5$	$1.52(1)\cdot 10^4$	$5.4(1)\cdot 10^3$	$1.17(1)\cdot 10^5$

Table 4.1: Second-order elastic constants of fcc and hcp hard-sphere crystals at densities between the melting point and close packing. The values for the hcp structure with $c/a = \sqrt{8/3}$ are shown in upright font. The (almost identical) results for a fully relaxed c/a ratio ($c/a = \sqrt{8/3}\left(1 - 7.5\cdot 10^{-4}\right)$ at $\phi = 0.543$), are shown in italics.

ϕ	N		C'_{14}	C'_{44}
0.543	13292	fcc	-8.77(4)	32.22(6)
		hcp	0	33.79(4)
		hcp	*0*	*33.90(5)*
0.543	216	fcc	-8.75(6)	32.4(1)
		hcp	0	35.0(1)
0.550	216	fcc	-9.65(4)	35.76(4)
		hcp	0	37.38(7)
0.576	13292	fcc	-13.82(6)	52.33(5)
		hcp	0	54.56(4)
0.576	216	fcc	-14.3(1)	52.8(4)
		hcp	0	54.9(1)
0.628	216	fcc	-35.4(1)	133.7(2)
		hcp	0	138.2(1)
0.681	216	fcc	-145(2)	535(2)
		hcp	0	557(2)
0.733	216	fcc	$-1.05(3)\cdot 10^4$	$4.05(4)\cdot 10^4$
		hcp	0	$4.08(1)\cdot 10^4$

Table 4.2: Continuation of table 4.1.

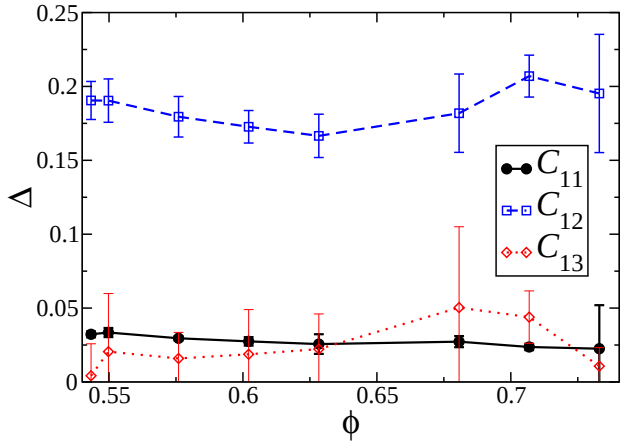

Figure 4.2: Relative difference $\Delta \equiv |C'^{\mathrm{fcc}}_{ab} - C'^{\mathrm{hcp}}_{ab}|/C'^{\mathrm{fcc}}_{ab}$ between fcc and hcp C'_{11}, C'_{12} and C'_{13} elastic constants as a function of packing fraction ϕ. The results shown were obtained in simulations of a system of 216 particles, with $c/a = \sqrt{8/3}$. The curves only serve as guides to the eye.

melting: $K^T_{fcc} = 0.02422(5)$ vs. $K^T_{hcp} = 0.02424(5)$ (for 1728 particles). We computed these compressibilities in two ways: (a) from the appropriate linear combination of elastic constants and (b) directly from the equation of state.[67] The results are the same, to within the statistical error. At the same density, the pressures of the fcc and hcp phases are also very similar: $P_{fcc} = 11.568(1)$ and $P_{hcp} = 11.571(1)$. Finally, the free energies differ only by about $1.12(4)\ 10^{-3} k_B T$ per particle (see chapter 3 and refs. 9, 10).

The difference between the fcc and hcp elastic constants is surprising because, already in 1967, Stillinger and Salsburg[68] had pointed out that a simple free-volume model predicts that the fcc and hcp elastic constants should be equal. However, they also showed that pair and triplet correlation effects can lead to differences.* Still, we were surprised by the magnitude of the computed differences, in particular for C'_{12}. To double-check our calculations of the elastic constants, we performed a second, fully independent calculation where we directly computed the free energy of the crystals in various states of deformation. The free energy of the (deformed and undeformed) crystals was calculated using a 20-point Einstein integration.[58,42] We found that the results obtained by the two methods were completely consistent. For example, in Fig. 4.3, we show the results of the two calculations for free energy change due to a deformation of the form

$$\alpha_{ij} = \begin{pmatrix} 1+\xi & 0 & 0 \\ 0 & 1/(1+\xi) & 0 \\ 0 & 0 & 1 \end{pmatrix} \tag{4.4}$$

*As the cell-cluster expansion converges poorly, its numerical predictions differ very considerably (more than 100%) from the simulation data.

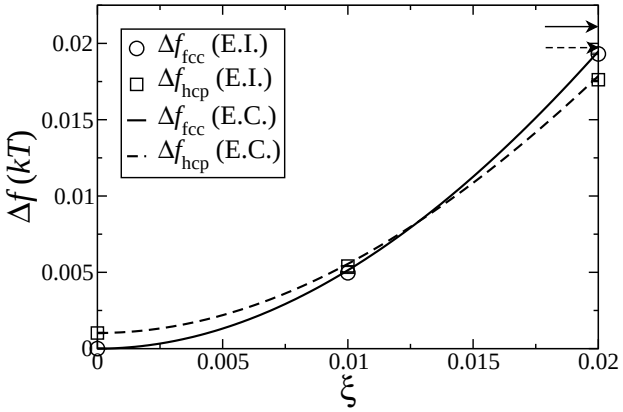

Figure 4.3: Variation of the fcc and hcp free energy with deformation ξ (see Eq. 4.4). The symbols indicate the results of Einstein free energy calculations (see text). The continuous curves were computed on basis of the calculated second and third order elastic constants. The error bars of the Einstein free-energy calculations are about one sixth the size of the symbols. The two horizontal arrows show the predictions for Δf obtained by neglecting the third-order elastic constants.

	fcc	hcp
C'_{111}	$-2.0(1)\cdot 10^3$	$-2.1(1)\cdot 10^3$
C'_{112}	$-7.3(9)\cdot 10^1$	$-7.9(9)\cdot 10^1$
C'_{122}	$-3.2(9)\cdot 10^2$	$-4.2(8)\cdot 10^2$
C'_{222}	$-1.71(8)\cdot 10^3$	$-1.71(8)\cdot 10^3$

Table 4.3: Values for the computed third-order elastic constants at melting ($\phi = 0.54329$). These numbers were obtained for fcc and hcp systems containing 13292 particles.

To lowest order in ξ, $\Delta F/V = (-2T_{xx} + C_{11} - C_{12})\xi^2$, for this deformation. As the figure shows, the differences in elastic constants C'_{11} and C'_{12}, for fcc and hcp, are so large that a deformation of 1.2% is enough to make hcp more stable than fcc. The free energy increase of the fcc phase due to a deformation of 2% is $\Delta f_{fcc} = 1.93(1)\cdot 10^{-2}$, while the hcp free-energy increase is only $\Delta f_{hcp} = 1.66(1)\cdot 10^{-2}$. Fig. 4.3 also shows the effect of the third-order elastic constants. To within the statistical accuracy of our simulations, the relevant third-order elastic constants (see table 4.3), were found to be the same for fcc and hcp. Hence, they do not affect the free energy difference between the two lattices.

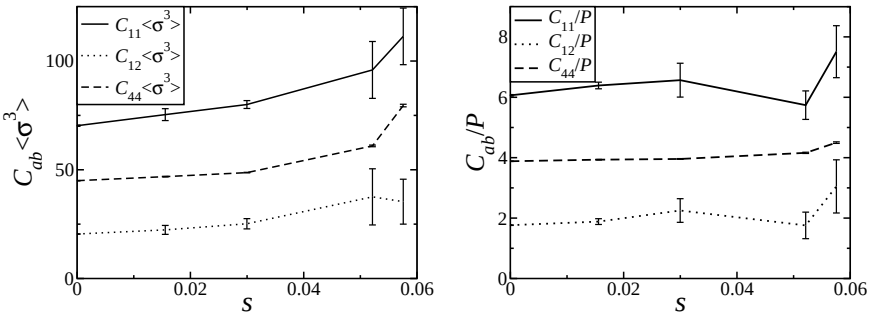

Figure 4.4: Left: the normalized fcc elastic constants $C_{11}\langle\sigma^3\rangle$, $C_{12}\langle\sigma^3\rangle$ and $C_{44}\langle\sigma^3\rangle$ as a function of polydispersity s at the melting curve. Right: 'reduced inverse compressibility' C_{ab}/P as a function of polydispersity.

4.3 Polydispersity

In experiments on hard-sphere colloidal crystals, one has to live with the fact that there is always a certain amount of size dispersity. In experiments on colloidal crystals, the degree of polydispersity (the width of the particle size distribution) of the fluid is typically between 3% and 5%;[27,28,29,30] the polydispersity in the crystal is slightly, lower due to fractionation.[23,24]

In order to estimate the influence of polydispersity on the elastic constants of the hard-sphere crystal, the semigrand-canonical ensemble was used:[69] in this ensemble, polydisperse systems can be conveniently sampled;[23] it allows for quick relaxation through Monte Carlo moves which alter the diameter of particles (for details, see Chapters 6 and 7), obviating the need for diffusion to get a particle-size equilibrated configuration of particles.

The incorporation of the particle sizes in the partition sum has, however, consequences for the derivatives of the semigrand-canonical free energy; they become derivatives not only of the particle position part of the partition sum, but also of the particle diameter part. So, to be able to connect to experimentally obtained elastic constants, we distinguish between 'quenched' and 'annealed' elastic constants: the annealed elastic constants are the full second derivative of the free energy with respect to strain as specified by Eq. 4.1. The quenched elastic constants, however, are specified by the stress-strain relationship (Eq. 2.28 on page 13) of the polydisperse system where the particle diameters are 'frozen in' when the strain is applied.

The quenched elastic constants correspond most closely to what one gets in an experimental situation where particles are fixed to their lattice sites, while, using the semigrand-canonical ensemble simulations one would normally obtain the annealed elastic constants. To be able to obtain the quenched elastic constants, a hybrid MC (Monte Carlo) – MD (Molecular Dynamics) algorithm was used that does not allow particle size relaxation of the deformed system.

This MC–MD algorithm does a normal semigrand-canonical Monte Carlo sampling of an undeformed polydisperse hard sphere crystal and, at regular intervals,

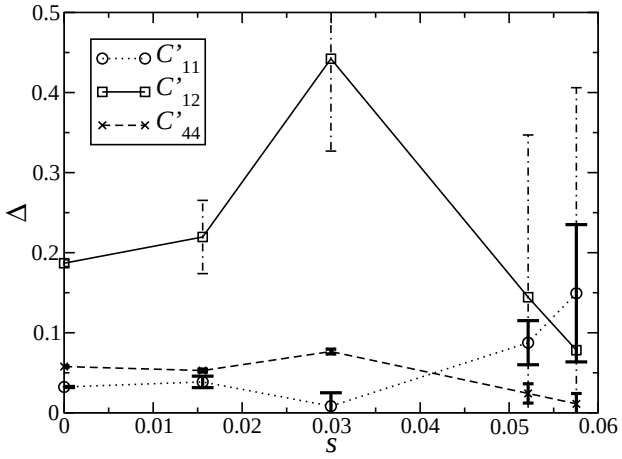

Figure 4.5: Relative difference in fcc and hcp elastic constants $\Delta \equiv |C'^{\mathrm{fcc}}_{ab} - C'^{\mathrm{hcp}}_{ab}|/C'^{\mathrm{fcc}}_{ab}$ as a function of polydispersity at melting.

performs a molecular dynamics simulation in a deformed box, using the particle size distribution and particle coordinates from the MC simulation (Each MD simulation is quickly equilibrated to properly achieve a Maxwell velocity distribution). The algorithm effectively calculates the elastic constants of many realizations of a polydisperse hard-sphere crystal in a normal canonical ensemble.

The results of such simulations applied to the fcc crystal at specific polydispersities along the melting curve, for the normal fcc elastic constants C_{11}, C_{12} and C_{44} (normalized to mean particle size), is shown in Fig. 4.4. The polydispersity s is defined as

$$s \equiv \sqrt{\langle\sigma^2\rangle/\langle\sigma\rangle^2 - 1} \tag{4.5}$$

The elastic constants stay relatively constant, especially when shown relative to the pressure as a reduced inverse compressibility.

The relative difference between a few elastic constants as a function of polydispersity is shown in Fig 4.5, similarly to Fig 4.2. It is clear that the errors in the calculations are much larger due to the added complexity of the MC–MD algorithm. It is, however, clear that — save for the higher polydispersities where the errors are too large to conclude anything — the polydispersity does not seem to affect the relative differences in fcc and hcp elastic constants substantially.

To address the question of the thermodynamic stability of fcc over hcp as a function of polydispersity, thermodynamic integration was used from zero polydispersity to the terminal polydispersity of 5.8% (in the semigrand canonical ensemble) along the melting curve. These showed up to a numerical precision of $10^{-5}k_BT$ per particle, no change in the relative free energies per particle over the entire range of polydispersity.

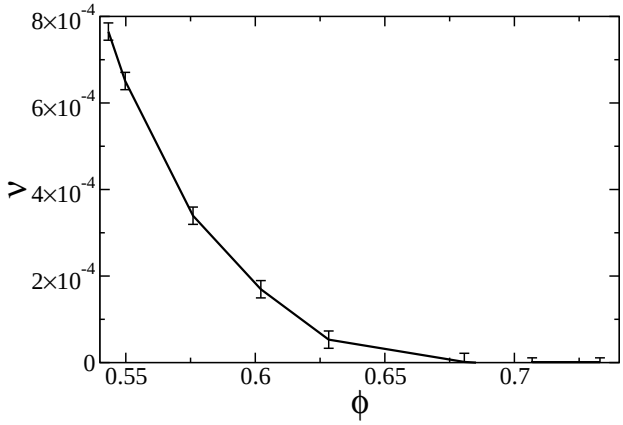

Figure 4.6: Equilibrium anisotropy ($\nu \equiv 1 - \frac{c}{a}/\sqrt{\frac{8}{3}}$) for the hcp hard sphere crystal as a function of packing fraction.

4.4 Lattice Anisotropy

For the undeformed fcc system, all three diagonal components of the pressure tensor are equal. However, this does not hold for a hcp system at the same c/a-ratio (i.e. for the same spacing between the close packed [111]-planes). If we fix the c/a ratio at the fcc value ($\sqrt{8/3}$) then the stresses exhibit a slight anisotropy. For the 13292 particle system T_{xx} and T_{yy} are equal (as they should be): $T_{xx} = -11.587(1)$, $T_{yy} = -11.588(1)$. However, T_{zz} is significantly different: $T_{zz} = -11.537(1)$. From equation 4.1, we can derive what change in the c/a ratio is needed to make the pressure isotropic. We find that, at melting, isotropy is restored for a c/a ratio of $\sqrt{8/3}(1 - 7.5(2) \cdot 10^{-4})$. At higher densities, this value approaches the close-packing value $c/a = \sqrt{8/3}$, as can be seen in Fig. 4.6. Stillinger and Salsburg[68] used the cell-cluster method to estimate the difference of the fcc and hcp c/a ratios. Our simulations show that, close to melting, the effect is one order of magnitude larger than predicted. Some hcp elastic constants reported in tables 4.1 and 4.2 were computed at the c/a ratios where the stress tensors were isotropic. The free energy difference between the equilibrium hcp and fcc crystals is only slightly changed by this relaxation of the hcp c/a ratio: it becomes $1.050(5) \cdot 10^{-3} k_B T$ per particle for $N = 13292$ at melting.

As can be seen from the results for $\phi = 0.543$ — where the c/a ratio differs most from fcc — the effect of relaxing c/a to its equilibrium value, is barely significant. For this reason, most hcp elastic constants in tables 4.1 and 4.2, were computed for $c/a = \sqrt{8/3}$. The table also shows that the elastic constants depend somewhat on system size, but the effect is too small to change the qualitative picture.

In colloidal-epitaxy experiments,[33] the best hcp crystals were obtained when the patterned template was stretched by 2.6% with respect to the expected lattice spacing at the observed experimental packing fraction ($\phi = 0.68$). The templates

used matched a 'diagonal' cut through the *xy* plane of Fig. 4.1. Together with the stress produced by gravity (resulting in a strain perpendicular to the template plane of -2.8%), this strain is comparable to the strain of Eq. 4.4 and would result in a free energy difference of about $3 \cdot 10^{-2} k_B T$ per particle *in favor* of hcp. The present simulation results may help experimentalists in designing optimal templates to grow selectively colloidal hcp or fcc crystals.

4.5 Conclusion

In this chapter we have shown that some elastic constants of the hard sphere fcc and hcp crystals, when expressed in comparable coordinate systems, differ significantly (up to about 20% for C'_{12}). This difference seems not sensitive to either density or polydispersity. This difference can be used to reverse the relative stability of fcc over hcp by applying moderate strain (about 1.5%) in the correct direction.

In addition, the equilibrium lattice spacing of the hard sphere hcp crystal is slightly different than the equivalent spacing in the fcc crystal. The difference in c/a ratio is small ($7.5 \cdot 10^{-4}$) but significant and very slightly affects the relative free energy. This free energy difference is not affected by increasing polydispersity.

5 Point Defects in Hard Sphere Crystals

Any crystal in equilibrium will contain defects, such as vacancies, interstitials and dislocations. Of these, the point defects are the most common. Some thirty years ago, Bennett and Alder[39] estimated the equilibrium concentration of vacancies in a hard-sphere crystal and found that, close to melting, this concentration could be quite high (typically, one vacancy per 4000 lattice sites). At present, the question of the concentration (and transport) of point defects in (colloidal) hard-sphere crystals takes on a renewed — and now quite practical — significance. Apart from the theoretical interest in hard sphere crystals as a model system, crystals from colloidal particles, having lattice sizes comparable to the wavelength of light, are being prepared and studied because of their potentially interesting photonic properties. Clearly the presence of even a small number of defects can have a pronounced effect on the nature of photonic states in such materials. Moreover, as the accuracy of free energy calculations increases, it is no longer permissible to ignore the contribution of vacancies to the total free energy. The aim of the present chapter is to review briefly the statistical mechanical description of a crystal with point defects. This problem is not completely trivial, as the concept of a vacancy or interstitial is inextricably linked to that of lattice sites. And lattice sites loose their meaning in a disordered state. So, we should first address the question: when is it permissible to count states with a different number of lattice sites as distinct? The answer is, of course, that this is only true if these different states can be assigned to distinct volumes in phase space. This is possible if we impose that every particle in a crystal is confined to its Wigner-Seitz cell. In three dimensional crystals, this constraint on the positions of all particles has little effect on the free energy (in contrast, in a *liquid* it is not at all permissible). In a two-dimensional crystal, the constraint is more problematic, at least in the thermodynamic limit. However, for large but finite two-dimensional systems, the single-occupancy cell constraint is also quite reasonable. Below, we describe two alternative (but equivalent) routes to arrive at the free energy of a crystal with vacancies. In one case, we use the Grand-Canonical ensemble. This would seems to be the most obvious ensemble to use when describing a system with a fluctuating number of particles. Yet, the analysis is complicated by the fact that not only the number of particles, but also the number of lattice sites, may fluctuate. In the second analysis, we consider an isothermal-isobaric system. The latter approach is simpler and is, apart from a minor correction, equivalent to the one followed by Bennett and Alder.[39] We then describe our numerical approach

to compute the concentration of interstitials in a hard-sphere crystal. We compare our numerical results with a simple theoretical estimate.

5.1 Free Energy of Vacancies

5.1.1 The Grand-Canonical Route

When considering the statistical mechanics of a crystal with vacancies, it is convenient to consider first a system with a fixed number of lattice sites, M, contained in a volume V. If this crystal is in contact with a particle-reservoir at chemical potential μ, then the number of vacancies in the crystal may fluctuate. In principle, the crystal could also contain interstitials but, for the time being, we shall ignore this possibility. It is then easy to write down the expression for the grand potential of the crystal Ξ':

$$\Xi'_M = \sum_{n=0}^{M} \exp\Big[(M-n)\beta\mu\Big] Q_{M-n}(V,T) \tag{5.1}$$

where $\beta \equiv 1/k_B T$. Note that this is not the true grand potential, because we should also allow for fluctuations in the number of lattice sites. We denote the free energy of a crystal with *no* vacancies by $F^{(0)} = -k_B T \ln Q_M$. In practice, the equilibrium concentration of vacancies in a crystal is very low. We shall therefore make the approximation that vacancies do not interact. This assumption is not as reasonable as it seems, as the interaction of vacancies through the stress field is quite long-ranged. The assumption that vacancies are ideal makes it easier to compute the canonical partition function of a crystal with n vacancies:

$$Q_{M-n}(V,T) \approx \frac{M!}{n!(M-n)!} Q^{(n)}(V,T) = \frac{M!}{n!(M-n)!} \exp(-\beta F^{(n)}) \tag{5.2}$$

where we have used the notation $F^{(n)}$ to denote the free energy of a crystal with n vacancies *at given positions*. As the vacancies are assumed to be non-interacting, it is clear that we can write

$$F^{(n)} = F^{(0)} - n f_1 = M f_0 - n f_1 \tag{5.3}$$

where f_0 is the free energy per particle in the defect-free crystal and -f_1 is the change in free energy of a crystal due to the creation of a single vacancy at a specific lattice point*. Combining Eqs. 5.1, 5.2 and 5.3, we obtain

$$\begin{aligned} \Xi'_M &= \sum_{n=0}^{M} \frac{M!}{n!(M-n)!} \exp\Big[(M-n)\beta\mu\Big] \exp\Big[-\beta(M f_0 - n f_1)\Big] \\ &\equiv Q_M \exp(M\beta\mu)\Big[1+\exp\Big(-\beta[\mu - f_1]\Big)\Big]^M \end{aligned} \tag{5.4}$$

*The choice of the minus sign in the definition will later turn out to be convenient.

Usually, $\exp[-\beta(\mu - f_1)]$ is much less than unity. This allows us to write:

$$\Xi'_M = Q_M \exp(M\beta\mu) \exp\left[M \exp\Big(-\beta[\mu - f_1]\Big)\right] \tag{5.5}$$

Using

$$\langle M - n \rangle = \frac{\partial \ln \Xi'}{\partial \beta\mu}$$

the average number of vacancies follows as

$$\langle n \rangle = M \exp\Big[-\beta(\mu - f_1)\Big] \tag{5.6}$$

Now, we should take into account the fact that, actually, the number of lattice sites itself is not fixed but will adjust to the number of vacancies. The total grand partition function is therefore a sum over all states with different number of lattice sites $M' = M + \Delta M$. In practice, $\Delta M \ll M$. We can then write

$$\Xi = \sum_{\Delta M=-\infty}^{\infty} \Xi'_{M+\Delta M}$$

Note that Ξ' depends on both $M + \Delta M$ and μ. We now choose the reference number of lattice sites such that in that particular case μ is equal to the chemical potential of the perfect lattice. That is:

$$F^{(0)} + P^{(0)}V = M\mu$$

We also introduce a rather strange quantity, namely the 'grand canonical' partition function of a perfect lattice with a fixed number of particles (M) : $\Xi_M^{(0)} \equiv Q_M \exp(M\beta\mu)$. Of course, $\Xi_M^{(0)}$ is *not* a true grand-canonical partition function, as the number of particles in this system is fixed. The Grand Canonical partition function then becomes:

$$\begin{aligned} \Xi &= \sum_{\Delta M=-\infty}^{\infty} \exp\Big[-\beta F^{(0)}(M + \Delta M)\Big] \\ &\times \exp\Big[(M + \Delta M)\beta\mu\Big] \exp\left[(M + \Delta M) \exp\Big(-\beta[\mu - f_1]\Big)\right] \end{aligned} \tag{5.7}$$

We assume (as usual) that, in the thermodynamic limit, Ξ is dominated by the largest term in the sum. Hence, we have to determine the point where the derivative of Ξ with respect to M vanishes. To this end, we perform a Taylor expansion of the exponent in Eq. 5.7 in powers of ΔM. Note that for a perfect — defect free — lattice

$$\frac{\partial F^{(0)}}{\partial M} = \frac{\partial F^{(0)}}{\partial N} = \mu \tag{5.8}$$

and

$$\frac{\partial^2 F^{(0)}}{\partial M^2} = \frac{\partial \mu}{\partial N} = \frac{1}{N}\frac{\partial P}{\partial \rho} \tag{5.9}$$

Moreover,

$$f_1(M+\Delta M) = f_1(M) + \frac{1}{V}\frac{\partial f_1}{\partial \rho}\Delta M + \mathcal{O}(\Delta M^2) \tag{5.10}$$

By combining Eq. 5.8–5.10 we obtain

$$\begin{aligned}\exp\Big[-\beta(\mu - f_1[M+\Delta M])\Big] &= \exp\Big\{-\beta[\mu - f_1(M)]\Big\} \\ &\quad\times\Big[1+\frac{\beta}{V}\frac{\partial f_1}{\partial \rho}\Delta M + \mathcal{O}(\Delta M^2)\Big]\end{aligned} \tag{5.11}$$

Note that $f_1 = F^{(0)} - F^{(1)}$. Hence,

$$\frac{\beta}{V}\frac{\partial f_1}{\partial \rho} = \frac{\beta}{V}\frac{\partial f_1}{\partial V}\frac{\partial V}{\partial \rho} = \beta\frac{V}{N}\left(P^{(0)} - P^{(1)}\right) \equiv \beta\Delta P^{0,1}/\rho \tag{5.12}$$

where $\Delta P^{0,1}$ is the difference in the pressure of two crystals with M lattice sites, one with zero vacancies and the other with one vacancy (both in a fixed volume V and a temperature T). As a consequence,

$$\begin{aligned}(M+\Delta M)\quad &\exp\Big[-\beta(\mu - f_1[M+\Delta M])\Big] \\ &\approx M\exp\Big\{-\beta[\mu - f_1(M)]\Big\}\Big\{1+\frac{\Delta M}{M} + (\beta\Delta P^{0,1}/\rho)\Delta M\Big\}\end{aligned} \tag{5.13}$$

Inserting the Taylor expansion in the expression for Ξ, we obtain

$$\begin{aligned}\Xi = \quad &\exp\Big[-\beta F^{(0)}(M) + M\beta\mu\Big]\Sigma_{\Delta M}\exp\Big\{M\exp\Big[-\beta(\mu - f_1(M))\Big] \\ &\times\Big[1+\tfrac{\Delta M}{M} + (\beta\Delta P^{0,1}/\rho)\Delta M\Big] - \tfrac{\beta}{2}\tfrac{1}{M}\tfrac{\partial P}{\partial \rho}(\Delta M)^2\Big\}\end{aligned} \tag{5.14}$$

It may seem inconsistent that we expand to second order in ΔM in the last term of Eq. 5.14 but only to first order in the preceding terms. However, as we show below, we actually expand — consistently — to second order in the vacancy concentration.

We define the fractional change in the number of lattice sites, y, as

$$y \equiv \frac{\Delta M}{M} \tag{5.15}$$

Similarly, we define the vacancy concentration x as

$$x = \frac{\langle n\rangle}{M} = \exp\Big[-\beta(\mu - f_1)\Big] \tag{5.16}$$

Finding the maximum in the exponent is then equivalent to maximizing

$$-\frac{\beta M}{2}\left(\frac{\partial P}{\partial \rho}\right)y^2 + Mx(0)\Big[1 + y(1+\beta V\Delta P^{0,1})\Big] \tag{5.17}$$

where $x(0)$ is the value of x for $\Delta M = 0$ and ρ_s is the density of the ideal reference lattice. The maximum value is at

$$y = x(0)\frac{(1+\beta V \Delta P^{0,1})}{\beta\left(\frac{\partial P}{\partial \rho}\right)} \tag{5.18}$$

and the maximum of the grand canonical potential is

$$\Xi \approx \exp(-\beta F^{(0)}(M) + M\beta\mu)\exp\left(Mx(0) + \frac{M}{2}\frac{x^2(0)\left(1+\beta V\Delta P^{0,1}\right)^2}{\beta\left(\frac{\partial P}{\partial \rho}\right)}\right) \tag{5.19}$$

Hence, the presence of vacancies increases the grand potential (as it should) *and it changes (increases) the number of lattice sites*. However, ignoring terms of order $\mathcal{O}(x^2(0))$, the vacancy concentration is still given by Eq. 5.6.

The next question is: how do vacancies affect the melting curve. Now our definition of the reference system (i.e. the perfect lattice with the same μ) turns out to be convenient. Note that the Grand Canonical partition function is related to the pressure by

$$\beta PV = \ln\Xi = \beta P^{(0)}V + Mx(0) + \mathcal{O}(x(0)^2) \tag{5.20}$$

Ignoring terms quadratic in the vacancy concentration, we find that the effect of allowing for vacancies is to increase the pressure of the solid by an amount

$$\Delta\mathbf{P} \approx x(0)\rho_s k_B T \tag{5.21}$$

Let us assume that the liquid was in equilibrium with the perfect crystal at pressure P and chemical potential μ. Then it is easy to verify that the shift in the coexistence pressure due to the presence of vacancies is

$$\delta P_{coex} = \frac{-x(0)k_B T}{\rho_l^{-1} - \rho_s^{-1}} \tag{5.22}$$

and the corresponding shift in the chemical potential at coexistence is

$$\delta\mu_{coex} = \frac{\delta P_{coex}}{\rho_l} \tag{5.23}$$

Direct calculations of the vacancy concentration in a hard-sphere crystal at melting[39] indicate that $x(0) \approx 2.6\cdot 10^{-4}$. Hence, the increase in the coexistence pressure due to vacancies is $\delta P_{coex} \approx -2.57\cdot 10^{-3}\ k_B T/\sigma^3$ (where σ is the particle diameter). The corresponding shift in the chemical potential at coexistence is $\delta\mu_{coex} = -2.74\cdot 10^{-3} k_B T$ Note that this shift is very significant when compared to the accuracy of absolute free-energy calculations of the crystalline solid.[42]

5.1.2 The NPT Route

Bennett and Alder[39] work with the Gibbs free energy rather than the Helmholtz free energy. Their expression for the vacancy concentration is based on the analysis of the effect of vacancies on the Gibbs free energy of a system of N particles at constant pressure and temperature. First, we define g^{vac}, the variation in the Gibbs free energy of a crystal of M particles due to the introduction of a single vacancy *at a given lattice position*

$$\begin{aligned} g^{vac} &\equiv G_{M+1,1}(N,P,T) - G_{M,0}(N,P,T) \\ &= F_{M+1,1}(V_{M+1,1}) - F_{M,0}(V_{M,0}) + P(V_{M+1,1} - V_{M,0}) \end{aligned} \tag{5.24}$$

where the first subscript refers to the number of lattice sites in the system, and the second subscript to the number of vacancies. In this equation we distinguish M, the original number of lattice sites, and N, the number of particles, even though in the present case $N = M$. Let us write f_1 (Eq. 5.37) as

$$-f_1 \equiv F_{M+1,1}(V_{M+1,0}) - F_{M+1,0}(V_{M+1,0})$$

Hence,

$$\begin{aligned} g^{vac} &= F_{M+1,1}(V_{M+1,1}) - F_{M+1,1}(V_{M+1,0}) + \\ &\quad F_{M+1,1}(V_{M+1,0}) - F_{M+1,0}(V_{M+1,0}) + \\ &\quad F_{M+1,0}(V_{M+1,0}) - F_{M,0}(V_{M,0}) + \\ &\quad P(V_{M+1,1} - V_{M,0}) \end{aligned} \tag{5.25}$$

The next step is to introduce a hypothetical defect free crystal with M lattice sites, at the same pressure as the system with $M+1$ lattice sites. The volume of this system is $V_{M,0} = \{M/(M+1)\}V_{M+1,0}$.Similarly, the free energy of this hypothetical system is $F_{M,0} = \{M/(M+1)\}F_{M+1,0}$. Note also that

$$F_{M+1,1}(V_{M+1,1}) - F_{M,0}(V_{M,0}) = -P\Delta v - f_1 + f_0 \tag{5.26}$$

where $\Delta v \equiv v^{vac} - v^{part}$ is the difference in volume of a vacancy and a particle, at constant pressure and number of lattice sites. Moreover,

$$P(V_{M+1,1} - V_{M,0}) = P(\Delta v + V/N) \tag{5.27}$$

Hence, the Gibbs free energy difference associated with the formation of a vacancy at a specific lattice site, $G_{M,1} - G_{M-1,0} \equiv g^{vac}$, is then

$$\begin{aligned} g^{vac} &= P(V_{M+1,1} - V_{M,0}) - f_1 + (\Delta v + V/N)P + f_0 \\ &= P(V_{M,1} - V_{M,0} + V_{M,0} - V_{M-1,0}) - f_1 + f_0 \\ &= P(V/N) - f_1 + f_0 \\ &= (P/\rho + f_0) - f_1 \\ &= \mu_0 - f_1 \end{aligned} \tag{5.28}$$

where we have defined $\mu_0 \equiv (P/\rho + f_0)$. Now we have to include the entropic contribution due to the distribution of n vacancies over M lattice sites. This total Gibbs free energy then becomes

$$\begin{aligned} G &= G_0(N) + ng^{vac} + Mk_BT\left(\frac{n}{M}\ln\frac{n}{M} + \left[1-\frac{n}{M}\right]\ln\left[1-\frac{n}{M}\right]\right) \quad (5.29)\\ &\approx G_0(N) + ng^{vac} + nk_BT\ln\frac{n}{M} - nk_BT \quad (5.30)\end{aligned}$$

If we minimize the Gibbs free energy with respect to n, we find

$$\langle n\rangle \approx M\exp(-\beta g^{vac})$$

where we have ignored a small correction due to the variation of $\ln M$ with n. If we insert this value in the expression for the total Gibbs free energy, we find:

$$G = G_0(N) + \langle n\rangle g^{vac} - \langle n\rangle g^{vac} - \langle n\rangle k_BT = G_0 - \langle n\rangle k_BT$$

The total number of particles is $M - \langle n\rangle$. Hence the Gibbs free energy *per particle* is

$$\begin{aligned}\mu &= \frac{G_0 - \langle n\rangle k_BT}{N} = \mu_0 - \frac{\langle n\rangle k_BT}{N}\\ &\approx \mu_0 - x_v k_BT \quad (5.31)\end{aligned}$$

Thus the change in chemical potential of the solid is

$$\Delta\mu = -x_v k_BT \quad (5.32)$$

from which it follows that the change in *pressure* of the solid at fixed chemical potential is equal to

$$\Delta P = x_v\rho_s k_BT \quad (5.33)$$

This is equivalent to Eq. 5.21 above. Hence the Bennett-Alder scheme is equivalent to the 'grand-canonical' scheme [†]

It should be pointed out that the variation in volume due to the replacement of a particle by a vacancy can be computed either directly, in a constant-pressure simulation, or indirectly by measuring the change in pressure in a constant volume simulation. The two methods are related through the thermodynamic relation

$$\left(\frac{\partial V}{\partial P}\right)_{N,T}\left(\frac{\partial P}{\partial N}\right)_{V,T}\left(\frac{\partial N}{\partial V}\right)_{P,T} = -1 \quad (5.34)$$

Noting that the number of vacancies is $n = M - N$, we can see that the change in pressure with the number of vacancies for a fixed number of lattice sites, is

$$-\left(\frac{\partial P}{\partial N}\right)_{V,T} = \left(\frac{\partial P}{\partial V}\right)_{N,T}\left(\frac{\partial V}{\partial N}\right)_{P,T} \quad (5.35)$$

[†] In Ref. 39, a slightly different expression is found, but this is due to a small error in the derivation in that paper.

In particular, the pressure change due to one vacancy (i.e. $\Delta P^{0,1}$, defined in Eq. 5.12) is

$$\Delta P^{0,1} = P_{M.0} - P_{M,1} = \Delta v \left(\frac{\partial P}{\partial V} \right)_{N,T} \tag{5.36}$$

5.2 Computational Scheme

5.2.1 Vacancies

Numerically, it is straightforward to compute the equilibrium vacancy concentration. As before, the central quantity that needs to be computed is $-f_1$, the change in free energy of a crystal due to the creation of a single vacancy at a specific lattice point. In fact, it is more convenient to consider $+f_1$, the change in free energy due to the removal of a vacancy at a specific lattice point. This quantity can be computed in several ways. For instance, we could use a particle-insertion method. We start with a crystal containing one single vacancy and attempt a trial insertion in the Wigner-Seitz cell surrounding that vacancy. Then f_1 is given by

$$f_1 = -k_B T \ln \left(\frac{V_{WS} < \exp(-\beta \Delta U >}{\Lambda^d} \right) \tag{5.37}$$

where V_{WS} is the volume of the Wigner-Seitz cell, and ΔU is the change in potential energy associated with the insertion of a trial particle. For hard particles

$$f_1 = -k_B T \ln \left(\frac{V_{WS} P_{acc}(V_{WS})}{\Lambda^d} \right) \tag{5.38}$$

where $P_{acc}(V_{WS})$ is the probability that the trial insertion in the Wigner-Seitz cell will be accepted. As most of the Wigner-Seitz cell is not accessible, it is more efficient to attempt insertion in a sub-volume (typically of the order of the cell-volume in a lattice-gas model of the solid). However, then we also should consider the reverse move — the removal of a particle from a sub-volume v of the Wigner-Seitz cell, in a crystal without vacancies. The only thing we need to compute in this case is $P_{rem}(v)$, the probability that a particle happens to be inside this volume. The expression for f_1 is then

$$f_1 = -k_B T \ln \left(\frac{v P_{acc}(v)}{P_{rem}(v) \Lambda^d} \right) \tag{5.39}$$

Of course, in the final expression for the vacancy concentration, the factor Λ^d drops out (as it should), because it is cancelled by the same term in the ideal part of the chemical potential.

5.2.2 Interstitials

As in the case of vacancies, the calculation of interstitials centers around the calculation of g_I, the free energy associated with introducing an interstitial into the

system (in the NPT ensemble). g_I can be expressed as a sum of two parts: the free energy of introducing a point particle into the system ($g^{ins} = -k_B T \ln < 1 - \eta >$, where η is the packing fraction), and the free energy of growing that particle to the same diameter ($\sigma_0 \equiv 1$) as the other particles (g^{grow}).

For the calculation of g^{grow}, we simulate an extended system consisting of a lattice of N particles with diameter $\sigma_0 = 1$ on (or near) lattice sites and one extra (interstitial) particle that has a diameter σ_I that can vary freely. We interpret σ_I as an additional coordinate and, in this sense, the system that we are considering is an extended system. The partition sum for the extended system is

$$Q(N+1,P,T) = \int_0^1 d\sigma' \, Q(N+1,P,T,\sigma') \tag{5.40}$$

where $Q(N+1,P,T,\sigma')$ is the partition function for the isothermal-isobaric system with one interstitial particle with radius σ'. The probability of finding the interstitial particle with a specific radius $\sigma' = \sigma_I$ is

$$\begin{aligned} P(\sigma_I|N+1,P,T) &= \frac{\int_0^1 d\sigma' \, Q(N+1,P,T,\sigma')\delta(\sigma_I - \sigma')}{Q(N,P,T)} \\ &= \frac{Q(N+1,P,T,\sigma_I)}{Q(N+1,P,T)} \end{aligned} \tag{5.41}$$

and the Gibbs free energy $G(N+1,P,T,\sigma_I)$ of a system with an interstitial with diameter σ_I is equal to

$$G(N+1,P,T,\sigma_I) = -k_B T \ln Q(N+1,P,T,\sigma_I) \tag{5.42}$$

Thus, the free energy difference between a system with a pintails interstitial ($\sigma_I = 0$) and a full-grown interstitial ($\sigma_I = 1$) is

$$\begin{aligned} g^{grow} &= G(N+1,P,T,1) - G(N+1,P,T,0) \\ &= -k_B T \ln \frac{Q(N+1,P,T,1)}{Q(N+1,P,T,0)} \\ &= k_B T \ln \frac{P(0|N+1,P,T)}{P(1|N+1,P,T)} \end{aligned} \tag{5.43}$$

It is obvious that $P(\sigma|N+1,P,T)$ can be very small for large values of σ_I. In order to get an accurate histogram for $P(\sigma_I|N+1,P,T)$, we have to use a biased sampling scheme. We employ the method of umbrella-sampling/multicanonical sampling,[70,43] where we associate a weight $\xi(\sigma)$ with σ, which we use while sampling over σ:

$$P(\sigma|N+1,P,T,\{\xi\}) \propto P(\sigma|N+1,P,T)e^{\xi(\sigma)}$$

If we sample over this distribution, we get a histogram $P(\{\sigma\}|N+1,P,T,\{\xi\})$, for which we can get the desired histogram $P(\{\sigma\}|N+1,P,T)$ by refolding the bias:

$$P(\sigma|N+1,P,T) \propto P(\sigma|N+1,P,T,\{\xi\})e^{-\xi(\sigma)}$$

The weights $\xi(\sigma)$ are obtained by iteratively running the system and calculating (for the run $i+1$, from the results of run i)

$$\xi_{i+1}(\sigma) = \xi_i(\sigma) - \ln P(\sigma|N,P,T,\{\xi_i(\sigma)\}) + C$$

where C is an arbitrary constant.[43] This will make the histogram $P(\{\sigma_0\}|N+1,P,T,\{\xi\})$ converge to a flat distribution over the accessible range.

5.2.3 Interstitial Type Discrimination

The fcc crystal has two types of possible places, or 'holes' in which interstitials can reside: one of octahedral shape and one of tetrahedral shape. There are four octahedral holes and eight tetrahedral holes in one fcc unit cell. To measure the relative concentrations of interstitials in these two types of holes, it turns out it is not possible to try to prepare the system in one hole and calculate g^{grow}, because during the course of a simulation the interstitial makes many hops.

In order to measure the relative occupation probability of the different holes, the interstitial has to be traced. This is done by the following scheme: at the start of the simulation, every particle i, except the original interstitial, is assigned to a lattice position $\mathbf{R}_i$. At fixed sampling intervals, the squared distance between the original interstitial and the nearest lattice sites ($\delta^2_{int,i} = (\mathbf{r}_{int} - \mathbf{R}_i)^2$) is compared with $\delta_i^2 = (\mathbf{r}_i - \mathbf{R}_i)^2$. If $\delta^2_{int,i} < \delta_i^2$, the interstitial and particle i exchange identity (i.e. the interstitial acquires a lattice position $\mathbf{R}_i$ and particle i becomes the interstitial). Once we have identified the interstitial, it is straightforward to assign it to a tetrahedral or octahedral hole.

5.3 Simulation Results

The free energy calculations were performed with $256+1$ particle systems ($4\times4\times4$ cubic fcc unit cells) at four different pressures. Different parts of the histogram $P(\{\sigma\}|N,P,T,\{\eta\})$ were calculated in parallel, and subsequently combined. The calculation of the weights took about 20 iterations of $2\cdot10^4$ MC sweeps per CPU on 5 CPU's. Once the weights were known for one pressure, they could be used as starting points for the other pressures, accelerating the weight calculation considerably. Final calculations were done with approximately 20 iterations of $4\cdot10^5$ sweeps each (again on 5 CPU's). The final $P(\sigma|N,P,T)$ histograms for all four pressures are plotted in Fig. 5.1.

For the calculation of μ at the different pressures, the results for the free energy of the perfect crystal[42] were used together with Hall's[71] equation of state. The results are summarized in Fig. 5.2 and table 5.1. For one pressure ($P = 11.7$, the coexistence pressure), we calculated g_I for a larger system ($N = 8\times8\times8+1 = 2048+1$) to check for finite-size effects; as can be seen from the results, these are negligible. Using the interstitial type discrimination algorithm described above, it was found that the (bigger) octahedral holes are far more likely to contain the interstitial than the tetrahedral holes (see table .5.1).

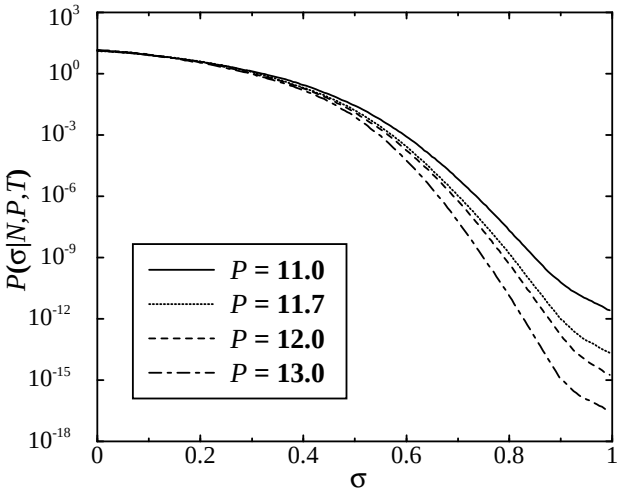

Figure 5.1: The normalized probability $P(\sigma|N,P,T)$ of finding an interstitial with radius $\sigma/2$ for hard-sphere crystals at (reduced) pressures 11, 11.7, 12 and 13.

5.3.1 Interstitial Diffusion

When an interstitial is tracked, as described in section 5.2.3, an interesting effect can be seen. As is shown in Fig. 5.3, the interstitial makes discrete 'hops'. These hops are from one octahedral hole to the other; the interstitial takes the place of a lattice particle, which then in turn becomes the interstitial.

This hopping leads to a fast diffusion of the interstitial through the crystal; Fig. 5.4 shows the mean squared distance (relative to the interstitial's original position) as a function of the number of random particle displacements (MC cycles) for a MC simulation with very small (relative to inter-particle separation) particle displacement moves. In this case, the particles will move diffusively. When this short-time self-diffusion is compared to the long time hopping diffusion, they turn out to be nearly equal: for a step size of $l = 0.0008\sigma$, the short-time self-diffusion constant is[72] $D_{\text{self}} = \frac{1}{2d} l^2 \approx 1.07 \times 10^{-7}\sigma^2/\text{step}$, while the long-time hopping diffusion constant is $D_{\text{hop}} = 1.20 \times 10^{-7}\sigma^2/\text{step}$. Because the diffusion is so fast, particle diffusion through interstitials could be a major mechanism for particle diffusion through the crystal, even when interstitial concentrations are low.

5.4 Analytical Estimate of the Free Energy of Interstitials

As octahedral holes are the largest cavities in an fcc crystal, we limit our analysis to these. The number of octahedral holes in an fcc crystal is equal to the number

P	11.0	11.7	11.7	12.0	13.0
N	$256+1$	$256+1$	$2048+1$	$256+1$	$256+1$
η	0.536	0.545	0.545	0.548	0.559
μ	16.5	17.1	17.1	17.4	18.4
g_I/k_BT	29.9(1)	34.5(2)	34.7(2)	36.5(2)	44.1(3)
x_I	$1.5\cdot10^{-6}$	$2.7\cdot10^{-8}$	$2.4\cdot10^{-8}$	$5.6\cdot10^{-9}$	$7.2\cdot10^{-12}$
h_{et}	0.087(6)	0.032(2)		0.079(9)	0.118(8)
C_{44}	41	46	46	48	57
$x_{I,\mathrm{a}}$	$1.1\cdot10^{-6}$	$1.3\cdot10^{-7}$	$1.3\cdot10^{-7}$	$6.8\cdot10^{-8}$	$3.2\cdot10^{-9}$

Table 5.1: Simulation results for the properties of interstitials in hard sphere crystals. The values for the packing fraction η and the chemical potential μ were taken from refs. 42 and 71. g_I is the free energy associated with interstitial formation, x_I is the interstitial concentration from the simulations. h_{et} is the fraction of interstitials found in tetrahedral holes. The values from the analytical estimate of section 5.4 are given as $x_{I,\mathrm{a}}$, using values for the elastic constants C_{44} from ref. 65

of lattice sites, the derivation of the expression for the concentration of interstitials is almost identical to the one for the vacancy concentration. Let us denote the change in free energy associated with the introduction of an interstitial at a specific octahedral site by f_I. The concentration of interstitials is then

$$x_I = \exp\Big[-\beta(f_I-\mu)\Big] \tag{5.44}$$

In a static lattice, r_0, the radius of such octahedral holes equals $(\sqrt{2}/2-0.5)a$, where a is the nearest-neighbor distance. For a hard-sphere crystal at melting, this radius equals $r_0 = 0.229\ \sigma$. Clearly, in order to fit in an interstitial, the cavity has to be expanded. If we assume that the crystal is elastically isotropic (a fair approximation for a cubic crystal) then the work needed to create a cavity of radius r equals[63]

$$W = 8\pi\mu_L r_0 (r-r_0)^2 \tag{5.45}$$

where μ_L is the shear Lamé coefficient. How large should r be? Clearly, it should be at least 0.5σ, otherwise the interstitial would not fit into the lattice. But, in fact, it should be larger, because the interstitial particle itself requires some free volume v_F. We should therefore minimize the sum of the free energy of a particle in a cavity of radius r and the elastic energy required to create such a cavity. Using $v_F = (4\pi/3)(r-\sigma/2)^3$, the expression for this free energy is[‡]

$$F(r) = -k_BT\ln\Big[(4\pi/3)(r-\sigma/2)^3\Big] + 8\pi\mu_L r_0(r-r_0)^2 \tag{5.46}$$

[‡] In what follows, we leave out the factor involving the de Broglie thermal wavelength, as it cancels anyway in the final result.

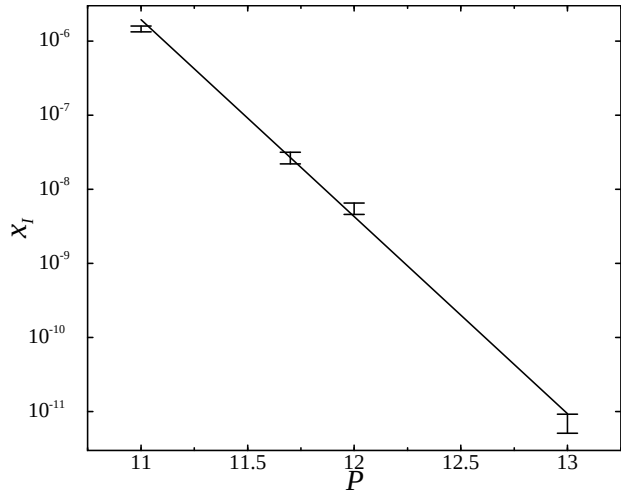

Figure 5.2: x_I as a function of the reduced pressure P. The drawn line corresponds to a fit of the form $x_I = \exp(-6.1P + 54)$

Differentiating Eq. 5.46 with respect to r yields the following equation for the equilibrium radius of the cavity:

$$-\frac{3k_BT(r-\sigma/2)^2}{(r-\sigma/2)^3} + 16\pi\mu_L r_0(r-r_0) = 0 \tag{5.47}$$

This yields the following equation for r

$$r^2 - (\sigma/2 + r_0)r + \frac{\sigma r_0}{2} - \frac{3k_BT}{16\pi\mu_L r_0} = 0$$

and hence

$$r_I = \frac{\sigma/2 + r_0}{2} + \sqrt{\frac{(\sigma/2+r_0)^2}{4} - \frac{\sigma r_0}{2} + \frac{3k_BT}{16\pi\mu_L r_0}} \tag{5.48}$$

Inserting Eq. 5.48 in Eq. 5.46 we obtain the expression for the total free energy of an interstitial at a specific lattice site

$$f_I = -k_BT \ln\left[(4\pi/3)(r_I - \sigma/2)^3\right] + 8\pi\mu_L r_0(r_I - r_0)^2 \tag{5.49}$$

If we use the parameters for a hard-sphere solid at melting ($\mu_L \approx C_{44} = 46$[65]), we find that the predicted concentration of interstitials is approximately $1 \cdot 10^{-7}$. Considering the crudeness of the approximations involved in deriving this result, the agreement with the corresponding numerical estimate ($x_I \approx 3 \cdot 10^{-8}$) is gratifying. However, at higher densities, the agreement becomes worse, possibly because it is no longer justified to assume isotropic, linear, elastic behavior around an interstitial (see table 5.1).

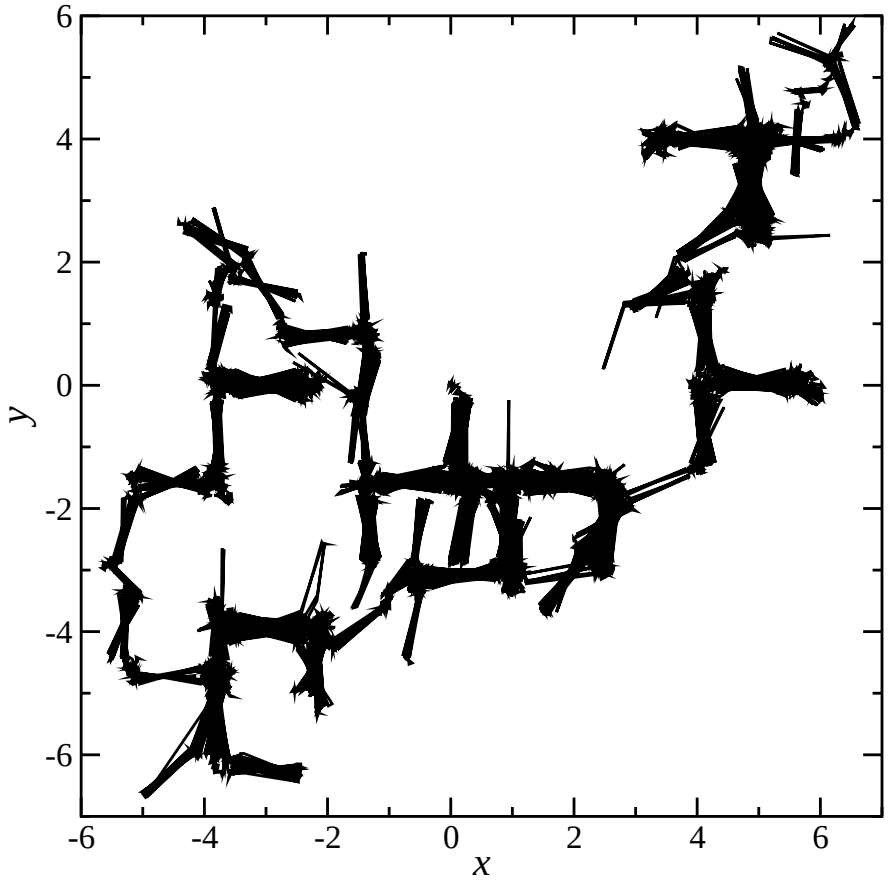

Figure 5.3: Projection of the interstitial position during the simulation onto the *xy*-plane. Note the horizontal and vertical 'hops' that correspond to octahedral holes in the 100-oriented fcc crystal.

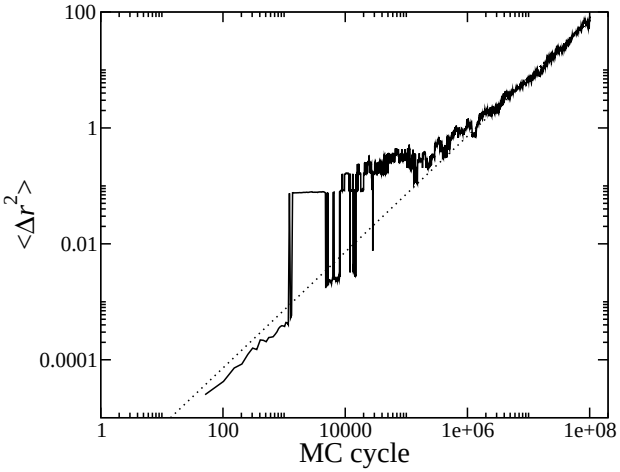

Figure 5.4: Mean interstitial distance from the origin ($\langle \Delta r^2 \rangle$) as a function of MC cycle number for a MC simulation with small particle step size ($l = 0.0008\sigma$). The MC cycle number here corresponds to the number of displacements in a random walk. The dotted line corresponds to the fitted diffusion coefficient. The discrete nature of the interstitial 'hopping' is clearly visible in the intermediate regime of 10^3–10^5 cycles.

In summary, we have shown that the equilibrium concentration of interstitials in hard-sphere crystals is so low that most experiments will not be able to detect them. We find that interstitials are quite mobile. This implies that interstitials that are trapped during crystal growth should be able to diffuse rapidly to the crystal surface. This information is good news for experimentalists trying to grow photonic band-gap materials. On the other hand, colloidal hard sphere crystals will have a high equilibrium concentration of vacancies. With the present accuracy of free-energy calculations, vacancies yield a detectable change in the free energies, but interstitials do not.

6 Polydispersity and Point Defect Concentrations

The experimental study of colloidal crystals is of interest for at least two reasons. First of all, the possibility to design the building blocks of such crystals, allows us to gain insight into the factors that determine the structure and kinetics of formation of crystalline materials. In addition, colloidal crystals are of interest because of their potential application as photonic materials.[15] To a first approximation, one might view colloidal crystals as scale models of atomic crystals. But this analogy is tenuous for several reasons. First of all, the intermolecular forces between colloidal particles may be qualitatively different from those between atoms. Secondly, the dynamics of colloidal matter is intrinsically different from that of atomic materials, due to the presence of a solvent. Finally, unlike atomic materials, colloidal systems are never completely mono-disperse. This polydispersity may have important consequence for the phase behavior and structural properties of the colloidal crystals. In addition, polydispersity can have an effect on the equilibrium concentration of (point) defects in colloidal crystals. As defects may strongly influence the photonic properties of colloidal crystals, a better understanding of the effect of polydispersity on defect concentrations, may also be of practical relevance for the design of photonic crystals.

This chapter describes a numerical study of the effect of polydispersity on the concentration of vacancies and interstitials in hard-sphere colloidal crystals.

6.1 Simulation Methods

6.1.1 Semigrand Canonical Ensemble

To simulate the equilibrium properties of polydisperse hard-sphere crystals, we used the semigrand canonical ensemble method.[69,23] For a system with continuous size polydispersity, the free-energy functional of the semigrand canonical ensemble is given by:

$$\begin{aligned} Y(N,P,T,\{\Delta\mu\}) &= U - TS + PV + N\mu(\sigma_0) - N\int d\sigma \left[\mu(\sigma) - \mu(\sigma_0)\right] p(\sigma) \\ &= N\mu(\sigma_0) \end{aligned} \tag{6.1}$$

where N is the total number of particles in the system, P is the pressure, T is the temperature and the set $\{\Delta\mu\}$ denotes the differences between $\mu(\sigma)$, the chemi-

cal potential of a species with diameter σ, and $\mu(\sigma_0)$, the chemical potential of an (otherwise arbitrary) reference species: $\Delta\mu(\sigma) \equiv \mu(\sigma) - \mu(\sigma_0)$. As we are dealing with hard-core particles, we choose our unit of energy to be equal to $k_B T$. $p(\sigma)$ denotes the probability of finding a particle with diameter σ. The set of thermodynamic fields $\{\Delta\mu\}$ act as control parameters that determine the particle-size distribution. In the present work, we assume a quadratic dependence of $\Delta\mu(\sigma)$ on $\sigma - \sigma_0$:

$$\mu(\sigma) - \mu(\sigma_0) = -(\sigma - \sigma_0)^2/2\nu \tag{6.2}$$

The parameter ν determines the degree of polydispersity. At infinite dilution, the size distribution is directly given by $p(\sigma) = c\exp(-(\sigma - \sigma_0)^2/2\nu)$. At finite concentrations, the size distribution cannot be inferred directly from the functional form of $\Delta\mu(\sigma)$. Both the average particle diameter and the actual polydispersity s (defined through $s^2 \equiv \langle\sigma^2\rangle/\langle\sigma\rangle^2 - 1$) must be determined in the semigrand ensemble simulations. Once the functional form of $\Delta\mu(\sigma)$ has been specified, the semi-grand partition function Ξ is a function of N, P, T, ν and σ_0.

$$\begin{aligned}\Xi(N,P,T,\nu,\sigma_0) = &\int dV \int d\mathbf{r}^N \int d\sigma^N \\ &\exp\left(-\beta\left[PV + U\left(r^N,\sigma^N\right)\right] - \sum_i \frac{(\sigma_i - \sigma_0)^2}{2\nu}\right)\end{aligned} \tag{6.3}$$

The semigrand free energy Y is related to Ξ through $Y = -k_B T \ln \Xi$. To sample the configurations of the semi-grand ensemble, we use Metropolis-style Monte Carlo sampling of all variables that characterize a given configuration of the N-particle system. In addition to the usual trial moves that attempt to change the particle coordinates $\{\mathbf{r}^N\}$ and the system volume V, there are trial moves to change the diameter of a particle. As has been explained by Bolhuis and Kofke, it is computationally more efficient to combine volume-changing moves with particle resizing moves.[23]

To calculate the chemical potential of the reference species, thermodynamic integration was used. As a reference state, we took the monodisperse hard-sphere crystal near coexistence, for which the free energy per particle is accurately known through thermodynamic integration with the Einstein crystal as a reference.[42] In order to compute the change in free energy with P and ν, we make use of the following thermodynamic relations:

$$\begin{aligned}\left(\frac{\partial Y}{\partial P}\right)_{N,T,\nu} &= V \\ \left(\frac{\partial Y}{\partial \nu}\right)_{N,P,T} &= \int d\sigma' p(\sigma') \frac{-(\sigma' - \sigma_0)^2}{2\nu^2}\end{aligned} \tag{6.4}$$

The semigrand free energy of an ideal, non-interacting system of polydisperse particles, is

$$Y_{\text{id}} = -k_B T \ln \int dV \exp(-\beta PV) \int d\mathbf{r}^N \int d\sigma^N \exp\left(-\sum_i \frac{(\sigma_i - \sigma_0)^2}{2\nu}\right)$$

$$= \quad N\mu_{\rm id}(\sigma_0) = G_{\rm id} - \frac{Nk_BT}{2}\ln(2\pi v) \tag{6.5}$$

We can now employ the following scheme to compute $\mu_{\rm ex}(\sigma_0)$ by thermodynamic integration, using as input our knowledge of the excess chemical potential $\mu_{\rm ex,0}$ of a monodisperse hard sphere system at pressure P_0:

$$\begin{aligned}\mu_{\rm ex}(\sigma_0) &= \mu_{\rm ex,0} + \frac{1}{N}\int_{P_0}^{P} dP' \left\langle V - \frac{(N+1)k_BT}{P'} \right\rangle \\ &\quad + \frac{1}{N}\int_0^v dv' \left\langle \frac{-\sum_i(\sigma_i-\sigma_0)^2}{2v'^2} + \frac{N}{2v'} \right\rangle . \end{aligned} \tag{6.6}$$

6.1.2 Interstitial Concentration

The methods that we used to calculate the concentration of point defects are similar to those discussed in Chapter 5. We first consider the free energy Y_{M,n_V,n_I} of a crystalline system containing M lattice sites, n_V vacancies and n_I interstitials. The total number of particles in this system is $N = M + n_I - n_V$. It is convenient to consider interstitials and vacancies separately.

By analogy to the derivation of interstitial concentrations in monodisperse systems of chapter 5, it is straightforward to show that the concentration of interstitials (x_I) is given by $x_I \approx \exp(-\beta y_I)$, where y_I is defined as $y_I = Y_{M,0,1} - Y_{M+1,0,0}$. It is convenient to rewrite y_I as

$$\begin{aligned} y_I &= Y_{M,0,1} - Y_{M+1,0,0} \\ &= Y_{M,0,1} - Y_{M,0,0} + Y_{M,0,0} - Y_{M+1,0,0} \\ &= Y_{M,0,1} - Y_{M,0,0} - \left[\mu_{\rm id}(\sigma_0) + \mu_{\rm ex}(\sigma_0)\right] \\ &= Y_{M,0,1} - \left[Y_{M,0,0} + \mu_{\rm id}(\sigma_0)\right] - \mu_{\rm ex}(\sigma_0) \\ &= y_{\rm add} - \mu_{\rm ex}(\sigma_0) \end{aligned} \tag{6.7}$$

Here $y_{\rm add}$ is the free energy difference between a system with one interstitial and a perfect crystal plus one ideal (non-interacting) particle.

To calculate $y_{\rm add}$, we simulate a crystal with M lattice sites and $M+1$ particles, of which particle j has a scaled hard-core diameter $a\sigma_j$. The diameter scaling parameter a can be varied during the simulation, so that we sample the partition defined by

$$\Xi'_{M,0,1}(M+1,P,T,v) = \int_0^1 da\, \Xi_{M,0,1}(M+1,P,T,v,a) \tag{6.8}$$

where $\Xi_{M,0,1}(M+1,P,T,v,\sigma_0,a)$ is defined as in Eq. 6.3, but with configurational energy $U(\mathbf{r}^M,\sigma^M,a\sigma_j)$. We stress that particle j differs from the other particles only in the overlap criterion, not in the probability distribution that determines diameter sampling: for the overlap criterion, the particle radius of this particle is $a\sigma$,

whereas its weight in the Semigrand chemical potential distribution of Eq. 6.2 is still determined by σ.

During the simulation, we construct a histogram $P(a|M,P,T,\nu)$:

$$P(a|M+1,P,T,\nu) = \frac{\int_0^1 da'\,\delta(a-a')\Xi_{M,0,1}(M+1,P,T,\nu,\sigma_0,a)}{\Xi'_{M,0,1}(M+1,P,T,\nu,\sigma_0)} \tag{6.9}$$

With this histogram we can calculate

$$y_{\text{grow}} = -k_B T \ln \frac{P(a=1|M+1,P,T,\nu,\sigma_0)}{P(a=0|M+1,P,T,\nu,\sigma_0)} \tag{6.10}$$

where y_{grow} is the reversible work needed to transform an interacting point particle (a=0) into a particle with a hard-core diameter σ_j (corresponding to a=1). In order to sample the full range of a-values from 0 to 1, it is necessary to use biased sampling. We employed multicanonical/umbrella sampling[70,43] to generate $P(a|M,P,T,\nu,\sigma_0)$.

To obtain the total interstitial free energy y_{add} we must still add the free energy change associated with the transformation of a non-interacting particle into an interacting point particle. This free energy change is determined by the ratio of the volumes accessible to the two types of particles:

$$y_{\text{add}} = y_{\text{grow}} - k_B T \ln\langle 1-\eta\rangle \tag{6.11}$$

where η denotes the volume fraction of the defect-free hard-sphere crystal. It is not necessary to confine the interstitial to a particular Wigner-Seitz cell, as interstitials diffuse quickly through the system. If this were not the case, both the scaled and the unscaled particle would have to be confined to a particular Wigner-Seitz cell (or even, to one particular interstitial cavity).

6.1.3 Vacancy Concentration

For the vacancies, the concentration x_V is given by $x_V \approx \exp y_V$, with y_V as the free energy difference between a defect-free system and a system with the same number of particles, but with one vacancy: $y_V = Y_{M+1,1,0} - Y_{M,0,0}$. We introduce the analogous free energy to y_{add}:

$$\begin{aligned}
y_V &= Y_{M+1,1,0} - Y_{M,0,0} \\
&= Y_{M+1,1,0} - Y_{M+1,0,0} + Y_{M+1,0,0} - Y_{M,0,0} \\
&= Y_{M+1,1,0} - Y_{M+1,0,0} + \mu(\sigma_0) \\
&= Y_{M+1,1,0} - Y_{M+1,0,0} + \mu_{\text{id}}(\sigma_0) + \mu_{\text{ex}}(\sigma_0) \\
&= -\left(Y_{M+1,0,0} - \left[Y_{M+1,1,0} + \mu_{\text{id}}\left(\sigma_0\right)\right]\right) + \mu_{\text{ex}}(\sigma_0) \\
&= -y_{\text{rem}} + \mu_{\text{ex}}(\sigma_0)
\end{aligned} \tag{6.12}$$

In this case, y_{rem} is the free energy difference between a perfect crystal and a crystal with one vacancy plus a non-interacting particle.

If we assume that we can sample a system which can switch one particle between being a normal particle ($b = b_n$) and a non-interacting particle ($b = b_i$), we can introduce the equilibrium probability $P(b|M,P,T,\nu,\sigma_0)$:

$$y_{\text{rem}} = -k_B T \ln \frac{P(b_n|M,P,T,\nu,\sigma_0)}{P(b_i|M,P,T,\nu,\sigma_0)} = -k_B T \ln \frac{\langle \pi(b_i \to b_n) \rangle}{\langle \pi(b_n \to b_i) \rangle} \tag{6.13}$$

where $\langle \pi(b_i \to b_n) \rangle$ is the mean transition probability from $b = b_i$ to $b = b_n$. Because a real particle can always switch to a non-interacting, particle, we can reduce the expression for y_{rem} to

$$y_{\text{rem}} = -k_T \ln \langle \pi(b_i \to b_n) \rangle \tag{6.14}$$

Now $\langle \pi(b_i \to b_n) \rangle$, the transition probability from a state of a system with a vacancy and a non-interacting particle to a perfect crystal, is related to the probability P_{ins} for the insertion of a (normal polydisperse) particle into the Wigner Seitz cell associated with a vacancy:

$$-k_T \ln \langle \pi(b_i \to b_n) \rangle = -k_B T (\ln P_{\text{ins}})$$

In practice, the simulation will consist of a collection of $M-1$ normal particles and one ideal polydisperse particle which we keep in the Wigner-Seitz cell of the vacancy. We then do multicanonical sampling, biasing on the number of overlaps that the ideal particle would create if it would be switched to a real particle, and get P_{ins} from the probability to create zero overlaps. This scheme is essentially identical to that of Bennett and Alder,[39] save for the multicanonical sampling.

6.2 Results

The simulations to calculate the point defect concentration were done at various points along the melting line of polydisperse hard sphere crystals, as taken from Ref. 23. The points chosen give a polydispersity of approx. 1.5%, 3%, 5% and 5.8%. The latter value corresponds to the maximum polydispersity attainable with the chemical potential difference function used. Here, the polydispersity s is defined as the normalized second moment of the particle diameter distribution

$$s \equiv \frac{\sqrt{\langle \sigma^2 \rangle - \langle \sigma \rangle^2}}{\langle \sigma \rangle} \tag{6.15}$$

All simulations were performed on $256(\pm 1)$ particle systems (a cubic fcc $4 \times 4 \times 4$ lattice); a simulation of a larger system in the monodisperse case in Chapter 5 shows that this particle number is sufficient for the required accuracy. For the (interstitial) calculation of y_{grow}, the $P(a|M+1,P,T)$ histograms were divided into 5 windows for which simulations were run in parallel. The multicanonical biasing weights were generated starting with the weights for the monodisperse case and took 10 – 80 runs of $4 \cdot 10^5$ MC sweeps (Monte Carlo cycles per particle) per CPU

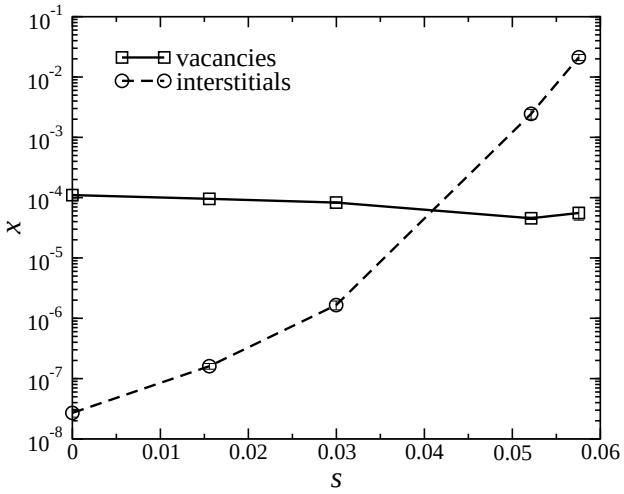

Figure 6.1: Point defect concentration (x) versus polydispersity (s).

to refine. The final results were obtained using typically 80 runs of $4 \cdot 10^5$ sweeps per CPU. In the case of vacancies there was one window for which about 20 runs of $1 \cdot 10^6$ sweeps were needed to equilibrate the weights after which about 40 runs of similar length were done for the final results. The equilibrium concentration of the two types of point vacancies as a function of different polydispersities is shown in Table 6.1 and Fig. 6.1.

The values of $\mu_{\mathrm{ex}}(\sigma_0)$, required for both the vacancy and interstitial concentration, were calculated using thermodynamic integration using the free energy differentials of Eq. 6.4. Integration was done along the P-ν points shown in Table 6.1, with 20 steps between each step and $1 \cdot 10^6$ averaging sweeps per step.

6.3 Discussion

The simulation results show a dramatic increase in the interstitial concentration with increasing polydispersity, while the vacancy concentration remains roughly similar over the full range of polydispersities. The increase in interstitial concentration can be attributed to the size of the interstitials: if the particle size distribution has non-zero width, the interstitials are smaller than the mean particle size in the crystal, as is shown in Fig. 6.2. This size difference between interstitials and the surrounding crystal is real: although the trial moves used in semigrand-canonical simulations are unphysical, the resulting size distribution of interstitials is real.

The influence of the small particles on the interstitial concentration can be illustrated by looking at the free energy of formation of a vacancy as a function of size. If we define a partial interstitial concentration $x_I(\sigma)$, we can, as in Eq. 6.7, express

ν	0	0.00025	0.001	0.004	0.0056
P	11.7	12.08	13.56	26.9	82.6
s	0	0.015562(3)	0.029974(7)	0.05213(3)	0.05755(5)
μ_{ex}	17.071	17.418	18.308	24.350	37.516
$\langle\sigma\rangle$	1	0.992	0.967	0.815	0.589
$\mu_{\text{ex}}(\langle\sigma\rangle)$	17.1	16.9	17.8	20.1	22.5
η	0.54329	0.54522(8)	0.54641(6)	0.55726(6)	0.56997(6)
$-\ln P_{\text{ins}}$	7.92(1)	8.098(9)	8.77(2)	13.68(4)	26.1(2)
x_V	$1.10(2)\cdot10^{-4}$	$9.55(9)\cdot10^{-5}$	$8.3(2)\cdot10^{-5}$	$4.6(2)\cdot10^{-5}$	$5(1)\cdot10^{-5}$
y_{grow}		32.2(1)	30.8(2)	29.5(2)	40.5(1)
x_I	$2.7(4)\cdot10^{-8}$	$1.6(2)\cdot10^{-7}$	$1.7(3)\cdot10^{-6}$	$2.4(5)\cdot10^{-3}$	$2.1(2)\cdot10^{-2}$

Table 6.1: Results for the vacancy and interstitial concentration for the polydisperse hard sphere system. The interstitial concentration for the monodisperse case was taken from Ref.[73] All free energies are in units of k_BT and the pressure is in k_BT/σ_0^3, with the errors in the last digit(s) shown in brackets. Here, ν is the polydispersity control parameter (see Eq. 6.2), η is the packing fraction, $\langle\sigma\rangle$ is the mean packing fraction, s is the polydispersity, as defined in Eq. 6.15, $\langle\sigma_I\rangle/\langle\sigma\rangle$ is the mean interstitial size relative to the mean particle size, P_{ins} is the particle insertion probability (see Eq. 6.1.3), y_{grow} is the free energy associated with growing an interstitial (see Eq. 6.10), x_V is the vacancy concentration and x_I is the interstitial concentration.

it in terms of the free energy of formation $f_I(\sigma)$ and the chemical potential:

$$x_I(\sigma) = \exp\left[-f_I(\sigma)+\mu(\sigma)\right] \tag{6.16}$$

Assuming that the total interstitial concentration is the integral of the partial concentrations:

$$x_I = \int_0^\infty d\sigma x_I(\sigma) \tag{6.17}$$

we can extract $f_I(\sigma)$, the free energy associated with creating an interstitial of size σ, because we know the chemical potential distribution and the partial interstitial concentration. The values for $f_I(\sigma)$ at the polydispersities from Table 6.1 are shown in Fig 6.3. To be able to compare values of $f_I(\sigma)$ over a large range of $\sigma/\langle\sigma\rangle$, the values for $x_I(\sigma)$ in this figure were obtained by fitting the values from the simulations with locally skewed Gaussians

$$x_I(\sigma) \approx a\exp\left[-b(\sigma-\langle\sigma_I\rangle)^2 - c(\sigma-\langle\sigma_I\rangle)^3\right] \tag{6.18}$$

The fits work very well for the values of σ which have been sampled during the simulation, and should yield meaningful results for the range shown in Fig. 6.3.

The similarity in slopes and actual values of the $f_I(\sigma/\langle\sigma\rangle)$ curves is striking; it means that, for the full range of polydispersities at which a crystal is stable, the partial interstitial concentration depends on the chemical potential distribution

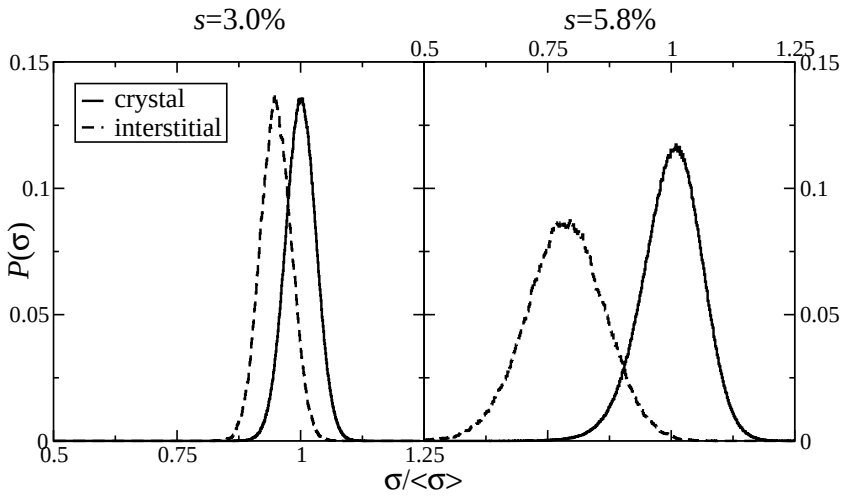

Figure 6.2: Normalized size distribution for the crystal and the interstitial for the polydispersities of 3.0% (left, $\nu = 0.001$) and 5.8% (right, $\nu = 0.0056$)

and an interstitial free energy which seems to be only weakly dependent on the polydispersity:

$$x_I = \int_0^\infty d\sigma \exp\left[\mu_{\text{ex}} - \frac{(\sigma-\sigma_0)^2}{2\nu} + \kappa\left(\frac{\sigma}{2\langle\sigma\rangle} - r_0\right)^2 + f_I^0\right] \tag{6.19}$$

with $\kappa = 741 k_B T/\sigma_0^2$, $r_0 = 0.338\sigma_0$ and $f_I^0 = 11.3 k_B T$ as fitted parameters from the points in Fig 6.3. The last two terms in the exponent are our approximation for $f_I(\sigma)$and, although the form of this equation was taken from the analytical estimate for the interstitial concentration of Eq. 5.49 of page 49 , which gives physical meanings to the values of κ and r_0 and has reasonable agreement for r_0, we stress that, here, κ and r_0 are simply fit parameters

The similarity in the $f_I(\sigma)$ can probably be attributed to the fact that the chemical potential at the mean particle size does not change much much over the range of polydispersities at the phase transition. As a consequence, the free energy associated with the creation of an interstitial of a given size does not depend strongly on polydispersity.

In the case of vacancies, similar considerations apply in a slightly different form; the vacancy concentration depends on the chemical potential and the free energy of removing a particle while keeping its lattice site. As argued above, they both stay relatively constant at melting for increasing polydispersities which causes the concentration of vacancies to remain roughly similar.

Because $f_I(\sigma)$ hardly depends on the width and, presumably, the shape of the particle size distribution, the small particle tail of the particle size distribution becomes crucial: those particles have the lowest $f_I(\sigma)$ and will form the most important contribution to the interstitial concentration. For example, at the near-Gaussian

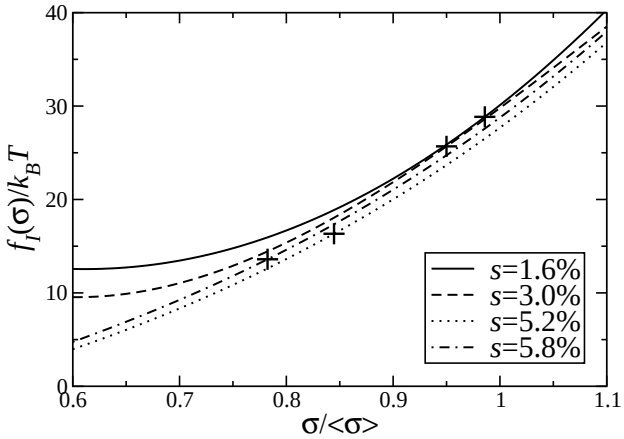

Figure 6.3: Interstitial free energy $f_I(\sigma)$ for different polydispersities s as a function of renormalized particle diameter $\sigma/\langle\sigma\rangle$. The polydispersities match those of Table 6.1. The crosses denote the means of the interstitial sizes for the corresponding polydispersities.

polydispersity of $s = 5.2\%$, obtained by setting $\nu = 0.004$, practically all particles with diameter smaller than 75% of the mean particle radius are interstitials. This implies that the polydispersity, as measured by the second moment of the particle size distribution in the liquid, is *not* a good predictor for the interstitial concentration in the solid. The *tail* of the particle size distribution in the liquid is hard to measure, yet it is all-important for the interstitial concentration.

In summary, we have shown that for polydisperse hard-sphere crystals along the melting curve, the interstitial concentration increases dramatically (going up to 2%) while the vacancy concentration remains relatively constant. This can be attributed to the fact that, with increasing polydispersity, there is an increasing probability of finding a particle small enough to have an appreciable probability of fitting in a hole of the underlying crystalline lattice.

This finding has practical implication for the preparation of colloidal crystals from slightly polydisperse solutions. As the presence of interstitials may affect the optical properties of colloidal crystals, it is important to control their concentration. The present calculations show that the interstitial concentration depends sensitively on the *tail* of the size distribution in the liquid phase. Hence, the polydispersity as such does not provide a reliable criterion to predict interstitial concentrations. Rather, it will be necessary to have an accurate representation of the functional form of the tail of the particle-size distribution (in particular, on the small-σ side).

7 Melting of Polydisperse Hard Disks

In the 1930's, Landau and Peierls showed that two-dimensional solids are qualitatively different from their 3D counterpart, as they lack long-ranged positional order (see e.g. 40). However, 2D crystals do have long-ranged bond-orientational order and, in this respect, they differ form the isotropic liquid phase where both translational and bond-orientational order are short ranged.

In the 1970's, Kosterlitz and Thouless suggested that the melting of two-dimensional crystals may be quite different form 3D melting. In particular, they proposed that melting in two dimensions may proceed via a continuous dislocation-unbinding transition.

Kosterlitz and Thouless[6,41] showed that the free energy associated with a single dislocation becomes negative when

$$K < 16\pi k_B T \tag{7.1}$$

where K is the Young's modulus of the crystal. At the point where $K = 16\pi k_B T$, dislocation pairs can unbind and, as solid with free dislocations 'flow' under shear, Kosterlitz and Thouless interpreted this temperature as the melting point. In a more detailed analysis, Halperin and Nelson[6] and Young,[74] showed that dislocation unbinding is not enough to complete the melting process. At the point where the condition of Eq. 7.1 is first satisfied, the system undergoes a (continuous) transition from a 2D crystal to a hexatic phase. The hexatic phase is characterized by short-ranged (exponentially decaying) positional order, but quasi-long-ranged (algebraically decaying) orientational order: the positional order is destroyed by the presence of the unbound dislocations. A second (continuous) phase transition is required to transform the hexatic phase into an isotropic liquid with short-ranged bond-orientational order.

The Kosterlitz-Thouless-Halperin-Nelson-Young (KTHNY) theory makes precise predictions about the behavior of the correlation functions of both the translational and orientational order parameters. It should be stressed, however, that the KTHNY theory describes only a possible scenario: it also possible that one or both of the continuous transitions are first order, and even that there is a direct first-order transition from the crystal to the isotropic fluid.

The KTHNY predictions sparked off an intensive search for real or model systems that would exhibit this two-stage melting process (for an early review see: ref. 75. More recent examples can be found in refs. 76, 77, 78 and 79).

Surprisingly, however, there is still no satisfactory answer to the question whether the KTHNY scenario applies even to the simplest of all two-dimensional model systems, namely hard, elastic disks. In fact, this system was the very first to be studied in any computer simulation.[80]

The reason why it is difficult to determine the nature of the melting transition, is that finite size effects tend to obscure the distinction between first order and continuous melting in 2D systems (see ref. 75).

In the case of hard disks, the early work by Alder and Wainwright suggested that the hard-disk melting transition was first order[81] (in the very early work of Metropolis et al.,[80] the computing power was insufficient to draw meaningful conclusions about the nature of the melting transition). The hard-disk melting problem was revisited many times after the suggestion of the KTHNY scenario, but the evidence is still ambiguous. Evidence for continuous melting was reported in ref. 82, while evidence for a first-order phase transition was presented in refs. 83,84,85,86. In addition, several publications could not distinguish between the two scenarios.[87,88,89] More recently, there has been some evidence for the KTHNY scenario[90,91,92] but, the matter still seems far from settled.

One possible route to tackle this problem would be to consider hard disks as a special case of a more general class of systems, and study possible trends in the phase behavior of this generalized model. In the present case, we consider the 2D hard-disk system as a special case of polydisperse disks. In 3D hard spheres, the melting transition is of first order. As the polydispersity is increased the difference in volume fraction of the coexisting solid and liquid phases widens with increasing polydispersity.[23,34] One might expect similar behavior in two dimensions if the solid-liquid transition would be of first order.

While polydispersity in two dimensional systems has been studied before, it was in the context of melting by increasing size dispersity for Lennard Jones systems[93] or in the context of a possible glass transition.[94,95] In the present Chapter, we examine the phase behavior of polydisperse hard disk systems.

7.1 The System

7.1.1 The Semigrand Canonical Ensemble

The model for polydispersity is based on the semigrand canonical ensemble;[69] this ensemble has previously been used to study the phase diagram of polydisperse 3D hard spheres.[23,34] The semigrand canonical ensemble can be seen as a hybrid version of the canonical ensemble and the grand canonical ensemble. It is characterized by a thermodynamic potential X that satisfies the following fundamental thermodynamic relation[96]

$$dX = -SdT - PdV - \int N(\sigma)\delta\mu(\sigma)d\sigma \tag{7.2}$$

Here S is the entropy of the system, T the temperature, P the pressure, V the volume. $N(\sigma)d\sigma$ denotes the number of particles with diameter between σ and

$\sigma + d\sigma$ and $\mu(\sigma)$ is the chemical of particles with diameter σ. We now add and subtract a term containing the chemical potential of a reference species σ_0

$$\int N(\sigma)\delta\mu(\sigma_0)d\sigma = d\mu(\sigma_0)\int N(\sigma)d\sigma = Nd\mu(\sigma_0) \tag{7.3}$$

from the complete differential:

$$dX = -SdT - PdV - Nd\mu(\sigma_0) - \int N(\sigma)\delta\Delta\mu(\sigma)d\sigma \tag{7.4}$$

where we replace $\mu(\sigma) - \mu(\sigma_0)$ with $\Delta\mu(\sigma)$. We now perform a Legendre transformation to a new ensemble that has N as a thermodynamic control parameter instead of $\mu(\sigma_0)$ (and P instead of V).

$$dY = -SdT + VdP + \mu(\sigma_0)dN - \int N(\sigma)\delta\Delta\mu(\sigma)d\sigma \tag{7.5}$$

which, in explicit form becomes (with the Euler equation)

$$\begin{aligned} Y(N,\Delta\mu(\sigma),P,T) &= U - TS + PV + N\mu(\sigma_0) - \int N(\sigma)\Delta\mu(\sigma)d\sigma \\ &= N\mu(\sigma_0) \end{aligned} \tag{7.6}$$

The partition sum for this ensemble is

$$\begin{aligned} \Upsilon(N,\Delta\mu(\sigma),P,T) = \int d\sigma^N \int dV \int ds^N \\ \exp\left(-\beta\left\{PV + U(V,s^N) - \Delta\mu(\sigma)N(\sigma)\right]\right\}\right) \end{aligned} \tag{7.7}$$

with $Y = -k_B T \ln\Upsilon$. For simulation purposes, the semigrand canonical ensemble can be interpreted as one where there is a constant number of particles that can change identity. This identity switching can be an extra move in a Monte Carlo simulation; in a polydisperse mixture, this would amount to a particle size change with an acceptance criterion based on the functional form for the chemical potential $\Delta\mu(\sigma)$.

As in ref. 23, we use the following functional form for the chemical potential

$$\Delta\mu(\sigma) = -\frac{(\sigma - \sigma_0)^2}{2\nu^2} \tag{7.8}$$

which, at zero density, will give a Gaussian particle size distribution according to the partition sum of Eq. 7.7. In practice, the size distribution is Gaussian-like at the densities of the crystalline phase.

7.1.2 Order Parameters

For the study of the properties of the phases and the phase transitions, some order parameters have been used that are standard in the studying of 2D melting[75] and

for which the KTHNY melting scenario makes explicit predictions.[6] We define the n-fold bond-orientational order at $\mathbf{x}_i$, the position of particle i, as

$$\psi_n(\mathbf{x}^i) = \frac{1}{N_i} \sum_{j=1}^{N_i} e^{in\theta_j(\mathbf{x}^i)} \tag{7.9}$$

where N_i is the number of neighbors and $\theta_j(\mathbf{x}^i)$ is the angle between an arbitrary (fixed) axis and the line connecting particle i with its j-th neighbor; two particles are neighbors if they share a Voronoi cell edge. For systems that tend to crystallize into triangular lattices, the leading bond-order parameter is the one for which $n = 6$. The global value of the order parameter is simply the mean of the local values.

The positional order is measured using the static structure factor $S(\mathbf{q})$ at one specific scattering vector $\mathbf{q}$ equal to a reciprocal lattice vector of a perfect crystal with orientation and lattice spacing taken from the system. To check for hexagonal crystalline positional order, the lattice vector a_0 is set to its ideal value for a given packing fraction:

$$a_0 = \left(\frac{\pi/\sqrt{12}}{\eta} \right)^{1/2} \tag{7.10}$$

The crystal orientation is taken from the mean angle obtained from the global hexagonal bond-orientational order parameter:

$$\Psi_6 = \frac{1}{N} \sum_{i=1}^{N} \psi_6(\mathbf{x}_i) \tag{7.11}$$

which specifies the orientation of one of the six equivalent crystal axes within an angular range $0 \leq \alpha < \pi/3$. Once the average orientation of the nearest-neighbor 'bonds' $\mathbf{a_0}$ has been specified, it is straightforward to deduce the orientation of the corresponding reciprocal lattice vector $\mathbf{G}$ through $\mathbf{G} \cdot \mathbf{a_0} = 2\pi$. The positional order parameter ζ of the crystal is then given by

$$\zeta(\mathbf{x}_i) = e^{i\mathbf{G}\cdot\mathbf{x}_i} \tag{7.12}$$

Radial correlation functions of the order parameters are defined as

$$g_6(r) = \langle \psi_6^*(\mathbf{0}) \psi_6(r) \rangle / g(r) \tag{7.13}$$

$$\zeta(r) = \langle \zeta^*(\mathbf{0}) \zeta(r) \rangle / g(r) \tag{7.14}$$

In two-dimensional systems, ζ is expected to decay to zero, either exponentially (short ranged order) or algebraically ('quasi-long ranged'). The KTHNY melting scenario makes predictions for the decay of the orientational order in the hexatic and phase: $g_6(r) \sim r^{-\eta_6}$ with $\eta_6 \to \frac{1}{4}$ at the melting of the hexatic phase into the liquid phase.[6,75]

7.1.3 Elasticity

Eq. 7.1 provides a very useful test to decide whether or not a 2D melting can be of the KTHNY type. If we find that Young's modulus drops below the 'magical' value of $16\pi k_B T$ in an otherwise stable solid, then it is very likely that this solid melts by dislocation unbinding. Conversely, if we find that this magical value is only crossed at densities where we know that the isotropic liquid phase is thermodynamically stable, then it is reasonable to assume that melting is a first-order transition. Often, however, the simulations do not provide a clear answer, as the point where $K = 16\pi k_B T$ is located in the intermediate density regime that may either be a two-phase region separating two stable phase, or the domain of the elusive hexatic phase.

The Young's modulus is defined through the shear (λ_L) and bulk (μ_L) Lamé elastic constants in 2D,

$$K = \frac{4a_0^2\mu_L(\mu_L+\lambda_L)}{2\mu_L+\lambda_L} \leq 16\pi \tag{7.15}$$

where a_0 is the equilibrium lattice spacing. The Lamé elastic constants are related to the second-order elastic constants (i.e. the elastic constants defined by the second derivative of the free energy to the Lagrangian strain; see chapter 2), through

$$\begin{aligned} C_{11} &= \lambda_L + 2\mu_L \\ C_{12} &= \lambda_L \\ C_{44} &= \mu_L - P \end{aligned} \tag{7.16}$$

To calculate the elastic constants at different polydispersities, the hybrid Monte Carlo – Molecular Dynamics method described in section 4.3 on page 33 was used. However, when specifying elastic constants of a polydisperse system, we should distinguish between 'quenched' and 'annealed' elastic constants. Quenched elastic constants measure the second strain derivative of the free energy of a polydisperse crystal with a 'frozen in' size distribution: i.e. the particle-size distribution is assumed not to respond to the deformation. In contrast, the 'annealed' elastic constants measure the second strain derivative of the semi-grand potential. In this case, the particle size distribution is assumed to respond to the deformation. The quenched constants are the ones that are presumably measured in mechanical experiments that probe the elastic deformation of a polydisperse solid. But the annealed constants describe the equilibrium state of a deformed polydisperse solid. In order to determine the critical value for Young's modulus in a polydisperse 2D solid, we computed the annealed elastic constants, as these determine the equilibrium behavior of the system.

The quenched elastic constants described in section 4.3 will be larger than the annealed quantities, because of the concavity of the free energy. Hence the corresponding 'quenched' Young's modulus will only reach the instability limit $K = 16\pi$ at lower densities.

The strains used in the elastic constant determination were

$$\alpha_{ij}^1 = \begin{pmatrix} 1+a & 0 \\ 0 & 1+a \end{pmatrix}$$

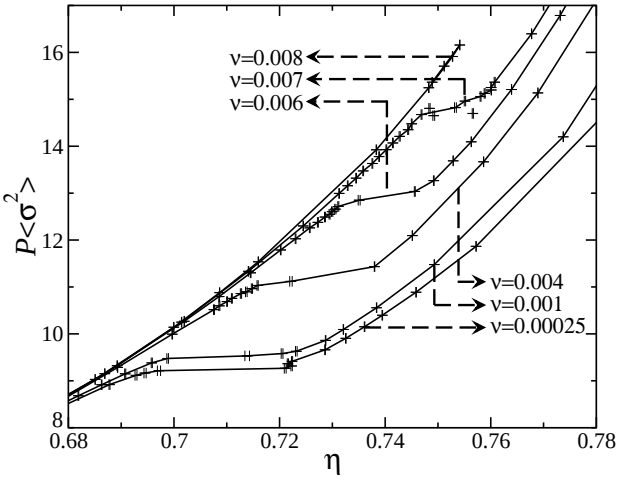

Figure 7.1: Calculated equations of state (with normalized pressure) for varying polydispersity control parameter ν. System size is 4012 particles.

$$\alpha_{ij}^2 = \begin{pmatrix} 1 & b \\ 0 & 1 \end{pmatrix} \tag{7.17}$$

with a as the (small) strain parameter. The resulting stress derivatives, according to Eq. 2.28, give us

$$\begin{aligned} \frac{dT_{11}}{da} &= \frac{\partial T_{11}}{\partial \alpha_{11}^1} + \frac{\partial T_{11}}{\partial \alpha_{22}^1} = C_{11} + C_{12} = 2\lambda_L + 2\mu_L \\ \frac{dT_{12}}{db} &= \frac{\partial T_{12}}{\partial \alpha_{12}^1} = C_{44} + P = \mu_L \end{aligned} \tag{7.18}$$

allowing us to calculate the Young's modulus of Eq. 7.15.

7.2 Simulations

The simulations were performed on systems containing $59 \times 68 = 4012$ particles, with a chemical potential disitribution width ('polydispersity') parameter ν (see Eq. 7.8) varying between $\nu = 0.00025$ and $\nu = 0.008$. For higher values of ν (higher polydispersities), the equilibration was exceedingly slow, even with the combined volume–particle radius sampling: equilibration took 1.3×10^6 to 2.5×10^6 MC steps per particle and data were sampled during 1×10^6 steps per particle; around 20% of steps were devoted to particle radius steps. For $N = 4012$, the simulation time was 6–8 hours on an Athlon 1600+ CPU.

To speed up the simulation, the coupling between mean particle size and system size is exploited to remove the global volume moves and simultaneous system+particle size scaling was introduced. This improves the statistics of sampling

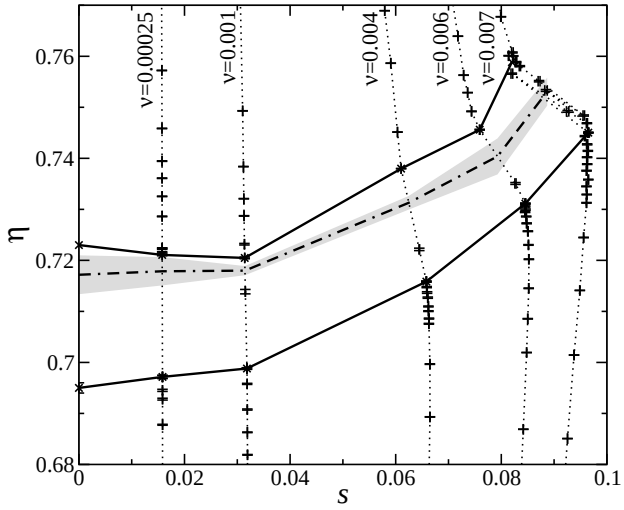

Figure 7.2: Packing fraction η as a function of polydispersity s for varying ν. The boundaries of the apparent density gap are shown as the solid lines; the density gap of the monodisperse ($s = 0$) case is taken from data by Jaster,[88] with $N = 4096$. The dashed line shows the location of packing fractions (with matching polydispersities) where is extrapolated to be $K = 16\pi$; the gray area denotes an estimate of the size of the error.

considerably.[23] It turns out that, in practice, a real simultaneous system+particle size scaling is at least as fast as the analytical integration of the scaling part of the partition sum also described in Ref. 23.

The resulting equations of state are shown in Fig. 7.1. From this figure, it is clear that the phase transition, which is around packing fraction $\eta \approx 0.70$ for the monodisperse case,[88,89,87] shifts to higher packing fractions and higher pressures with increasing polydispersity. At $\nu = 0.008$, the system cannot be made to freeze at all. A similar phenomenon was observed in Ref. 23. It is due to the choice of the functional form for the chemical potential (Eq. 7.8). In addition, for $\nu = 0.007$, it is extremely difficult to equilibrate the system properly in the vicinity of the phase transition.

As is the case for 3D spheres, the liquid branches of the equations of state very nearly superimpose.[23] However, near the phase transition, the pressure appears to increase slightly with polydispersity. Upon further compression, the system undergoes a phase transition with an apparent density gap. However, because of the relatively small system size, the presence of such an apparent density gap is also compatible with continuous melting. We find that the density gap decreases with increasing polydispersity.

In Fig. 7.2 we plot the variation in polydispersity upon freezing. As a measure for the polydispersity, we use the normalized second moment of the particle size distribution $s \equiv \sqrt{\langle\sigma^2\rangle/\langle\sigma\rangle^2 - 1}$. In the same figure, the apparent density gap is

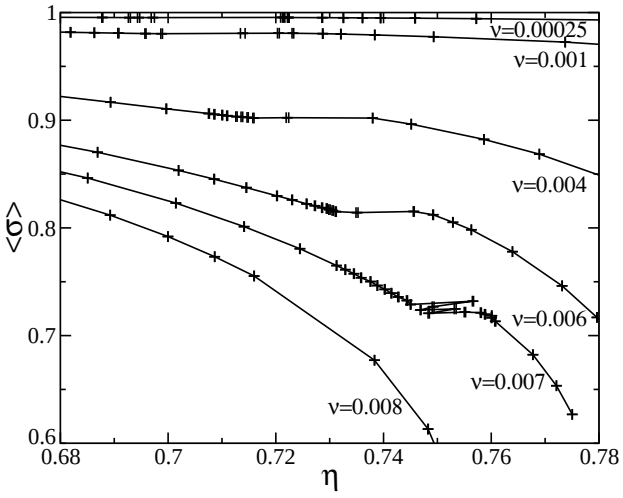

Figure 7.3: Mean particle diameter $\langle\sigma\rangle$ as a function of packing fraction η for the different values of the polydispersity control parameter ν.

also shown (the borders of the density gap shown here are simply the solid with the lowest packing fraction and the liquid with the highest packing fraction found in the simulations). As in the 3D case,[23,34] the freezing point moves to higher volume fractions as the polydispersity is increased and size fractionation is also increased. But, whereas the density gap widens upon freezing in 3D, it appears, if anything, to decrease in 2D (except for the possibly seemingly poorly equilibrated case of $\nu = 0.007$). Additionally, the maximum polydispersity at which the solid seems to remain stable (around 8%) is considerably higher than in 3D (5.7%).

In the semigrand-canonical ensemble, the system equilibrates to a mean particle size, dependent on pressure and ν. Fig. 7.3 shows this mean particle size as a function of packing fraction: the phase transitions show up as jumps in the packing fraction, but not in the mean particle size. This means that there is no particle size fractionation (the mean of the particle diameter distribution does not change) while there is, as can be seen in Fig 7.2, polydispersity-fractionation (the width of the particle diameter distribution changes).

An example of the behavior of the order parameters near the phase transition is shown in Fig. 7.4. The positional and orientational order both increase sharply (but not quite simultaneously) in the region of the phase transition, similar to what one finds for monodisperse hard disks. Although the decay of the orientational correlation function $g_6(r)$ goes with $r^{-\frac{1}{4}}$ as predicted by the KTHNY scenario for the hexatic at the hexatic-crystal transition, this seems to be a coincidence, because a further simulation of the same configuration yields a different (but still algebraic) decay rate. This indicates that the typical decay 'time' of fluctuations in the system exceeds the typical length of the (rather long) simulations.

We stress that all observations reported thus far are consistent with either a

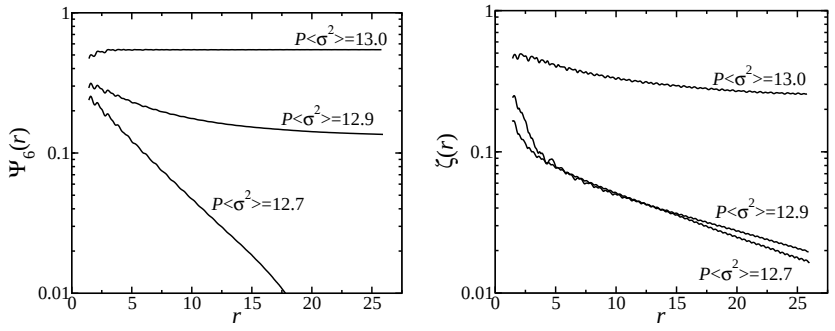

Figure 7.4: Example of the decay of the orientational (left) and positional (right) order parameters over the phase transition, for $\nu = 0.006$. The decay of the positional order parameter, $g_6(r)$ goes as $g_6(r) \propto r^{-\frac{1}{4}}$ at the intermediate pressure $P\langle\sigma^2\rangle = 12.7$. The positional order parameters decay exponentially for both lower pressures.

KTHNY scenario or a weak first-order transition. The KTHNY scenario however, is based on the assumption that the concentration of bound dislocations in the crystal phase is low; dislocation interaction is not taken into account and the Kosterlitz-Thouless normalization is based on an expansion in the dislocation unbinding length which may be unrealistically long for high dislocation concentrations. We measured the concentration of bound dislocation pairs (see Fig. 7.5). In the figure, we show the concentration of seven-coordinated particles. Because in the crystal the number of eight or more coordinated particles is negligible, and as the number of point defects turns out to be an order of magnitude lower than the number of bound dislocations,[89] the number of seven-coordinated particles is a good measure of the dislocation count. At the melting point (the boundary of the apparent density gap) the dislocation concentration varies from 1% to more than 3%. As the concentration of dislocation pairs depends sensitively on the dislocation core energy, this suggests that the core energy is rather low. Note that a core energy less than 2 to $4k_BT$ is not compatible with KTHNY melting.[97,98]

7.2.1 Elastic Constants

The elastic constants were measured using the method described in section 7.1.3, using simulations of 412 particles, equilibrating for 4×10^6 MC steps and 4×10^4 MD collisions per particle and measuring up 5×10^6 MC steps and 1.5×10^6 MD collisions per particle. Earlier work[89] had shown that the elastic constants are not significantly affected by the presence of point defects such as vacancies. Away from the KTHNY transition, the elastic constants are not very sensitive to finite-size effects.[84] Of course, this is not true close to a KTHNY transition, but this will turn out to be less relevant for the present system because we always observe melting before we get into the 'danger zone'.

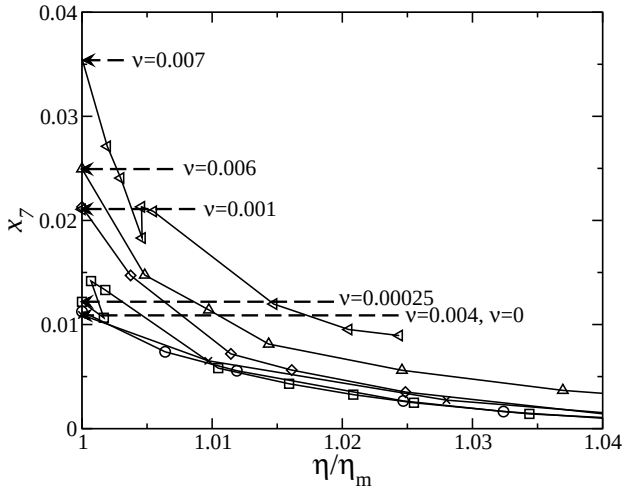

Figure 7.5: Concentration of seven-coordinated particles x_7 (a measure for the number of dislocations) as a function of packing fraction relative to the melting packing fraction (determined by the boundaries of the apparent density gap).

The results of the simulations are shown in Fig. 7.6; here an exponential of the Young's modulus, $\kappa = (1 - 16\pi/K)^{\nu_{KT}}$, where ν_{KT} is the Kosterlitz-Thouless renormalization exponent, which has a value of $\nu_{KT} \approx 0.36963$.[6] This form is chosen because close to the KTHNY transition, the Young's modulus — expressed as function of the difference between the packing fraction η and the packing fraction at the KTHNY, η_{KT} — behaves as[75]

$$\frac{K}{16\pi} = \frac{1}{1 - c(\eta - \eta_{KT})^{\nu_{KT}}} \tag{7.19}$$

The measured κ values are then fitted to a second-order polynomial. The results for the monodisperse case ($\nu = 0$) are similar to those by Wojciechowski and Brańka[84,46] and by Bates and Frenkel.[89]

From the locations of the $K = 16\pi$ line in Fig. 7.2 it is clear that the situation with respect to the type of phase transition is, even for higher polydispersities, similar to that of the monodisperse system; the points seem to follow — within the statistical uncertainties — not only the loci of the phase transitions, but also the position within the density gap.

7.3 Conclusion

In this chapter, we explored the effect of polydispersity on the nature of the 2D melting transition is a system of 2D hard disks.

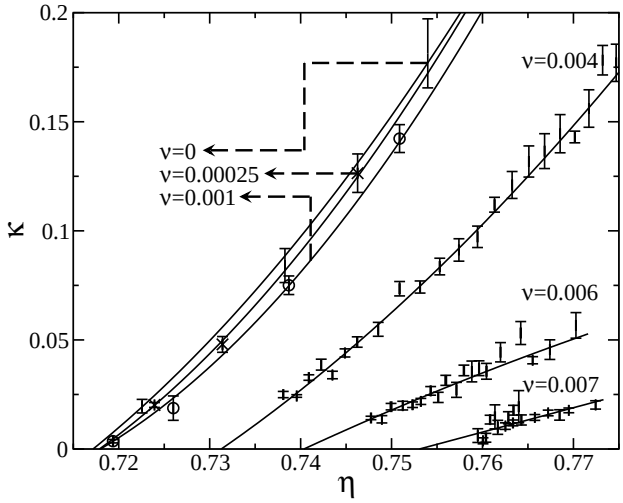

Figure 7.6: Fractional exponent of the Young's modulus $\kappa = (1-16\pi/K)^{\nu_{\mathrm{KT}}}$ with $\nu_{\mathrm{KT}} = 0.3696$, for the different polydispersities, as a function of packing fraction. The lines are the fits to determine the locations of $K = 16\pi$.

We find that the solid-liquid phase transition shifts to higher packing fractions as the polydispersity increases, and that polydispersity fractionation takes place in the region of the phase transition. The maximum polydispersity at which the solid can be stable is larger than in 3D hard spheres.

The density-polydispersity gap, be it real or apparent, does not seem to increase in size with increasing polydispersity. The fact that the points for which $K = 16\pi$ appear to be located in the two-phase region, supports the assumption that the melting transition is first order. Even if this should not be the case, the high dislocation concentration will presumably have an effect on the KTHNY predictions.

8 Monte Carlo Study of Hard Pentagons

In this chapter we consider the freezing of a liquid consisting of molecules that have a shape that prevents close packing in a regular crystal. In particular, we consider a two-dimensional system of hard pentagons. We have studied the phase behavior of hard pentagons in isobaric and isotensic Monte Carlo simulations. On increasing pressure the system first goes from an isotropic liquid phase to a rotator phase on a triangular lattice. At higher pressures, it undergoes a first order phase transition at which orientational order sets in and the lattice is distorted, thus partially accommodating the frustration due to the mismatch between particle and lattice symmetries. The resulting phase is similar to the 'striped' phase in the compressible antiferromagnetic Ising model on a triangular lattice.

8.1 Background

Shape is one of the main characteristics of molecules. Simple models, in which molecules are represented by hard objects without any interaction apart from their excluded volume, have been very successful in the analysis of the phase behavior of liquids and liquid crystals.[4]

In this work we have investigated how a liquid behaves under pressure, if particle geometry does not 'fit' to the crystal structure, into which the liquid tends to freeze. The simplest objects which fulfill this requirement are two-dimensional pentagons. At low densities they act like hard disks, that form hexagonal structures. At high densities the fivefold symmetry forbids hexagonal ordering.

A system of pentagons has already been studied in an 'experimental simulation', by Duparcmeur, Gervois and Troadec.[99] These authors studied the compaction of macroscopic hard styrene pentagons on a blowing air table. These pentagons undergo thermal-like motion and experience, apart from hard pairwise pentagonal interaction, a soft repulsion due to the hydrodynamics of the air flowing from under the pentagons. This study focused on the high-density (presumably close-packed) crystal and its defects; no mention of a rotator crystal was made and information on the nature of any phase transition was experimentally inaccessible.

A model related to pentagons are hard pentamers, objects made from five circular disks arranged with their centers on the vertices of a pentagon. Those were studied by Brańka and Wojciechowski in computer simulations and mechanical

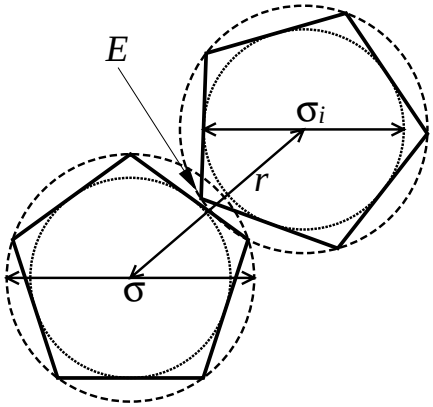

Figure 8.1: Sketch for the overlap algorithm.

simulations.[100, 101, 102] We will refer to similarities and differences of our results in the respective result sections of this chapter.

We have performed isobaric and isotensic Monte Carlo simulations of hard pentagons. In an isotensic simulation the pressure tensor is imposed instead of the pressure. The system is allowed to relax to the pressure tensor by sampling the box shape. Because the box shape is not necessarily rectangular, the system may form crystalline phases that are not commensurate with a rectangular box.[50, 103, 55]

The order parameters, by which we have identified the structures obtained in the simulations, are defined in section 8.2.2. In section 8.2.3 the numerical data are presented and in section 8.3 we compare the freezing behavior to the transition in the compressible antiferromagnetic Ising model on a triangular lattice. Section 8.4 sums up our conclusions.

8.2 Simulations

8.2.1 Overlap Criterion

The algorithm for the overlap criterion required for the Monte Carlo simulations, consists of 3 steps (See Fig. 8.1 for details):

1. If the distance r between the pentagons is bigger than the diameter of the outer circle, σ, the pentagons can't overlap.

2. If r is smaller than the diameter $\sigma_i = \sigma \cos \pi/5$ of the inscribing circle, the pentagons always overlap.

3. The edge E of either pentagon which is closest to the center of the other

pentagon (in this case b) is sought. If this edge is inside the other pentagon, the pentagons overlap, otherwise they don't.

To test whether E is inside the other pentagon, we can draw a line from E in any direction. If the line crosses a border of the pentagon an odd number of times the point is inside, otherwise it's outside. In practice we choose the line to be horizontal, so we only have to check crossings of the line with border pieces that have a bigger *and* smaller y coordinate of the ends.

8.2.2 Order Parameters

We computed several quantities that reflect positional or orientational ordering of the system.

We define the local values of the order parameters at location $\mathbf{x}_i$, which is the location of pentagon i. The global order A for the local order parameter $a(\mathbf{x}_i)$ is then defined as

$$A = \frac{1}{N}\left|\sum_i a(\mathbf{x}_i)\right| \tag{8.1}$$

(we use absolute values because most order parameters have imaginary components).

First, the particle orientational order parameter $\phi_n(x_i)$ is defined as

$$\phi_n(\mathbf{x}_i) = e^{in\theta_i} \tag{8.2}$$

where θ_i is the angle between the orientation of pentagon i and an arbitrary fixed axis.

For bond-orientational order we use

$$\psi_n(\mathbf{x}_i) = \frac{1}{N_i}\sum_j e^{in\theta_{ij}} \tag{8.3}$$

where N_i is the number of neighbours of particle i, the sum is over the neighbours of i and θ_{ij} is the angle between an arbitrary fixed axis and the line connecting particles i and j. This is one of the usual order parameters used in studying 2D melting.[75] Two particles are neighbours if they share an edge in the Voronoi tessellation of the collection of points that are the centers of the pentagons.

The positional order is measured using the static structure factor $S(\mathbf{q})$ at one specific scattering vector $\mathbf{q}$ equal to a reciprocal lattice vector of a perfect crystal with orientation and lattice spacing taken from the system. To check for hexagonal crystalline positional order, the lattice vector a is set to its ideal value for a given packing fraction:

$$a = \sqrt{\frac{\pi}{2\sqrt{3}\eta}} \tag{8.4}$$

The crystal orientation is taken from the mean angle obtained from the global hexagonal bond-orientational order parameter:

$$\Psi_6 = \frac{1}{N}\sum_{i=1}^{N} \psi_6(\mathbf{x}_i) \tag{8.5}$$

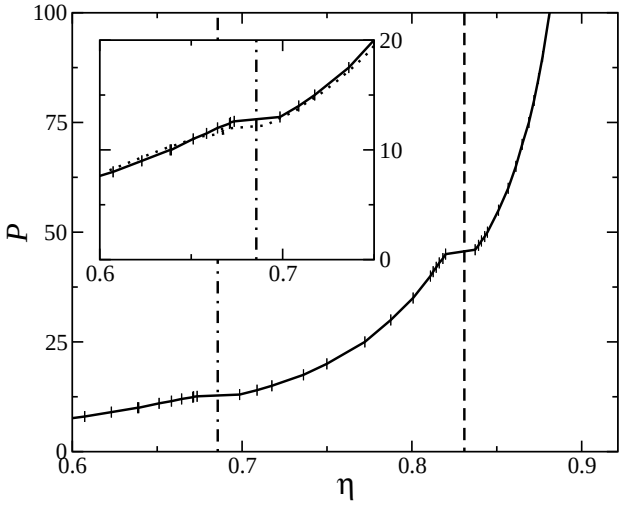

Figure 8.2: Pressure P versus packing fraction η: The equation of state shows two discontinuities; one a low density (see the inset) and one a higher density. The dotted line is a scaled 2D hard-disk equation of state.

which gives an orientation α between $0 \leq \alpha < \pi/3$ on the complex plane. Together, the lattice vector and the orientation give a reciprocal lattice vector $\mathbf{G}$ through the definition $\mathbf{G} \cdot (ae^{i\alpha}) = 2\pi$. The hexagonal crystal positional order parameter ζ now is

$$\zeta(\mathbf{x}_i) = e^{i\mathbf{G}\cdot\mathbf{x}_i} \tag{8.6}$$

The same order parameter with different reciprocal vector $\mathbf{q}$ can be used for non-hexagonal lattices.

To get an measure of the coupling between the local bond order and particle orientation, the combined order parameter

$$\phi_m^* \psi_n = \frac{1}{N_i} \sum_{j=1}^{N_i} e^{i(m\theta_{ij} - n\theta_i)} \tag{8.7}$$

was used.

8.2.3 Phase Behaviour

The simulations were performed with 4736 pentagons. Equilibration took $1.5 \cdot 10^6$ MC steps per particle (sweeps) and production runs were of $1.0 \cdot 10^6$ sweeps. Results are given in length units of σ (diameter of pentagon perimeter) and energy units of $k_B T$.

In Fig. 8.2, the pressure P is plotted versus the packing fraction η; the fraction of area covered by pentagons. There are two discontinuities in packing fraction

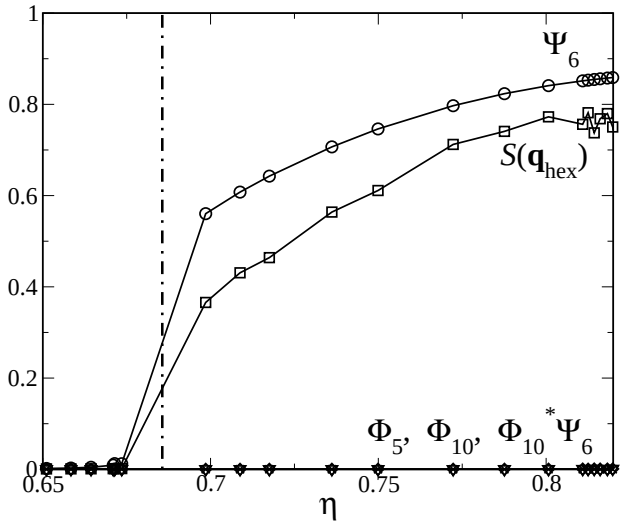

Figure 8.3: Order parameters near the low density phase transition: The sixfold bond order Ψ_6 and the structure factor of the corresponding triangular lattice $S(\mathbf{q}_{\rm hex})$ increase.

which indicate phase transitions. While the second (higher density) phase transition seems to show a clear density gap, the nature of the transition is not so clear for the first one. This situation is similar to the 2D hard disk melting scenario; there it is difficult to decide on the basis of simulations of systems of finite size between a first-order phase transition and a KTHNY dislocation-unbinding melting scenario involving a hexatic phase (see, for example, chapter 7 or refs. 6,75). Phase transitions that appear to be first-order in the simulations can be compatible with a continuous melting scenario in the thermodynamic limit. The similarity between the present case of the low-density phase transition of the pentagons and the hard disk fluid-solid phase transition can be seen in Fig. 8.2, where the scaled hard disk equation of state is superimposed on the pentagon equation of state.

The density dependence of the order parameters in the vicinity of the low-density phase transition, are shown in Fig. 8.3 . The sixfold bond order Ψ_6 (solid line) and the structure factor of the corresponding lattice $S(\mathbf{q}_{\rm hex})$ (dotted line) increase. As we shall see in the high-density crystal, the value of the structure factor is a sensitive measure for the exact lattice type and indicates that it is hexagonal.

Fig. 8.3 also shows the absence of global 10-fold (and therefore 5-fold) orientational order. The correlation of 10-fold order[104]

$$g_{\Phi_{10}}(r) = \langle \phi_{10}^*(0)\phi_{10}(r)\rangle / g(r) \tag{8.8}$$

is shown in Fig. 8.4: the decay of the orientational order is rapid and initially exponential and the simulation box appears to be large enough relative to the decay length of the orientational order.

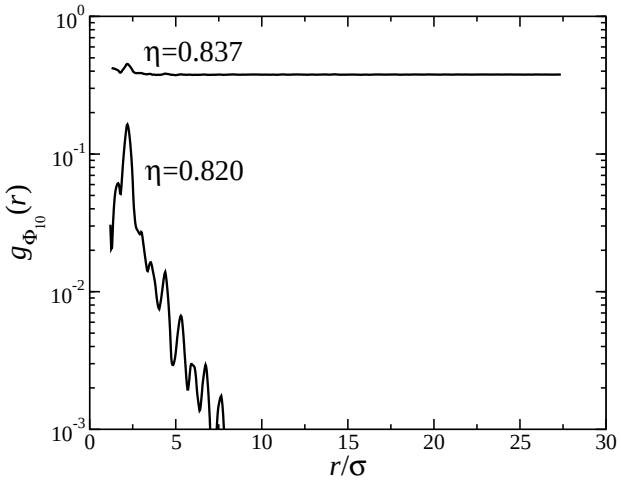

Figure 8.4: The orientational correlation function $g_{\Phi_{10}}(r)$ for the highest simulated pressure of the low-density solid ($P = 45$, $\eta = 0.820$) and for the lowest simulated pressure of the high-density crystal phase ($P = 46$, $\eta = 0.837$). Beyond r approximately 10σ, the low-density values merely show statistical noise.

Higher order orientational order that incorporates both the 5-fold symmetry of the particles and the 6-fold symmetry of the lattice, Φ_{30}, or the coupling of that to orientational order ($\Phi_{30}^*\Psi_6$), could not be distinguished from zero, presumably because of the high sensitivity to thermal fluctuations (low Debye-Waller factor) associated with such high-order orientational order parameters in two dimensions.

At the higher density phase transition (see Fig. 8.5) the bond order Ψ_6 increases further, but the corresponding structure factor $S(\mathbf{q}_{\text{hex}})$ drops to zero. The system still has six-fold bond order, but the particles are no longer positioned in a regular triangular lattice. At the same transition, $5n$-fold orientational ordering sets in: in particular, Φ_{10} grows strongly. However, Φ_5 remains effectively equal to zero. The reason why we observe only 10-fold (in general, $10n$-fold) ordering is that the particles align in 'antiparallel' fashion, cancelling Φ_5 exactly.

Together with the absolute orientational order, the coupling between orientational and bond-orientational order, in this case $\Phi_{10}^*\Psi_6$ goes from zero to a finite value at the transition. The structure that forms is a striped phase of antiparrallelly packed pentagons, as the snapshot from Fig. 8.6 shows.

To our knowledge, there exists no proof that the regular arrangement of Fig. 8.6 (shown schematically in Fig. 8.7) is the densest possible pentagon packing on a plane, but it has been conjectured by Henley[105] that this is, in fact, the case. Our simulations, and the experiments by Duparcmeur et al[99] spontaneously form this arrangement at the highest pressures. The arrangement itself, as shown in Fig. 8.7,

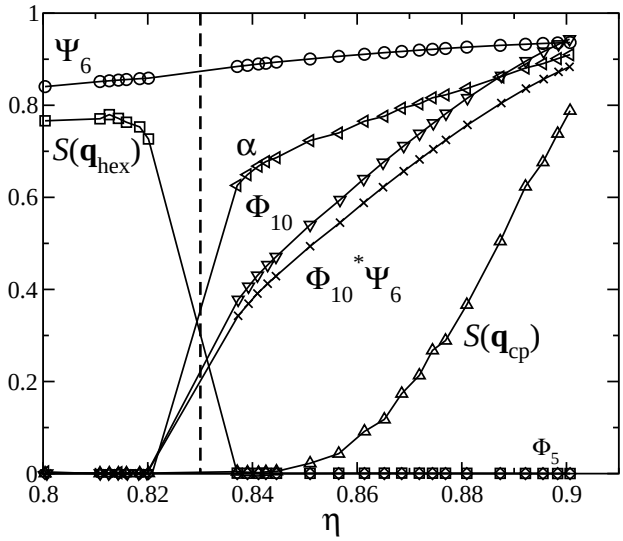

Figure 8.5: Order parameters near the (higher-density) rotator–crystal phase transition.

is a distorted hexagonal packing with a unit cell of size

$$\begin{aligned} a_x^{\mathrm{cp}} &= \sigma\frac{5+\sqrt{5}}{8} \approx 0.905 a_x^{\mathrm{hex}} \\ a_y^{\mathrm{cp}} &= \sigma\sqrt{\frac{9}{32}\left(5+\sqrt{5}\right)} \approx 0.824 a_x^{\mathrm{hex}} \end{aligned} \tag{8.9}$$

in which two particles are located at

$$\begin{aligned} \mathbf{r}_0 &= (0,0) \\ \mathbf{r}_1 &= \left(\sigma\left[\frac{1}{16}+\frac{3}{16}\sqrt{5}\right], \frac{a_y^{\mathrm{cp}}}{2}\right) \end{aligned} \tag{8.10}$$

with a maximum packing fraction of 0.92131.

Figure 8.5 also shows the density dependence of the appropriate structure factor $S(\mathbf{q}_{\mathrm{cp}})$ for this type of distorted hexagonal lattice. The figure clearly shows that this order parameter starts to grow at the phase transition. In addition we also followed the behavior of the 'aspect-ratio order parameter', defined as

$$\alpha = 1 - \left(\frac{a_y}{a_x} - \frac{a_y^{\mathrm{cp}}}{a_x^{\mathrm{cp}}}\right) \Bigg/ \left(\frac{a_y^{\mathrm{hex}}}{a_x^{\mathrm{hex}}} - \frac{a_y^{\mathrm{cp}}}{a_x^{\mathrm{cp}}}\right) \tag{8.11}$$

where a_x and a_y are the measured lengths of the unit cell edges corresponding to a_x^{cp} and a_y^{cp} in Fig. 8.7. a_x^{hex} and a_y^{hex} are the equivalent hexagonal unit cell dimensions.

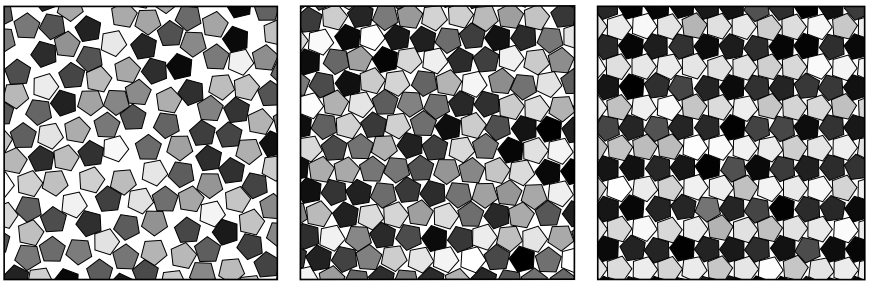

Figure 8.6: Partial snapshots from the three phases. On the left the fluid phase, in the middle the rotator crystal and to the right the high-density crystal. The pentagons are shaded according to their absolute orientation.

This order parameter goes from 0 to 1 as the lattice distorts from hexagonal to the close-packed structure, as can be seen in Fig. 8.5.

Upon compression, the system in the rotator-phase forms a close packed crystal with a large concentration of defects in the form of 'kinks' in the stripes of the parallelly aligned pentagons, similar to what the pentagon packings of Duparcmeur et al.[99] showed. In addition, hysteresis prevents crystallization until pressures are well beyond those at which the crystal melts.

The size of the density gap, the hysteresis and the jumps in order parameter values (especially the one in α) strongly suggest a first order phase transition between the rotator phase and the close packed crystalline phase. Given the large number of particles involved it is unlikely that it is a finite size effect.

8.3 The Elastic Antiferromagnet on a Triangular Lattice

Ising antiferromagnets — Ising models with a positive spin-spin coupling constant J — are often used as models of the order–disorder transition in alloys. 'Ordering' in an alloy usually implies that unlike particles tend to be neighbours, just as neighboring spins tend to align antiparallel in an antiferromagnet. However, in alloys with a face-centered cubic (fcc) lattice, this type of ordering leads to frustration, as antiferromagnetic order does not 'fit' the fcc structure: the lattice cannot be filled up with alternating rows of up and down spins in all directions. This 'frustration' results in the formation of a disordered ground state.

The two-dimensional analog of this problem, the antiferromagnet on a compressible triangular lattice, has been studied extensively.[106,107] In this model, spins are free to move around their lattice position and the neighbouring spin-spin interaction parameter $J(i,j)$ is a function of the distance between the spins i and j. In addition, there is a linear elastic term in the Hamiltonian with the strain depending on the spin positions, introducing the additional requirement of a slowly varying

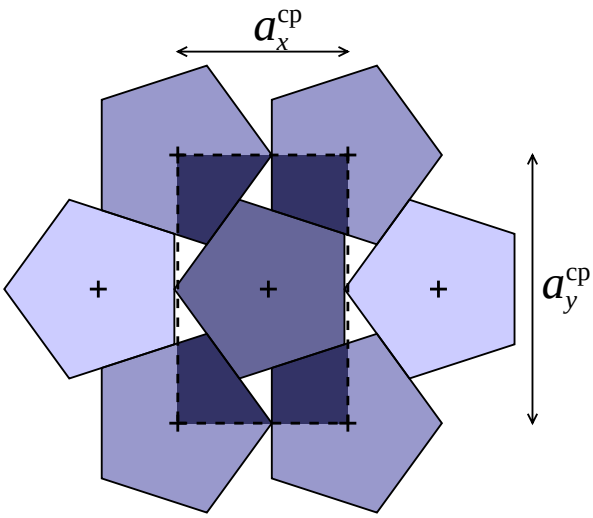

Figure 8.7: Close packing: pentagons pack onto a distorted triangular lattice. The unit cell is shown as the rectangular area with darker shades; its dimensions and particle positions are given by Eq. 8.9 and Eq. 8.10, respectively.

displacement field. It has been shown that the coupling to lattice distortions alleviates the frustration and allows for the existence of an ordered ground state.[107] This new phase, the 'stripe' phase, has two broken symmetries: the Ising symmetry and the three-state symmetry of bonds in the underlying lattice.

The transition to this stripe phase has been found to be strongly first order under the assumption of a mean strain field.[107] When fluctuations in the spin positions are taken into account, the transition is still strongly first order for low values for the spin-displacement coupling constant relative to the elastic constants, but becomes weakly first-order for higher values of the spin-displacement coupling constant.[108]

The high-density phase transition in the pentagon system resembles this transition. Frustration due to the mismatch in particle and lattice geometry is removed by straining the lattice into the non-hexagonal, striped phase shown in Fig. 8.6 and Fig. 8.7. Here, the symmetries that are broken are the 'left-right' symmetry (the direction where a pentagon corner is pointing in a bond direction) and a three-fold symmetry involving the choice of direction of the stripes. The size of the density gap, the behaviour of the order parameters α and $\Phi_{10}^{*}\Psi_6$ suggest a moderately weak first-order transition similar to what is seen by Gu et al.[108] for the intermediate regime of the spin-displacement coupling constant strength.

8.4 Conclusion

We have investigated the phase behavior of hard pentagons using Monte Carlo simulations. Pentagons constitute a simple model for particles, whose geometry conflicts with the simplest (2D) crystal symmetry.

At low pressures pentagons exhibit a positionally and orientationally disordered isotropic phase. On increasing the pressure, the system undergoes a 2D hard disk-like phase transition to a positionally ordered, but orientationally disordered rotator phase. We do not find traces of fivefold symmetry in the orientational order parameters.

On further increase of pressure, the non-spherical shape of the particles begins to influence the phase behavior. The system undergoes a first order phase transition, in which the orientational degrees of freedom are frozen and, simultaneously, the lattice becomes distorted.

As pentagons cannot be packed densely in a regular triangular lattice, the positional order changes at this phase transition. The resulting distortion of the lattice alleviates the frustration of orientational and positional order. This effect is well known in the context of the antiferromagnetic Ising model. The transition to the high density phase in hard pentagons resembles the transition to the ‘striped’ phase in the antiferromagnetic case.

One way of varying the polygon analog of the spin-displacement coupling constants would be to look at the behaviour of heptagons. Heptagons should have a lower ‘misalignment’ penalty to displacement (the analog of the spin-displacement coupling constant) and the rotator phase–striped crystal transition should should therefore be more strongly first-order.

Bibliography

[1] BRIDGMAN, P. W. Change of phase under pressure. I. the phase diagram of eleven substances with especial reference to the melting curve. *Phys. Rev. 3*, 3 (1914), 153.

[2] ALDER, B. J., AND WAINWRIGHT, T. E. Phase transition for a hard sphere system. *J. Chem. Phys. 27* (1957), 1208.

[3] WOOD, W. W., AND JACOBSON, D. J. Preliminary results from a recalculation of the Monte Carlo equation of state of hard-spheres. *J. Chem. Phys. 27* (1957), 1207.

[4] ALLEN, M. P., EVANS, G. T., FRENKEL, D., AND MULDER, B. Hard convex body fluids. In *Advances in chemical physics, Volume LXXXVI*, I. Prigogine and S. A. Rice, Eds. John Wiley & Sons, New York, 1993, pp. 1–166.

[5] BOLHUIS, P. G., AND FRENKEL, D. Tracing the phase boundaries of hard spherocylinders. *J. Chem. Phys. 106*, 2 (1997), 666.

[6] NELSON, D. R. *Defects and geometry in condensed matter*. Cambridge University Press, Cambridge, 2002.

[7] FRENKEL, D., AND SMIT, B. *Understanding Molecular Simulation*, second ed. Academic Press, London, 2002.

[8] ASTE, T., AND WEAIRE, D. *The pursuit of perfect packing*. Institute of Physics Publishing, Bristol, 2000.

[9] BOLHUIS, P. G., FRENKEL, D., MAU, S.-C., AND HUSE, D. A. Entropy difference between crystal phases. *Nature 388* (1997), 235.

[10] BRUCE, A. D., WILDING, N. B., AND ACKLAND, G. J. Free energy of crystalline solids: a lattice-switch Monte Carlo method. *Phys. Rev. Lett. 79*, 16 (1997), 3002.

[11] MAU, S.-C., AND HUSE, D. A. Stacking entropy of hard-sphere crystals. *Phys. Rev. E 59*, 4 (1999), 4396.

[12] FRENKEL, D. Introduction to colloidal systems. In *Soft and fragile matter. nonequilibrium dynamics, metastability and flow* (Bristol, 1999), M. E. Cates and M. R. Evans, Eds., Scottish Universities Summer school in Physics and Institute of Physics Publishing, pp. 113–143.

[13] PUSEY, P. N. Colloidal suspensions. In *Liquids, freezing and glass transition*, J.-P. Hansen, D. Levesque, and J. Zinn-Justin, Eds. Elsevier, Amsterdam, 1991, pp. 763–942.

[14] HOOGENBOOM, J. P. *Colloidal epitaxy, a real-space analysis*. PhD thesis, Universiteit Utrecht, September 2002. www.colloid.nl.

[15] VAN BLAADEREN, A., VELIKOV, K. P., HOOGENBOOM, J. P., VOSSEN, D. L. J., YETHIRAJ, A., DULLENS, R. P. A., VAN DILLEN, T., AND POLMAN, A. Manipulating colloidal crystallization for photonic applications: from self-organization to do-it-yourself organization. In *Photonic crystals and light organization in the 21st century*, C. M. Soukoulis, Ed. Kluwer Academic Publishers, Dordrecht, 2001, pp. 239–251.

[16] POON, W. C. K. A day in the life of a hard-sphere suspension. In *Soft and fragile matter. nonequilibrium dynamics, metastability and flow* (Bristol, 1999), M. E. Cates and M. R. Evans, Eds., Scottish Universities Summer school in Physics and Institute of Physics Publishing, pp. 1–8.

[17] PIAZZA, R., BELLINI, T., AND DEGIORGIO, V. Equilibrium sedimentation profiles of screened charged colloids: a test of the hard-sphere equation of state. *Phys. Rev. Lett. 71*, 25 (1993), 4267.

[18] RUTGERS, M. A., DUNSMUIR, J. H., XUE, J.-Z., RUSSEL, W. B., AND CHAIKIN, P. M. Measurement of the hard-sphere equation of state using screened charged polystyrene colloids. *Phys. Rev. B 53*, 9 (1996), 5043.

[19] PHAN, S.-E., RUSSEL, W. B., ZHU, J., AND CHAIKIN, P. M. Effects of polydispersity on hard sphere crystals. *J. Chem. Phys. 108*, 23 (1998), 9789.

[20] CHAIKIN, P. Thermodynamics and hydrodynamics of hard spheres: the role of gravity. In *Soft and fragile Matter. nonequilibrium dynamics, metastability and flow* (Bristol, 1999), M. E. Cates and M. R. Evans, Eds., Scottish Universities Summer school in Physics and Institute of Physics Publishing, pp. 315–348.

[21] PUSEY, P. N., AND VAN MEGEN, W. Phase behaviour in concentrated suspensions of nearly hard colloidal spheres. *Nature 320* (1986), 340.

[22] PHAN, S.-E., RUSSEL, W. B., CHENG, Z., ZHU, J., CHAIKIN, P. M., DUNSMUIR, J. A., AND OTTEWILL, R. A. Phase transition, equation of state, and limiting shear viscosities of hard sphere dispersions. *Phys. Rev. E 54*, 6 (1996), 6633.

[23] BOLHUIS, P. G., AND KOFKE, D. A. Monte Carlo study of freezing of polydisperse hard spheres. *Phys. Rev. E 54*, 1 (1996), 634.

[24] FASOLO, M., AND SOLLICH, P. Equilibrium phase behavior of polydisperse hard spheres. *Phys. Rev. Lett. 91*, 6 (2003), 068301.

[25] JACKSON, A. N., BRUCE, A. D., AND ACKLAND, G. J. Lattice-switch Monte Carlo method: application to soft potentials. *Phys. Rev. E 65* (2002), 036710.

[26] KEGEL, W. K., AND DHONT, J. K. G. "aging" of the structure of crystals of hard colloidal spheres. *J. Chem. Phys. 112*, 12 (2000), 3431.

[27] MARTELOZZO, V. C., SCHOFIELD, A. B., POON, W. C. K., AND PUSEY, P. N. Structural aging of crystals of hard-sphere colloids. *Phys. Rev. E 66* (2002), 021408.

[28] HOOGENBOOM, J. P., DERKS, D., VERGEER, P., AND VAN BLAADEREN, A. Stacking faults in colloidal crystals grown by sedimentation. *J. Chem. Phys. 117*, 24 (2002), 11320.

[29] PETUKHOV, A. V., DOLBNYA, I. P., DE HOOG, E. H. A., KASSAPIDOU, K., VROEGE, G. J., BRAS, W., AND LEKKERKERKER, H. N. W. High-resolution small-angle x-ray diffraction study of long-range order in hard-sphere colloidal crystals. *Phys. Rev. Lett. 88*, 20 (2002), 208301.

[30] ZHU, J., LI, M., ROGERS, R., MEYER, W., OTTEWILL, R. H., STS-73 SPACE SHUTTLE CREW, RUSSEL, W. B., AND CHAIKIN, P. M. Crystallization of hard-sphere colloids in microgravity. *Nature 387* (1997), 883.

[31] CHENG, Z., CHAIKIN, P. M., ZHU, J., RUSSEL, W. B., AND MEYER, W. V. Crystallization kinetics of hard spheres in microgravity in the coexistence regime: interactions between growin crystallites. *Phys. Rev. Lett. 88*, 1 (2002), 015501.

[32] VAN BLAADEREN, A., RUEL, R., AND WILTZIUS, P. Templated-directed colloidal crystallization. *Nature 385* (1997), 321.

[33] HOOGENBOOM, J. P., VAN LANGEN-SUURLING, A. K., ROMIJN, J., AND VAN BLAADEREN, A. Hard-sphere crystals with hcp and non-close-packed structure grown by colloidal epitaxy. *Phys. Rev. Lett. 90*, 13 (2003), 138301.

[34] KOFKE, D. A., AND BOLHUIS, P. G. Freezing of polydisperse hard spheres. *Phys. Rev. E 59*, 1 (1999), 618.

[35] BARTLETT, P. Fractionated crystallization in a polydisperse mixture of hard spheres. *J. Chem. Phys. 109*, 24 (1998), 10970.

[36] MURCH, G. A., AND NOWICK, A. S. *Diffusion in crystalline solids*. Academic Press, London, 1984.

[37] VAN GASTEL, R., SOMFAI, E., VAN SAARLOOS, W., AND FRENKEN, J. W. M. A giant atomic slide-puzzle. *Nature 408* (2000), 665.

[38] AGULLO-LOPEZ, F., CATLOW, C. R. A., AND TOWNSEND, P. D. *Point defects in materials*. Academic Press, London, 1988.

[39] BENNETT, C. H., AND ALDER, B. J. Studies in molecular dynamics. IX. vacancies in hard sphere crystals. *J. Chem. Phys. 54*, 11 (1971), 4796.

[40] PEIERLS, R. *Surprises in theoretical physics*. Princeton University Press, Princeton, 1979.

[41] CHAIKIN, P. M., AND LUBENSKY, T. C. *Principles of condensed matter physics*. Cambridge University Press, Cambridge, 1995.

[42] POLSON, J. M., TRIZAC, E., PRONK, S., AND FRENKEL, D. Finite-size corrections to the free energies of crystalline solids. *J. Chem. Phys. 112*, 12 (2000), 5339.

[43] SMITH, G. R., AND BRUCE, A. D. Multicanonical Monte Carlo study of solid-solid phase coexistence in a model colloid. *Phys. Rev. E 53*, 6 (1996), 6530.

[44] WALLACE, D. C. Thermoelastic theory of stressed crystals and higher-order elastic constants. In *Solid State Physics: Advances in Research and Applications*, H. Ehrenreich, F. Seitz, and D. Turnbull, Eds. Academic Press, New York, 1970, pp. 301–404.

[45] LANDAU, L. D., AND LIFSHITZ, E. M. *Theory of elasticity*. Pergamon Press, Oxford, 1970.

[46] WOJCIECHOWSKI, K. W., TRETIAKOV, K. V., BRAŃKA, A. C., AND KOWALIK, M. Elastic properties of two-dimensional hard disks in the close-packing limit. *J. Chem. Phys. 119*, 2 (2003), 939.

[47] ALLEN, M. P., AND TILDESLEY, D. J. *Computer Simulation of Liquids*. Oxford University Press, Oxford, 1987.

[48] RUNGE, K. J., AND CHESTER, G. V. Monte Carlo determination of the elastic constants for the hard-sphere solid. *Phys. Rev. A 36*, 10 (1987), 4852.

[49] SQUIRE, D. R., HOLT, A. C., AND HOOVER, W. G. Isothermal elastic constants for argon. theory and Monte Carlo calculations. *Physica 42* (1969), 388.

[50] PARRINELLO, M., AND RAHMAN, A. Crystal structure and pair potentials: a molecular-dynamics study. *Phys. Rev. Lett. 45*, 14 (1980), 1196.

[51] PARRINELLO, M., AND RAHMAN, A. Polymorphic transitions in single crystals: A new molecular dynamics method. *J. Appl. Phys. 52*, 12 (1981), 7182.

[52] SPRIK, M., IMPEY, R. W., AND KLEIN, M. L. Second-order elastic constants for the lennard-jones solid. *Phys. Rev. B 29* (1984), 4368.

[53] FARAGO, O., AND KANTOR, Y. Fluctuation formalism for elastic constants in hard-spheres-and-tethers systems. *Phys. Rev. E 61*, 3 (2000), 2478.

[54] SENGUPTA, S., NIELABA, P., RAO, M., AND BINDER, K. Elastic constants from microscopic strain fluctuations. *Phys. Rev. E 61,* 2 (2000), 1072.

[55] TRETIAKOV, K. V., AND WOJCIECHOWSKI, K. W. Orientational phase transition between hexagonal solids in planar systems of hard cyclic pentamers and heptamers. *J. Phys. Cond. Matt. 14* (2002), 1261.

[56] HANSEN, J.-P., AND MCDONALD, I. R. *Theory of simple liquids*. Academic Press, San Diego, 1986.

[57] RUSSEL, W. B. On the dynamics of the disorder-order transition. *Phase Transitions 21* (1990), 127.

[58] FRENKEL, D., AND LADD, A. J. C. New Monte Carlo method to compute the free energy of arbitrary solids. application to the fcc and hcp phases of hard spheres. *J. Chem. Phys. 81*, 7 (1984), 3188.

[59] WOODCOCK, L. V. Entropy difference between the face-centred cubic and hexagonal close-packed crystal structures. *Nature 385* (1997), 131.

[60] SCHÄTZEL, K., AND ANDERSON, B. J. Observation of density fluctuations. *Phys. Rev. Lett. 68*, 3 (1992), 337.

[61] HENDERSON, S. Crystallization mechanisms in colloidal systems. Master's thesis, Royal Melbourne Institute of Technology, 1993.

[62] PUSEY, P. N., VAN MEGEN, W., BARTLETT, P., ACKERSON, B. J., RARITY, J. G., AND UNDERWOOD, S. M. Structure of crystals of hard colloidal spheres. *Phys. Rev. Lett. 63*, 25 (1989), 2753.

[63] FRENKEL, J. *Kinetic theory of liquids*. Oxford University Press, Oxford, 1946.

[64] PETUKHOV, A. V., DOLBNYA, I. P., AARTS, D. G. A. L., VROEGE, G. J., AND LEKKERKERKER, H. N. W. Bragg rods and multiple x-ray scattering in random-stacking colloidal crystals. *Phys. Rev. Lett. 90*, 2 (2003), 028304.

[65] FRENKEL, D., AND LADD, A. J. C. Elastic constants of hard-sphere crystals. *Phys. Rev. Lett. 59*, 10 (1987), 1169.

[66] RAPAPORT, D. C. The event scheduling problem in molecular dynamics simulation. *J. Comp. Phys. 34* (1980), 184.

[67] SPEEDY, R. J. Pressure and entropy in hard-sphere crystals. *J. Phys. Cond. Matt. 10* (1998), 4387.

[68] STILLINGER, F. H., AND SALSBURG, Z. W. Elasticity in rigid-disk and rigid-sphere crystals. *J. Chem. Phys. 46*, 10 (1967), 3962.

[69] KOFKE, D. A., AND GLANDT, E. D. Monte Carlo simulation of multicomponent equlibria in a semigrand canonical ensemble. *Mol. Phys 64*, 6 (1988), 1105.

[70] BERG, B. A., AND NEUHAUS, T. Multicanonical ensemble: a new approach to simulate first-order phase transitions. *Phys. Rev. Lett. 68*, 1 (1991), 9.

[71] HALL, K. R. Another hard-sphere equation of state. *J. Chem. Phys. 57* (1970), 2252.

[72] REICHL, L. E. *A modern course in statistical physics*. Edwald Arnold (Publishers) Ltd., Oxford, 1980.

[73] PRONK, S., AND FRENKEL, D. Point defects in hard-sphere crystals. *J. Phys. Chem. B 105*, 28 (2001), 6722.

[74] YOUNG, A. P. Melting and the vector Coulomb gas in two dimensions. *Phys. Rev. B 19*, 4 (1979), 1855.

[75] STRANDBURG, K. J. Two-dimensional melting. *Rev. Mod. Phys. 60*, 1 (1988), 161.

[76] BAGCHI, K., ANDERSEN, H. C., AND SWOPE, W. Computer simulation of the melting transition in two dimensions. *Phys. Rev. Lett. 76*, 2 (1996), 255.

[77] CHEN, K., KAPLAN, T., AND MOSTOLLER, M. Melting in two-dimensional Lennard-Jones systems: Observation of a hexatic phase. *Phys. Rev. Lett. 74*, 20 (1995), 4019.

[78] BLADON, P., AND FRENKEL, D. Dislocation unbinding in dense two-dimensional crystals. *Phys. Rev. Lett. 74*, 13 (1995), 2519.

[79] ZAHN, K., LENKE, R., AND MARET, G. Two-stage melting of paramagnetic colloidal crystals in two dimensions. *Phys. Rev. Lett. 82*, 13 (1999), 2721.

[80] METROPOLIS, N., ROSENBLUTH, A. W., ROSENBLUTH, M. N., TELLER, A. H., AND TELLER, E. Equation of state calculations by fast computing machines. *J. Chem. Phys. 21*, 6 (1953), 1087.

[81] ALDER, B. J., AND WAINWRIGHT, T. E. Phase transition in elastic disks. *Phys. Rev. 127*, 2 (1961), 359.

[82] FERNÁNDEZ, J. F., ALONSO, J. J., AND STANKIEWICZ, J. One-stage continous melting transition in two dimensions. *Phys. Rev. Lett. 75*, 19 (1995), 3477.

[83] LEE, J., AND STRANDBURG, K. J. First-order melting transition of the hard-disk system. *Phys. Rev. B 46*, 17 (1992), 11190.

[84] WOJCIECHOWSKI, K. W., AND BRAŃKA, A. C. Elastic moduli of a perfect hard disc crystal in two dimensions. *Phys. Lett. A 134*, 5 (1988), 314.

[85] WEBER, H., AND MARX, D. Two-dimensional melting approached via finite-size scaling of bond-orientational order. *Europhys. Lett. 27* (1994), 593.

[86] WEBER, H., MARX, D., AND BINDER, K. Melting transition in two dimensions: A finite-size scaling analysis of bond-orientational order in hard disks. *Phys. Rev. B 51*, 20 (1995), 14636.

[87] ZOLLWEG, J. A., AND CHESTER, G. V. Melting in two dimensions. *Phys. Rev. B 46*, 17 (1992), 11186.

[88] JASTER, A. Computer simulations of the two-dimensional melting transition using hard disks. *Phys. Rev. E 59*, 3 (1999), 2594.

[89] BATES, M. A., AND FRENKEL, D. Influence of vacancies on the melting transition of hard disks in two dimensions. *Phys. Rev. E 61*, 5 (2000), 5233.

[90] SENGUPTA, S., NIELABA, P., AND BINDER, K. Elastic moduli, dislocation core energy, and melting of hard disks in two dimensions. *Phys. Rev. E 61*, 6 (2000), 6294.

[91] JASTER, A. Short-time behaviour of the two-dimensional hard-disk model. *Physica A 277* (2000), 106.

[92] JASTER, A. The hexatic phase of the two-dimensional hard disk system. *arXiv* (2003), cond–mat/0305239.

[93] SADR-LAHIJANY, M. R., RAY, P., AND STANLEY, H. E. Dispersity-driven melting transition in two-dimensional solids. *Phys. Rev. Lett. 79*, 17 (1997), 3206.

[94] SANTEN, L., AND KRAUTH, W. Absence of thermodynamic phase transition in a model glass former. *Nature 405* (2000), 550.

[95] SANTEN, L., AND KRAUTH, W. Liquid, glass and crystal in two dimensions. *arXiv* (2001), cond–mat/0107459.

[96] CALLEN, H. B. *Thermodynamics and an introduction to Thermostatistics*. John Wiley & Sons, New York, 1985.

[97] SAITO, Y. Monte Carlo studies of two-dimensional melting: dislocation vector systems. *Phys. Rev. B 26*, 11 (1982), 6239.

[98] CHUI, S. T. Grain-boundary theory of melting in two dimensions. *Phys. Rev. B 28*, 1 (1983), 178.

[99] DUPARCMEUR, Y. L., GERVOIS, A., AND TROADEC, J. P. Crystallization of pentagon packings. *J. Phys. Cond. Matt. 7* (1995), 3421.

[100] BRAŃKA, A. C., AND WOJCIECHOWSKI, K. W. Monte Carlo simulation of hard cyclic pentamers in two dimensions. equation of state and structural properties. *Mol. Phys 72* (1991), 941.

[101] BRAŃKA, A. C., AND WOJCIECHOWSKI, K. W. Monte Carlo simulation of hard cyclic pentamers in two dimensions. translational-rotational coupling in the orientationally disordered phase. *Mol. Phys 78* (1993), 1513.

[102] BRAŃKA, A. C., AND WOJCIECHOWSKI, K. W. Rotational phase transition and melting in a two-dimensional hard-cyclic-tetramer system. *Phys. Rev. Lett. 50* (1983), 846.

[103] WOJCIECHOWSKI, K. W., AND TRETIAKOV, K. V. Computer simulation of elastic properties of solids under pressure. *Comp. Phys. Comm. 121* (1999), 528.

[104] CUESTA, J. A., AND FRENKEL, D. Monte Carlo simulation of two-dimensional hard ellipses. *Phys. Rev. A 42*, 4 (1990), 2126.

[105] HENLY, C. L. Sphere packings and local environments in Penrose tilings. *Phys. Rev. B 34* (1986), 797.

[106] WANNIER, G. H. Antiferromagnetism. the triangular Ising net. *Phys. Rev. 79* (1950), 357.

[107] CHEN, Z.-Y., AND KARDAR, M. Elastic antiferromagnets on a triangular lattice. *J. Phys. C: Solid State Phys. 19* (1986), 6825.

[108] GU, L., CHAKRABORTY, B., GARRIDO, P. L., PHANI, M., AND LEBOWITZ, J. L. Monte Carlo study of a compressible Ising antiferromagnet on a triangular lattice. *Phys. Rev. B 53* (1996), 11985.

Summary

In this thesis, various properties of hard-body solids are explored. Chapters 3 through 6 deal with 3D crystals of hard spheres. Chapter 7 is about about the melting of the crystalline phase of polydisperse 2D hard disks. Finally chapter 8 discusses the phase behaviour of hard pentagons.

Chapter 2 presents a short review of free energy methods for simulations in crystalline solids, and of methods to calculate elastic constants. The free energy methods reviewed are thermodynamic integration and its variants (Einstein integration) and lattice switch Monte Carlo. For elasticity calculations, both direct calculations of the stress as a function of strain, and fluctuation methods to calculate the elastic constants are discussed.

In chapter 3 predictions are made about the stacking behaviour of growing hard-sphere crystals. Crystals of hard spheres can be found either in one of the two regulare close-packed arrangements: fcc (face-centered cubic) or hcp (hexagonal close-packed), or in a mixed form, random hexagonal close-packed, rhcp. All of these packings amount to different ways to stack the hexagonal planes that make up a hard-sphere crystal. As hard-sphere crystallites in a hard-sphere colloidal suspension, one can expect a small crystallite to be randomly stacked, because the bulk-free energy gain of the entropically favoured fcc and the interfacial free energy associated with an fcc-hcp transition are outweighed by the stacking entropy. As the crystal gets larger, the ratio of number of layers to the number of particles gets smaller and the fcc phase should win out. To show this, the bulk free energy of the two regular stackings is re-calculated (it is around $10^{-3}k_BT$ per particle) and the interfacial free energy between fcc and hcp is calculated. Based on these values, a prediction is made for the timescales at which a randomly stacked crystal will regrow into an purely fcc crystal.

Another aspect of hard sphere fcc-hcp stacking is discussed in chapter 4: the elastic behaviour of both stackings. Using stress-strain methods in simulation, it is shown that some of the elastic constants — most notably C_{12} — differ by up to 20% between fcc and hcp. This result is verified by free energy calculations, with the comparison to the stress-strain results involving some third-order elastic constants. In addition, the relative distance between the stacking planes of hcp (its c/a ratio) is found to be different to the equivalent in fcc, converging to that the fcc value as density increases. Finally, the influence of polydispersity on the elastic constants is investigated, and found to be minimal.

Chapters 5 and 6 an analysis of the point defect concentration in hard-sphere crystals is presented. Chapter 5 considers the monodisperse case and develops a

theoretical framework for equilibrium point defect (vacancy and interstitial) concentrations. Subsequently, interstitial concentrations are calculated (and are found to be in the order of 10^{-8}) and compared with a simple model.

The vacancy and interstitial concentrations for the polydisperse hard-sphere crystal are calculated in chapter 6. As polydispersity increases from zero towards the maximum polydispersity at which the crystal is stable, the vacancy concentration declines by roughly a factor of two (from around 10^{-4} to around 5×10^{-5}), while the interstitial concentration increases by a factor of 10^6, up to 2×10^{-2}. This is due to the finite concentration of particles that are small enough to easily become interstitials. It is found that the free energy associated with an interstitial is mainly sensitive to the radius of that interstitial, independently of the polydispersity of the crystal; this means that the small-particle tail of the particle-size distribution of the crystal will be crucial for the interstitial concentration in real hard-sphere colloidal crystals.

The melting transition of 2D hard disks is investigated in chapter 7, in the light of possible KTHNY (Kosterlitz-Thouless-Halperin-Nelson-Young) dislocation-mediated melting. The hard disk system is viewed as a limiting case of the polydisperse hard disk system, as the melting behaviour as a function of polydispersity is explored. This is done because in 3D the hard-sphere system displays a widening of the density-polydispersity gap upon increasing polydispersity, showing a stronger first-order character. In 2D, the apparent width of the phase transition (which may in fact be a continuous transition with finite size effects) appears unchanged as a function of polydispersity. In addition, the point at which the crystal becomes soft enough for dislocations to start unbinding (the point where the Young's modulus $K = 16\pi$) appears to be located inside the apparent phase transition gap consistently throughout the range of accessible polydispersities.

Finally, chapter 8 explores the phase behaviour of hard pentagons in 2D, as a system where the particle symmetry is incommensurate with any crystalline symmetry. The system is found to undergo two phase transitions: one liquid to rotator crystal phase transition similar to the 2D hard disk freezing transition, where the particles in the rotator crystal are positionally quasi-long-range ordered on a hexagonal lattice but rotationally unordered. The second (first-order) transition converts the rotator crystal to the fully ordered crystal, where the orientations of the pentagons are ordered in a striped fashion. The particle positions in the fully ordered crystal on a compressed hexagonal lattice, with lower symmetry than the hexagonal lattice. A comparison can be made between the second phase transition and the phase transition in the elastic antiferromagnet on a triangular lattice.

Samenvatting

Het mysterie van de entropie

De thermodynamica, of warmteleer, is één van de grote triomfen van de negentiende eeuwse fysica en is typisch negentiende eeuws van karakter: een klein aantal vaste basiswetten (de 'hoofdwetten van de thermodynamica') leidt via strikte logische deductie tot een wijd scala aan, in principe, exact meetbare voorspellingen. Met de thermodynamica kan niet alleen worden uitgerekend hoe efficiënt bijvoorbeeld een stoommachine kan zijn, maar ook worden voorspeld hoeveel warmer het water geworden is benedenaan een waterval. De oorsprong van de natuurkundige theorieën die in dit proefschrift zijn gebruikt, zijn bijna allemaal te herleiden tot de thermodynamica en haar ontwikkeling in de negentiende eeuw.

De thermodynamica is oorspronkelijk een stoommachine-theorie; de ontwikkeling ervan begon met de publicatie uit 1824 van Sadi Carnot (1796-1832): "*Réflexions sur la puissance motrice du feu et sur les machines propres à développer cette puissance*" ("Gedachten over het voortstuwende vermogen van vuur en over de machines die ertoe geëigend zijn om dit vermogen te ontwikkelen"). Carnot, die de zoon van een minister van oorlog onder Napoleon was, was geïrriteerd over de technologische achterstand van Frankrijk na de val van Napoleon, vooral wat de stoommachine betrof. Hij besloot om grondig uit te zoeken wat de maximale efficiëntie was van een stoommachine en welke concepten daarvoor belangrijk waren. Hoewel hij een theorie over warmte aanhing die later fout bleek te zijn (de warmtestoftheorie: de gedachte dat warmte een in hoeveelheid behouden vloeistof is) waren zijn concepten over stoommachine-cycli van groot belang voor de ontwikkeling van de thermodynamica door Clausius, Joule and Thomson, zo'n twintig jaar later.

De tweede hoofdwet

Van een aantal begrippen, zoals warmte, temperatuur, energie, had men voordat de thermodynamica werd ontwikkeld geen vastomlijnd idee. De thermodynamica gaat over deze begrippen, zij het dat er iets wordt aangenomen over het bestaan van moleculen. Er zijn twee belangrijke hoofdwetten. De eerste hoofdwet is de bekende wet van behoud van energie, die vastlegt dat de totale energie van het heelal altijd behouden blijft, in welke vorm dan ook.

De tweede hoofdwet lijkt concreet: er kan geen machine gebouwd worden die warmte uit de omgeving absorbeert en daaruit kracht genereert. Deze hoofdwet impliceert echter wel het bestaan van een ander begrip, dat lijkt op energie: de

entropie. De entropie is, in deze zin, een maat voor de energie die niet kan worden omgezet in arbeid (bruikbare kracht) en dus verloren gaat aan de omgeving: de tweede hoofdwet legt dus vast dat de entropie bij elke handeling gelijk blijft, of toeneemt.

De thermodynamica had warmte aan mechanische energie gekoppeld via temperatuur en entropie; iets wat erg handig is voor het maken van een stoommachine. Bovendien was de thermodynamica was een prachtige allesomvattende theorie, hoewel er één schoonheidsfout aan te merken was: niemand wist wat entropie eigenlijk was.

Is natuurkunde exact?

De kwestie van het wezen van de entropie werd opgelost door de ontdekkingen van de Oostenrijkse fysicus Ludwig Boltzmann (1844-1906) die in de jaren zeventig en tachting van de negentiende eeuw zijn statistische mechanica introduceerde. Hij benaderde natuurkunde op een totaal andere manier.

Boltzmann kwam met een theorie waarin hij voorspelde dat een grote hoeveelheid moleculen samen het beste met statistiek kunnen worden beschreven. Deze statistische beschrijving voorspelde dat er 'een grote kans' is dat de tweede hoofdwet van de thermodynamica gevolgd werd. Bijvoorbeeld, de kans dat één gram water iets ronduit tegen de tweede hoofdwet in doet *gedurende de leeftijd van het heelal* is te verwaarlozen.

Hij introduceerde deze theorie in een tijd waarin het bestaan van moleculen nog steeds betwist werd. Belangrijker nog is dat vóór Boltzmann's theorie de fysica benaderd vanuit het idee dat haar wetten absoluut geldig waren en dat de voorspellingen van deze wetten in principe perfect waren. Het statistische karakter van deze theorie stuitte op heftig verzet van de fysici uit die tijd, die niet gewend waren aan natuurwetten die niet absoluut geldig waren. Karakteristiek voor de twintigsteeeuwse fysica werd echter, dat het toeval niet uitgesloten werd. Toeval een centraal element geworden in veel moderne theorieën.

Bewegingsruimte en wanorde

In de statistische mechanica van Boltzmann staat het begrip entropie voor de totale 'bewegingsruimte' van de moleculen. Omdat er zo ontzettend veel moleculen zijn, zullen de moleculen overal zitten waar ze kunnen zitten. De maat voor waar ze kunnen zitten is de bewegingsruimte, die Boltzmann definieerde als de entropie.

Nu wordt het begrip entropie, de bewegingsruimte, vaak geassocieerd met wanorde. Dit is niet geheel onterecht; vaak houdt het volledig benutten van de bewegingsruimte namelijk in, dat het systeem ernaar streeft om de deeltjes langs elkaar heen te laten bewegen. In onze belevingswereld komt dit bijvoorbeeld overeen met het feit dat een woning altijd 'vanzelf' stoffiger wordt en nooit andersom: het wordt nooit spontaan schoner. Men moet arbeid verrichten om het schoon te maken.

Het smelten van ijs is een andere illustratie van wanorde door entropie: in ijs zitten de watermoleculen aan elkaar 'vast' doordat ze elkaar in specifieke richtingen sterk aantrekken. Als de temperatuur hoger dan 0° Celsius wordt, krijgen de deeltjes genoeg energie om los te komen uit deze aantrekkingskracht en gaat de entropie domineren: de deeltjes gaan langs elkaar heen bewegen (omdat ze dan de meeste bewegingsruimte hebben) en ijs wordt vloeibaar.

Omdat het niet mogelijk is uit de wanordelijke bewegingen van moleculen arbeid terug te winnen, komt dit idee van entropie overeen met dat van de tweede hoofdwet van de thermodynamica. Men hoeft nu alleen nog uit te rekenen hoeveel manouvreerruimte er tot elk molecuul ter beschikking staat om alles te weten te komen over de gedragingen van een materiaal. Helaas is dat niet zo eenvouding.

Virtuele experimenten

De statistische mechanica is zeer succesvol gebleken. Met behulp van deze theorie zijn in de loop van de twintigste eeuw praktisch alle evenwichtsfenomenen die te maken hebben met wisselwerkingen tussen grote aantallen deeltjes bestudeerd. Verklaringen voor het bestaan van allerlei fases (toestanden van stoffen) en faseovergangen (toestandswisselingen van stoffen zoals het smelten van ijs) zijn goed te begrijpen door het inzicht en het theoretische kader dat de statistische mechanica biedt.

Het is over het algemeen echter onmogelijk gebleken om 'exacte' oplossingen van de statistische mechanica te krijgen met puur theoretische overwegingen. De manier om deze exacte oplossingen te berekenen bestaat wel, maar is vaak wiskundig te moeilijk om uit te voeren. In plaats van naar deze exacte oplossingen te streven is het handiger gebleken om slimme aannames te maken en daarop gebaseerde vereenvoudigingen toe te passen om wiskundige problemen te omzeilen.

In de jaren vijftig kwam er een nieuw hulpmiddel ter beschikking van fysici. Computers werden gebruikt om virtuele experimenten uit te voeren die de werkelijkheid simuleren. Deze simulaties waren gebaseerd op de theorie van de statistische mechanica en rekenden gewoonweg uit wat voorheen onmogelijk was op te lossen met pen en papier. Ze maakten het voor het eerst mogelijk experimenten te doen op modellen in plaats van op echte gassen, vloeistoffen en vaste stoffen.

Een beperking van simulaties is dat ze, in vergelijking met de natuur, langzaam zijn. Daarom is het extreem tijdrovend om echte moleculen te simuleren en vaak moeten we het doen met vereenvoudigde versies. Van deze model-moleculen kan men dan nagaan of ze een gas- en een vloeistoffase hebben, wanneer ze een kristal vormen, enzovoort. Het nadeel van de eenvoud van de model-moleculen kan dan ook een voordeel worden: als je het eenvoudigste model-molecuul dat een bepaalde eigenschap geeft aan het systeem als geheel (het kristalliseert bijvoorbeeld), kan je er achter komen wat voor die eigenschap belangrijk is en waardoor het veroorzaakt wordt.

Harde bollen

Het systeem van harde bollen is één van de meest eenvoudige modelsystemen. Moleculen worden hier voorgesteld als harde bollen die elastisch met elkaar botsen in een ‘vat’. Omdat de bollen elkaar alleen voelen als ze botsen, hangt de bewegingsruimte niet af van de temperatuur (de bewegingssnelheid van de bollen), maar alleen van het totale volume van het ‘vat’ waar de bollen in zitten, en het aantal bollen. Omdat de fase (toestand, zoals vloeibaar of vast) alleen afhangt van waar de moleculen zich ten opzichte van elkaar bevinden, worden de fases van een harde-bollen systeem alleen bepaald door de dichtheid (het volume van het vat per deeltje).

Toen in de jaren vijftig in Californië de eerste computersimulaties van harde-bollen systemen werden gedaan door Bernie Alder en Tom Wainwright, zag men tot ieders verbazing dat een systeem van harde bollen bij hogere dichtheden spontaan een geordend kristal; het bevriest. Blijkbaar is de bewegingsruimte van de deeltjes bij hogere dichtheden groter als ze netjes geordend in een kristal zitten dan wanneer ze (elkaar hinderend) langs elkaar heen kunnen bewegen.

Men was zeer verbaasd over het feit dat kristallen niet per sé vanwege de onderliggende aantrekkingskrachten van de moleculen ontstaan (wat overigens in natuurkundeboeken voor de middelbare school nog steeds beweerd wordt) maar vanwege de extra bewegingsruimte die verkregen wordt door ordening. Zo verbaasd zelfs, dat op de conferentie waar de resultaten werden gepresenteerd het door de nieuwe methode van computersimulaties bereikte resultaat door een groot gedeelte van deelnemers simpelweg niet geloofd werd. Uiteindelijk werd de kwestie zelfs in stemming gebracht — wat in de natuurwetenschappen hoogst ongebruikelijk is. Tegenwoordig is het idee dat stoffen bevriezen vanwege de onderlinge afstoting die de moleculen erin voelen als ze dicht bij elkaar komen (ze hebben een ‘vorm’), net zoals harde bollen, echter algemeen geaccepteerd.

Vijfhoeken

Wat er gebeurt bij het samendrukken van een systeem waarin deeltjes niet passen bij de vorm van het kristal, is in een deel van dit proefschrift onderzocht. Het systeem, dat onderzocht is door middel van simulaties, is dat van harde vijfhoeken (pentagons) op een vlak. Op een vlak willen deeltjes zich namelijk over het algemeen in een driehoekig rooster ordenen, dat niet past bij de vijfhoekigheid van vijfhoeken.

Bij lage dichtheden bewegen de vijfhoeken vrijelijk langs elkaar heen, zoals te zien is aan de linkerzijde van afbeelding 8.6 op pagina 82. Ze wijzen alle kanten op; de ‘richting’ van de vijfhoek is weergegeven als een tint: hoe donkerder, hoe groter de hoek van het linkerpunt met een horizontale lijn. In het middelste plaatje staat een uitkomst van een simulatie bij een meer samengedrukt systeem waarbij de vijfhoeken zich ordenen op een driehoekig rooster, maar ze alle kanten blijven opwijzen. Pas bij de hoogste dichtheden gaan ze zich ook in de ‘wijsrichting’ ordenen en ontstaat de volledig geordende struktuur van het laatste plaatje. Het

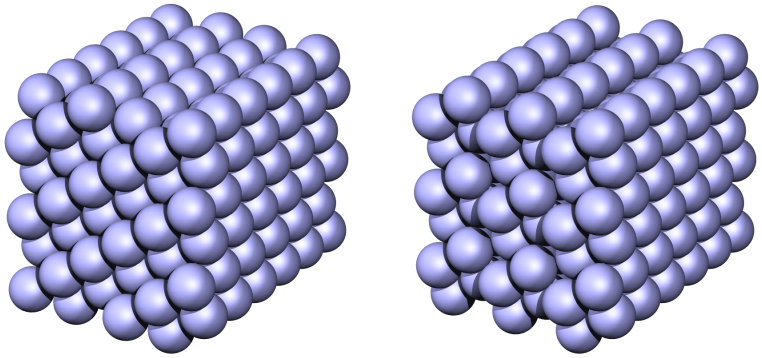

Figuur 8.8: De fcc (links) en hcp (rechts) stapelingen van harde bollen

resultaat van de simulaties is, dat het rooster niet meer gelijkzijdige driehoekig is, zoals bij het middelste plaatje, maar een beetje wordt samengedrukt door de ordening van de ‘wijsrichting’ van de vijfhoeken.

Stapelingen

Bij de harde-bollen-kristallen is er iets speciaals; er zijn meerdere varianten mogelijk. Dit heeft te maken met de beste manier waarop bollen gestapeld kunnen worden. In 1611 merkte Johannes Keppler (de ontdekker van de wetten van de planeetbanen) al een overeenkomst op tussen stapels van kanonskogels en de symmetrieën van sommige kristallen. De beste manier om harde bollen te stapelen is namelijk om ze in lagen neer te leggen die driehoekjes vormen (zie bijvoorbeeld afbeelding 1.1 op pagina 2). Deze lagen worden dan op elkaar gestapeld op zo’n manier dat de volgende laag in de ’gaten’ van de laag eronder komen te zitten. Overigens is dit pas in 1999 wiskundig bewezen.

Bizar is het, dat een verzameling kris-kras langs elkaar heen bewegende harde bollen uiteindelijk spontaan een geordende pakking gaat aannemen. De harde bollen moeten hier dan wel een keuze maken: er zijn in het in het stapelen van de lagen twee keuzes. Dat maakt bij twee lagen niet uit, maar bij de derde laag kan men dan kiezen voor één van de twee stapelingen; de derde laag komt óf precies boven de eerste laag te liggen (dit heet *hexagonal close packing* of hcp; zie weer de afbeelding op pagina 2), óf de derde laag komt in de gaten van de tweede laag te zitten die niet precies boven de eerste laag zitten (dit heet *face centered cubic* of fcc), zodat er een regelmatige pakking ontstaat uit bouwstenen van telkens twee (hcp) of drie (fcc) lagen. Zie figuur 8.8 voor plaatjes van de zo gevormde kristallen.

Hoewel deze twee kristalvormen erg op elkaar lijken (de deeltjes hebben in beide soorten pakking bijvoorbeeld hetzelfde aantal ‘buren’), is een paar jaar geleden gebleken dat het kristal iets meer bewegingsruimte heeft in de fcc pakking: ongeveer een tiende van een procent meer dan in hcp. Voor dit proefschrift is berekend dat, als de kristallen klein zijn, de bewegingsruimte van het *kiezen* van de

lagen belangrijk wordt, en de kristallen een wanordelijke stapeling gaan vormen: sommige lagen worden fcc en sommige hcp.

Bij grotere kristallen verandert de stapeling langzaam in fcc, omdat dan de winst van het kiezen van de lagen verdwijnt ten opzichte van de winst van het meer stabiele fcc: je kan immers maar één keer per laag een stapeling kiezen. Het bewegingsruimte-voordeel van de stabielere fcc pakking groeit ondertussen met het aantal deeltjes in het hele kristal.

Een andere, verrassende uitkomst van simulaties voor dit proefschrift is dat het verschil in elastische eigenschappen van de twee kristallen erg groot is. De elastische eigenschappen van een kristal zijn de 'vervormbaardheden' in bepaalde richtingen als het kristal op bepaalde manieren wordt vervormd. Het blijkt dat voor sommige vervormingen 'samendrukbaarheid' met meer dan 20% verschillen tussen fcc en hcp.

Nu zijn er echte stoffen die bestaan uit bouwstenen die lijken op harde bollen: colloïden. Stoffen als melk, verf en bloed bestaan uit oplossingen van dit soort deeltjes. Omdat ze zo klein zijn, bewegen ze langs elkaar op de manier waarop Boltzmann dat beschreven heeft in de statistische mechanica, net als de veel kleinere moleculen. Deze colloïdale deeltjes kunnen, net als de model-harde bollen, kristalliseren; een natuurlijk voorbeeld daarvan zijn opalen. Omdat de deeltjes ongeveer net zo groot zijn als de golflengte van zichtbaar licht, zijn er mogelijk toepassingen voor dit soort kristallen in het bouwen van materialen met speciale optische eigenschappen; de precieze stapeling van deze kristallen moet dan wel bekend zijn.

Roosterfouten

Voor dit proefschrift zijn simulaties gedaan om uit te rekenen hoeveel roosterfouten er te verwachten zijn. Dit is van belang voor praktische toepassingen: fouten, zoals het afwezig zijn van een deeltje (een zogeheten vacature), of het aanwezig zijn van een extra deeltje tussen de roosterplaatsen van het kristal (een interstitiëel). Roosterfouten ontstaan spontaan, omdat de winst in bewegingsruimte voor een roosterfout (deze kan dan door het hele vat gaan) groter kan zijn dan het verlies in bewegingsruimte voor de kristaldeeltjes om de fout heen door de vervorming van het kristal.

Als elke harde bol even groot is, zijn deze aantallen klein (één op de 4000 roosterplekken heeft geen deeltje, en één op de 100 miljoen deeltjes is dan een interstitiëel). In een colloïdale suspensie zijn echter niet alle deeltjes even groot. Het blijkt, dat als daarmee rekening wordt gehouden het aantal interstitiëlen dramatisch toeneemt als het verschil tussen het grootste en het kleinste deeltje groter wordt: met een factor van 1 miljoen; één op de vijftig deeltjes. Dit gebeurt omdat er een aantal deeltjes is dat klein genoeg is om makkelijker tussen de roosterplekken in te gaan zitten. Wil men dus goede colloïdale kristallen maken voor optische toepassingen, zal moet de spreiding van de deeltjesgroottes goed onder controle moeten houden.

De interstitiëlen bewegen verrassend snel door het kristal. Wanneer een interstitiëel de plaats inneemt van een deeltje in het kristal, schuift de feitelijke inter-

stitiëel een stuk op. In figuur 5.3 op pagina 50 is de (op een vlak geprojecteerde) positie van de interstitiëel in een kristal gevolgd over langere tijd. Het onderliggende rooster is duidelijk te zien, samen met de sprongen. Vaak wordt er honderden keren heen en weer gesprongen. Het uiteindelijke effect is een soort ‘moleculaire stoelendans’.

Dit proefschrift illustreert dat er veel onverwachte rijkdom te vinden is in het gedrag van verzamelingen eenvoudige deeltjes. Het collectieve gedrag van simpele deeltjes als harde bollen biedt niet alleen verklaringen voor het gedrag van de ingewikkeldere echte moleculen, maar heeft zijn eigen, unieke eigenschappen waaraan de drang naar bewegingsruimte ten grondslag ligt.

Nawoord

Vanaf deze plek wil ik een aantal mensen bedanken voor hun hulp bij het tot stand komen van dit proefschrift. Op de eerste plaats wil ik mijn woorden richten tot mijn promotor, Daan Frenkel. Daan, het was een voorrecht om bij jou promovendus te zijn. Het waren niet alleen jouw snelle inzicht, goede ideeën en suggesties, maar ook je benadering van wetenschap, waar ik heel veel van geleerd heb. Jouw gave om de juiste vragen te stellen, die in staat stellen met de juiste middelen te worden beantwoord, blijft verbazen.

Bela, ook van jouw enthousiaste manier van omgaan met natuurkunde in combinatie met je zeer brede kennis, heb ik ontzettend veel geleerd. Ik wil je, samen met Tanja Schilling bedanken voor de samenwerking die heeft geleid tot hoofdstuk 8.

De discussies met Jacob Hoogenboom over zijn indrukwekende experimentele resultaten met het groeien van hcp harde-bollen kristallen in de groep van Alfons van Blaaderen, hebben geleid tot de inspiratie voor hoofdstuk 4.

Even after returning from the ‘Villa’, the group has retained its cohesion and its great atmosphere. The group has, over the years, consistently been a collection of very nice people with great scientific curiosity. The eagerness to devote time to answer questions and discuss ideas has been wonderful to experience. The great atmosphere in the group has manifested itself in the numerous occasions at which we saw each other outside the lab, for example playing a game of ‘Kolonisten’ or seeing a movie; these were great times.

Tijdens mijn tijd als student hier op Amolf had ik het plezier om met Paul Wessels en Joël Wijngaarde op één kamer te zitten. Nu ben ik blij dat julie mijn paranimfen willen zijn. Paul, wij zijn inderdaad samen ‘wetenschappelijk volwassen’ geworden; in niet-wetenschappelijk opgroeien heb jij sinds juli dit jaar al de volgende stap genomen. Joël, nadat je afstudeerde en Us Media begon, hield je me op gezette momenten in de ‘echte wereld’.

Ron en Joris, julie vermogen om alles te relativeren vond een dankbaar onderwerp in mijn onderzoek. Julie verhalen over experimenten met echte muizen maakte mijn tijd als promovendus in de computerfysica een stuk draaglijker.

Ik wil mijn ouders en mijn broer Dénes bedanken voor hun steun, belangstelling en motivatie. Als laatste natuurlijk Pieternel; jouw bijdrage tot dit proefschrift is veel groter dan je waarschijnlijk denkt en jouw bijdrage tot wie ik ben en wie wij zijn is nog onnoemelijk veel groter.